

A Wearable Blood Pressure Sensor Using Oscillometric Photoplethysmography and Micro Accelerometers

by

Phillip Andrew Shaltis

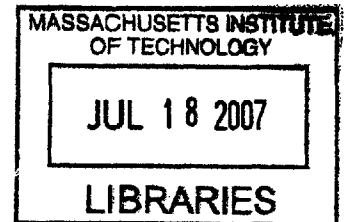
B.A. Physics
Albion College, 1999

B.S. Mechanical Engineering
University of Michigan, 2000

S.M. Mechanical Engineering
Massachusetts Institute of Technology, 2004

S.M. Electrical Engineering and Computer Science
Massachusetts Institute of Technology, 2004

ARCHIVES



SUBMITTED TO THE DEPARTMENT OF MECHANICAL ENGINEERING IN PARTIAL
FULFILLMENT OF THE REQUIREMENTS FOR THE DEGREE OF

DOCTOR OF PHILOSOPHY IN MECHANICAL ENGINEERING

AT THE

MASSACHUSETTS INSTITUTE OF TECHNOLOGY

June 2007

© 2007 Massachusetts Institute of Technology. All rights reserved.

Signature of Author:

Department of Mechanical Engineering
May 21, 2007

Certified by:

H. Harry Asada
Ford Professor of Mechanical Engineering
Thesis Supervisor

Accepted by:

Lallit Anand
Professor of Mechanical Engineering
Chairman, Committee for Graduate Students

A Wearable Blood Pressure Sensor Using Oscillometric Photoplethysmography and Micro Accelerometers

by

Phillip Andrew Shaltis

Submitted to the Department of Mechanical Engineering on May 21, 2007 in Partial Fulfillment of the Requirements for the Degree of Doctor of Philosophy in Mechanical Engineering

ABSTRACT

Monitoring arterial blood pressure (ABP) with a sensor virtually imperceptible to the wearer, for continuous periods of weeks, months, or years, could prove revolutionary in the diagnosis and treatment of chronic hypertension and heart failure, as well as a monitoring tool for convalescing individuals, and individuals in hazardous duty (such as firefighters or soldiers). To this end, a miniaturizable, non-invasive blood pressure sensor is designed and validated. A solid, coin-sized cuff-less photoplethysmography (PPG) sensor worn over a palpable artery is utilized to measure arterial blood pressure. Measurements are obtained through a modified oscillometric technique which eliminates the need for a high pressure cuff and instead, takes advantage of natural hydrostatic pressure changes caused by raising and lowering the subject's arm. In this work, the principle of hydrostatic oscillometry is first detailed. To better understand the internal mechanisms of pressure propagation within the tissue, a comprehensive non-linear finite element model of the finger base is constructed and validated using a combination of magnetic resonance imaging and experimental tissue stiffness measurements. A prototype finger blood pressure monitor is designed and constructed in combination with a novel accelerometer-based height sensor. The 95% confidence interval for a Bland-Altman comparison between the proposed sensor's mean arterial pressure (MAP) measurements and the simultaneous Finapres MAP measurements is [+919, -283] Pa ([+6.91, -9.04] mmHg). The percent difference between the two methods is shown to be 3.0%. A method for continuous MAP measurements utilizing the sensor system is proposed and is shown to be capable of providing reliable measurements for several minutes.

Thesis Committee:

H. Harry Asada, Chair

Ford Professor of Mechanical Engineering

Ian Hunter

Hatsopoulos Professor of Mechanical Engineering

Roger Kamm

Germeshausen Professor of Mechanical and Biological Engineering

Andrew Reisner

Visiting Scientist in Harvard-MIT Division of Health Sciences & Technology

Acknowledgements

This thesis would not have been possible without the guidance, support, and friendship of the following people.

Melissa, you are my best friend, my smile, my harshest critic (other than myself), and my love each and every day. You make my life in so many ways. Thank you for your patience, love, and compassion. You mean everything to me.

To my family - I can't begin to express what all of you mean to me. Your unconditional love and support give me strength and keep me sane. Mom – thank you for always listening to me and for always being there, no matter what. Dad – thank you for being such an amazing role model, teacher, and friend. I hope that someday I can be as successful as you. Bill – thanks for putting up with me when we were growing up. You are an incredible guy with amazing talents and someone who I am and will always be proud to call my brother.

I would like to thank my thesis advisor, Professor Harry Asada, for his tireless commitment to my growth as both a scholar and a researcher. I am grateful for his willingness to continually push the bounds of my abilities and for never letting me be satisfied with “good enough.” His faith in my abilities has been a source of strength throughout the project.

I would also like to thank Dr. Andrew Reisner for his friendship and support throughout this project. His insights and unique medical perspective have not only enhanced my understanding and appreciation of the underlying physiology of the plethysmograph signal, but have helped me to better understand how essential it is for an engineer to be able to visualize their work from both a clinician's and a patient's perspective.

I wish to thank my thesis committee Prof. Harry Asada, Prof. Ian Hunter, Prof. Roger Kamm, and Dr. Andrew Reisner for their time and valuable suggestions throughout the course of this thesis. I would also like to thank Raymond Mandeville for his time and help with the refinement of the finite element model, Chris Gaynor for her help in acquiring an MR image of the finger, and Bryant Harrison for his help with collecting human subject data.

To the *Asada Group* – you guys are the best. The people may change, but the spirit of the lab always remains. From lunches to volleyball to support during the qualifying exams, you guys, even the “new fish,” help to make the days bearable even when there are umpteen sponsor visits scheduled the day before a big homework assignment is due. Thanks for being there and for always making sure that life in the lab is entertaining. A special thanks to all of those who have added to this project in various ways, Devin McCombie, Aleksandar Marinkovic, Levi Wood, Jin-Oh Hahn, Eric Wade, Kyu Jin Cho, Binayak Roy, Manas Menon, Lael Odhner Dr. Jun Ueda, Tom Secord, Chris Brown, and Josiah Rosmarin. Thank you.

Table of Contents

Chapter 1	Introduction	11
1.1	Background and Objectives.....	11
1.2	Outline of Thesis.....	12
Chapter 2	Utility of the Photoplethysmogram.....	15
2.1	Physical Basis of the PPG Signal	15
2.1.1	Optics Considerations.....	15
2.1.2	Physiological Considerations	18
2.2	Relating Plethysmography/PPG to ABP	19
2.3	Monitoring Applications	22
2.3.1	Arterial Blood Pressure from PPG.....	22
2.3.2	PPG as a Binary Indicator of Pulsatile Perfusion	24
2.3.3	The Volume Clamp	25
Chapter 3	Oscillometric ABP Measurement with PPG.....	26
3.1	Oscillometric ABP Measurement with PPG.....	26
3.2	Hydrostatic Pressure Challenge.....	28
Chapter 4	Theoretical Analysis of Sensor-Artery Interaction.....	32
4.1	Formulating the Finite Element Model	33
4.1.1	Model Formulation: Anatomical Component Selection.....	35
4.1.2	Model Formulation: Geometry Selection	36
4.1.3	Model Formulation: Material Selection	40
4.1.4	Model Formulation: Boundary Selection and Loading.....	43
4.1.5	Model Formulation: Meshing Method	44
4.2	Validating the Finite Element Model	45
4.2.1	MRI Studies	45
4.2.2	Experimental Tissue Stiffness Measurements	48
4.3	Finite Element Driven Ring Sensor Design Analysis	51
4.3.1	Blood Flow Interference Prevention	51
4.3.2	Sensor Misalignment	52
4.3.3	Ring Sensor Contact Geometries	53
4.3.4	Influence of the Tendon on Pressure Propagation	54
4.3.5	Focally-applied Pressure Oscillometry	55
4.3.6	Limitations of the Model: Circumferential Oscillometric Cuff Simulation	59
4.4	Finite Element Modeling Results Summary.....	61
Chapter 5	Sensor Design and Implementation	62
5.1	Mechanical Design	63
5.1.1	Optical Components	63
5.1.2	Applied Pressure Measurement Components	64
5.2	Motorized Sensor Units	66

5.2.1	DC Motor Driven.....	66
5.2.2	Piezo-based Linear Actuator.....	69
5.3	Height Sensor.....	71
5.3.1	Theory and Implementation	71
5.3.2	Height Sensor Considerations	73
5.4	Electronic Component Design	74
5.4.1	Photodetector Array.....	74
5.4.2	LED Control.....	76
5.4.3	Pressure Sensor Conditioning.....	77
5.4.4	Accelerometer Conditioning.....	78
5.4.5	Motor Driver	79
5.5	Sensor Registration and Signal Processing	80
5.6	Data Acquisition and User Interface.....	87
5.7	Design Concept Considerations.....	89
5.8	PPG for MAP Measurement Consideration	91
Chapter 6 ABP Measurement Protocol.....		93
6.1	Hydrostatic Protocol.....	93
6.2	Hydrostatic Protocol Considerations	95
Chapter 7 Human Subject Testing		98
7.1	Blood Pressure Measurements	98
7.1.1	Compliance Curve Identification	98
7.1.2	Systolic and Diastolic Pressure Estimation.....	99
7.1.3	Bland-Altman	101
Chapter 8 Continuous ABP Estimation.....		103
Chapter 9 Conclusions.....		109
9.1	Summary of Contributions	109
Appendix A. Approved Study Protocol		111
Appendix B. Ring Sensor Drawings		117
References.....		119

List of Figures & Tables

Figure 1: Illustrative representation of the relative photon absorbance for various sections of the finger.	16
Figure 2: Hierarchy of the factors leading to a PPG signal.	17
Figure 3: Plot of the pressure-volume (PPG-based) loops occurring over a range of applied transmural pressures.....	21
Figure 4: Illustration of the sigmoidal volume-transmural pressure relationship which governs the appearance of a PPG signal. When low external pressures are applied (large positive transmural pressure) the peaks of the waveform are distorted or saturated in appearance. As the cuff pressure is increased (transmural pressure approaches zero), the PPG waveform more closely approximates the underlying blood pressure waveform. For cuff pressures significantly larger than the internal blood pressure (large negative transmural pressure) there is almost no visible waveform as the vascular wall has been collapsed.	23
Figure 5: Sigmoidal compliance curve relating blood vessel volume change to transmural pressure [10].....	27
Figure 6: Finger cross-section with a PPG sensor. (a.) Illustration of basic PPG sensor principle; (b.) Illustration of how an increase in cuff pressure can affect the light paths of a PPG sensor. Changing the cuff pressure can change both the path length and the tissue sections illuminated by the sensor.	27
Figure 7: PPG amplitude against transmural pressure.	28
Figure 8: Hydrostatic pressure due to the arm height. Positive h points upwards. When lowered below the heart, $h < 0$ and the bottom hydrostatic pressure is $-\rho gh > 0$	29
Figure 9: Photograph of the sensor unit worn at the finger base by a research subject.....	33
Figure 10: Finger cross-section imported into ADINA.	34
Figure 11: Illustration of the contacting surface utilized in our finite element model.	34
Figure 12: Illustration of a cross section of human skin [].	35
Figure 13: Sagittal cross section of a human finger [].	36
Figure 14: Sketch illustrating the location of the cutting plane used to create the finger slice to the right.	37
Figure 15: Cross-sectional slice of the right hand at the finger base of a cadaver [].	37
Figure 16: Complete finite element models of the finger base. a.) The tendon is modeled as a nearly rigid material surrounding the bone; b.) The tendon extends far below the bone and is rigid in structure.	38
Figure 17: Illustration of how the tendon is tightly coupled to the bone through wrapping [].	39
Figure 18: Illustration of the various components comprising a typical arterial wall.	40
Figure 19: Plot of an Ogden model fit to arterial wall stress-strain data provided by Sato, et. al. The above compliance curve defines the non-linear compliance characteristics of the modeled arterial wall.....	41
Figure 20: MRI image of a deformed fingerpad while loaded with a 1mm prescribed surface displacement [67].....	46
Figure 21: T1-weighted MRI of normal finger base [].	46
Figure 22: T1-weighted MRI of finger base deformed by passively loaded ring sensor.	46
Figure 23: Labeled MRI of a deformed finger base with the ring sensor for reference.	47

Figure 24: Picture of the finger base stiffness measurement system.	48
Figure 25: Human finger base compliance testing results compared to FE simulations.	49
Figure 26: Comparison of the experimentally measured and FEA results for surface pressures resulting from a prescribed local displacement.	50
Figure 27: Nominal pressure distribution within the finger resulting from the focally applied pressure.	51
Figure 28: Pressure distribution within the finger resulting from a severe rotation of the finger relative to the position of the blood pressure sensor.	52
Figure 29: Simple L-shaped contact surface.	53
Figure 30: Representation of the existing ring sensor contact surface with larger local protrusion.	53
Figure 31: Pressure distribution within the finger base resulting from a 1 mm prescribed displacement of the ring sensor unit.	54
Figure 32: Close-up view of the of the pressure acting around the circumference of the arterial wall. Note the large range of applied pressures.	54
Figure 33: Illustration of piece-wise linear method used with experimentally measured tissue stiffness results.	56
Figure 34: FE model implemented for directly simulating oscillometry.	57
Figure 35: Comparison of artery pulsation amplitude vs. transmural pressure for locally applied loading conditions.	58
Figure 36: Comparison of the oscillometric results for a 20% change in the elastic modulus of the surrounding tissue.	59
Figure 37: FE simulation of a circumferentially applied pressure illustrating the relatively uniform pressure distribution within the finger.	60
Figure 38: Prototype PPG ring sensor for MAP monitoring.	62
Figure 39: Illustration of the finger base with sensor unit.	64
Figure 40: CAD drawing and illustration of the cantilever mechanism used to apply localized pressure.	65
Figure 41: Motorized ring sensor design with movable pressure stage.	67
Figure 42: Close-up view of the actuated pressure stage with the pressure sensor.	67
Figure 43: Isometric view of the lifting mechanism contained within the motorized ring sensor.	68
Figure 44: Side view of the motorize ring sensor illustrating the travel available to the threaded nut and pressure stage as the motor is activated.	68
Figure 45: (a.) Squiggle series linear actuator; (b.) Ring Sensor using miniature piezo actuator.	70
Figure 46: Initial BP prototype with dimensions. The additional analog and digital conditioning circuitry are not pictured.	70
Figure 47: Actuated BP prototype with all required conditioning conditioning circuitry.	70
Figure 48: Illustration of the proposed height sensor using two MEMS accelerometers.	72
Figure 49: Definition of height measurement terms.	72
Figure 50: Schematic of multi-plexed PD array circuit.	75
Figure 51: CAD illustration of assembled PD array circuit.	76
Figure 52: Schematic and accompanying CAD illustration of the LED control circuitry.	77
Figure 53: Schematic and CAD illustration of the circuit used to condition the output signal of the pressure sensor.	78

Figure 54: 3-axis accelerometer schematic and CAD illustration.	79
Figure 55: Low power DC motor driver schematic and CAD model.....	80
Figure 56: Simultaneous waveform outputs from multiple photodetector array elements.....	81
Figure 57: Plot of the mean PPG amplitudes vs. photodetector element which illustrates a properly registered sensor. The maximum amplitude signal is found to occur near the middle of the photodetector array.	82
Figure 58: High-pass filtered PPG waveforms with detected maximum and minimum values (*).	84
Figure 59: Example of the raw data with Gaussian curve fit.....	86
Figure 60: Windows-based GUI for the blood pressure sensor calibration and registration.....	88
Figure 61: Data acquisition and sensor monitoring GUI.	89
Figure 62: Plots of the (a) Fingerbase PPG output; (b) Fingertip PPG output; (c) Digital blood pressure; (d) Measured arm height during a typical 20 second/height experiment.	93
Figure 63: Plots for two subjects (Subject A shown in the top row, subject B in the bottom) comparing the repeatability of the hydrostatic challenge for various height change rates. Rapid calibrations appear to be less reliable than more gradual hydrostatic calibration routines.....	95
Figure 64: Plots comparing the measured responses of the finger base PPG, fingertip PPG, and blood pressure sensor (from top to bottom) during a large hydrostatic pressure change.	96
Figure 65: Comparison of the compliance curves with Gaussian fit models generated by the hydrostatic challenge. The conditioned PPG amplitudes are represented by discrete data points (o); Gaussian fits applied to the raw data are shown with continuous lines.	99
Figure 66: Hydrostatic challenge derived compliance curve with Gaussian fit model. PPG amplitudes are represented by discrete data points (o); Measured values for the mean, systolic/diastolic blood pressures are illustrated in the figure. Specifically, for the hydrostatic method (in mmHg): MAP = 97, Systolic/Diastolic = 113/90; for the Finapres (in mmHg): MAP = 97, Systolic/Diastolic = 121/85.....	100
Figure 67: Comparison of the Finapres and Ring Sensor diastolic, mean and systolic blood pressure measurements for nine subjects.	101
Figure 68: Illustration of a method for continuous blood pressure measurements.....	104
Figure 69: Comparison of the hydrostatic calibration curves generated over a 35 minute period of time.	106
Figure 70: Comparison of continuous MAP measurements provided by a Finapres device and the Ring Sensor.	107
Figure 71: Comparison of two fingers immediately after long-term monitoring experiment. The Finapres finger is a deep shade of purple while the ring sensor finger is a healthy flesh tone.	108

Index of Terms

General Terms

P_{tm}	Transmural pressure across arterial wall
P_{in}	Mean locally measured internal arterial blood pressure
P_{out}	Mean compressive pressure acting on the outside of the arterial wall
ΔP	Pulsatile arterial blood pressure component
ΔV	Pulsatile arterial volume change
P_{ABP}	Mean arterial blood pressure
P_{HYD}	Hydrostatic pressure offset in local arterial blood pressure relative to heart pressure
ρ	Density of whole blood
g	Acceleration of gravity
h	Height of sensor relative to the heart
θ_j	Angle of accelerometer axis relative to gravity vector
l_k	Length of arm link
P_{cuff}	Circumferentially applied external pressure
i, j, k, n	Indices

Finite Element Modeling Terms

W	Ogden model fitting curve
μ_n	Ogden model material constant
α_n	Ogden model material constant
λ_i	Principle components of the stretch tensor
ϕ	Diameter
E	Young's modulus
ν	Poisson's ratio

Sensor Calibration Terms

\bar{y}_{AC_PPG}	Conditioned amplitude of the PPG signal
h_{zero_Ptm}	Arm height corresponding to the maximum PPG amplitude
P_{MAP}	Mean arterial pressure estimated from the hydrostatic challenge
P_{ext}	Locally applied external ring pressure
P_r	Reference pressure consisting of local pressure and hydrostatic pressure
β_i	Non-linear model fitting parameters
\hat{y}_{AC_PPG}	Non-linear fit estimating PPG amplitude for a given reference pressure
\bar{P}_S	Conditioned ring sensor estimated systolic blood pressure
\bar{P}_D	Conditioned ring sensor estimated diastolic blood pressure
$\bar{P}_{MAP,Finapres}$	Mean arterial pressure measured by the Finapres

Motorized Sensor Terms

A	Area of finger locally pressurized by sensor
F	Design loading for motorized sensor
P	Design pressure to be applied by motorized sensor
T	Torque required by motor for applying design loading
T_{stall}	Stall torque
D_p	Pitch diameter of threaded rod
Λ	Lead
μ	Coefficient of friction
d	DC motor barrel diameter
L	DC motor length

Chapter 1 Introduction

1.1 Background and Objectives

A truly wearable, ambulatory non-invasive blood pressure (NIBP) sensor – a sensor which is light-weight, compact, unobtrusive, and essentially unnoticeable to the patient -- could revolutionize healthcare, moving it out from the traditional walls of medical facilities so that patients would be cared for in their everyday surroundings. There is already substantial evidence that intensive tracking of blood pressure for a 24-hour period, using an oscillometric cuff-based device which makes measurements every 15 minutes or so, offers more meaningful data than traditional blood pressure measurement routines [1]. A reasonable conjecture is that a novel NIBP device which enabled long-term blood pressure measurements 24-hours per day could further enhance the ability to detect hypertension and optimize therapy, and ameliorate the massive health risks [2] associated with chronic hypertension. Wearable sensors, with wireless communication capabilities, could also provide vigilant management of individuals at risk for cardiovascular decompensation, such as chronic heart failure patients, patients convalescing at home, and individuals engaged in hazardous duties e.g. firefighters, soldiers, etc. Yet it is important that the long-term use of such a sensor be acceptable to patients, not interfering with their daily activities.

As of today, there are no truly wearable blood pressure sensors appropriate for long-term ambulatory use. Oscillometric cuffs, the most commonly used ambulatory devices, are bulky and can be very uncomfortable when worn for 24 hours in a row [3]. The Portapres, worn on a

patient's finger, employs the volume clamp method of Penaz. This device is bulky and its function causes total venous occlusion, so it cannot be used continuously for periods greater than an hour. Methods based on pulse wave velocity (PWV) have not proven to be robust [4] partly because it is non-trivial to measure accurate PWV and because PWV is a function of other physiologic factors beyond arterial pressure [5], [6]. Features in the photoplethysmogram (PPG) waveform, which can be measured by an ambulatory device [7], have been correlated with arterial blood pressure [8], but it is not clear that these relationships will be robust, considering the numerous factors which can affect the PPG signal, including non-linear optic phenomena and non-arterial oscillations (e.g. venous pulsations and fluctuations in capillary density) [9].

The goal of this thesis is to develop a monitoring platform which is capable of providing accurate, long-term non-invasive measurements of blood pressure. The technology is embodied in the form of a finger ring and combines information from the PPG with a novel hydrostatic-based implementation of cuffless oscillometry. The principle of hydrostatic oscillometry will be described and tested. Finite element modeling of the finger base and ring will be used to understand the influences of various structures on the accuracy of the device's measurements. A complete working prototype with data calibration and acquisition software will be benchmarked against a Finapres continuous blood pressure monitor.

1.2 Outline of Thesis

This thesis will discuss the principle and implementation of a hydrostatic approach to oscillometry. Chapter 2 provides a detailed discussion on the utility of the PPG for blood pressure measurements. An overview of the physiological connection between blood pressure and the measured waveform will be provided and will be followed by specific examples of

previous implementations of PPG-based blood pressure monitors. In chapter 3, the principle of hydrostatic oscillometry is detailed with a specific focus on a PPG-based implementation. A tetherless, accelerometer-based height sensor is presented which eliminates the need for more traditional fluid-filled tubing methods for height measurements. Chapter 4 next provides a complete description of a non-linear finite element model of the finger base as it is deformed by the ring. The model is separately validated by experimental stiffness measurements of the finger base as well as with MRI data collected while wearing the ring. Using the model, the proposed focally-applied pressure method for oscillometry is compared with more traditional circumferential pressure implementations. A sensitivity analysis of the method to changes in a variety of parameters are simulated and described. The focus of chapter 5 is on the physical implementation of the PPG-based blood pressure monitoring method. The design of the sensor unit is systematically broken down into each of the functional units and is accompanied by information detailing the basis for the various design choices. An algorithm for sensor registration is given for the purpose of reliably obtaining new sensor measurements. The algorithm is followed by a description of the Windows®-based acquisition GUI. Chapter 6 focuses on calibration of the blood pressure monitor. Using lessons learned during the development of the algorithm, a protocol is provided which has been shown to be effective for making reliable blood pressure measurements. In chapter 7, data from human subjects is presented which demonstrates the ability of the sensor to measure the blood pressure for a variety of healthy adults. Each of the blood pressure measurements are benchmarked against a simultaneous Finapres measurement with Bland-Altman statistics provided. Chapter 8 concludes the thesis by presenting a potential method for continuous blood pressure monitoring using the

ring sensor. Promising extended monitoring results are provided which demonstrate reliable tracking of the patient's mean blood pressure for nearly 10 minutes.

Chapter 2 Utility of the Photoplethysmogram

2.1 Physical Basis of the PPG Signal

The relationships illustrated in Figure 2 offer a framework for understanding the PPG. The PPG is a signal related to, but not equivalent to, simple *plethysmography*, the measure of tissue blood volume. Classic plethysmography measures, made with a strain gauge or a displacement tank [10], are democratic, with volume changes in various vessels of various tissues (e.g. skin, muscle, etc.) combined in a strictly additive fashion. Blood volume pulsations caused by the heart's beating occur in a number of vessel types, including large and small arteries, arterioles, and to a significantly lesser extent, venules and veins [11]. Capillaries and terminal arterioles are non-compliant [12,13] so these vessels do not contribute to the true plethysmograph.

2.1.1 Optics Considerations

Complicated optic phenomena distinguish the PPG from true plethysmography. In transmission mode photoplethysmography, tissue is irradiated by light typically provided by a light-emitting diode (LED), and the exiting light intensity is measured by a photodetector (PD) placed on the other side of the tissue (e.g. across a fingertip or an earlobe). Each pulse of blood entering the tissue increases the optical density (due to intravascular increases of erythrocytes and the light-absorbing hemoglobin they carry) of the illuminated tissue and decreases the light intensity at the PD. By convention, the PPG signal is inverted so that it positively correlates with

blood volume and inversely correlates with PD light intensity. Yet there is no simple quantitative relationship between blood volume, which is distributed throughout an irregular geometric network of vessels, and the fraction of emitted photons which successfully pass through the tissue. The light intensity is attenuated by optically significant tissue constituents, including oxygenated and de-oxygenated hemoglobin (in blood cells), myoglobin (in muscle), and cytochromes, as well as melatonin (in skin) and other compounds in bone and connective tissue [14] whose optic properties are wavelength dependent (Figure 1).

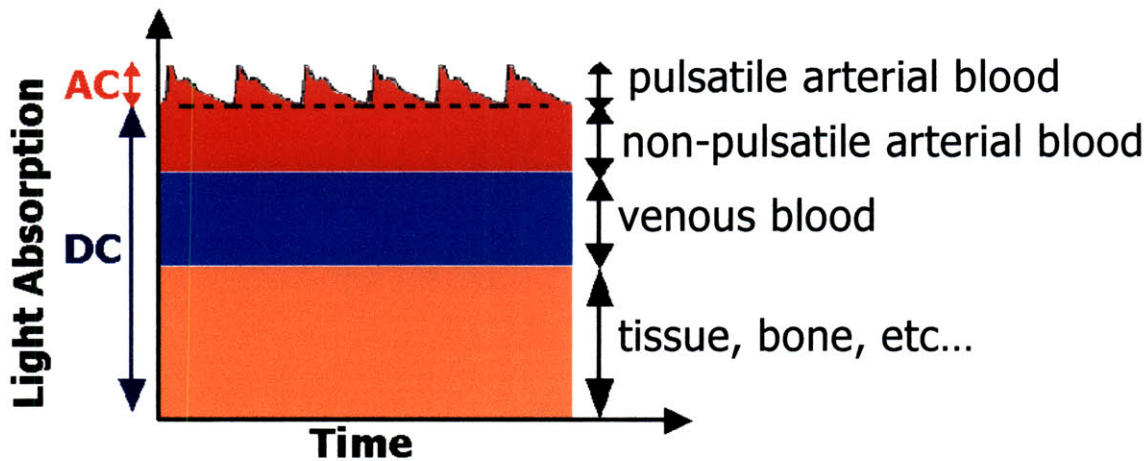


Figure 1: Illustrative representation of the relative photon absorbance for various sections of the finger.

Interestingly, the optical properties of whole blood are different from hemolysed blood, implying that the cell structure (e.g. cell wall) has optical properties distinct from its constituents [15], and even the walls of the blood vessels may be optically significant [16]. The Beer-Lambert law offers some quantitative insight about how blood volume will attenuate the incident light: if the blood were in a homogenous layer perpendicular to the light path, intensity would decay exponentially as a function of the thickness of the blood layer. This may be a reasonable approximation for a diffuse vascular bed, but perhaps less so when larger vessels contribute to the PPG signal [16]. The transmission PPG obtained from a finger pad or ear lobe is primarily

cutaneous given the lack of other highly vascularized tissues there [17], however the digital arteries contribute to a transmittance PPG from the finger base [18].

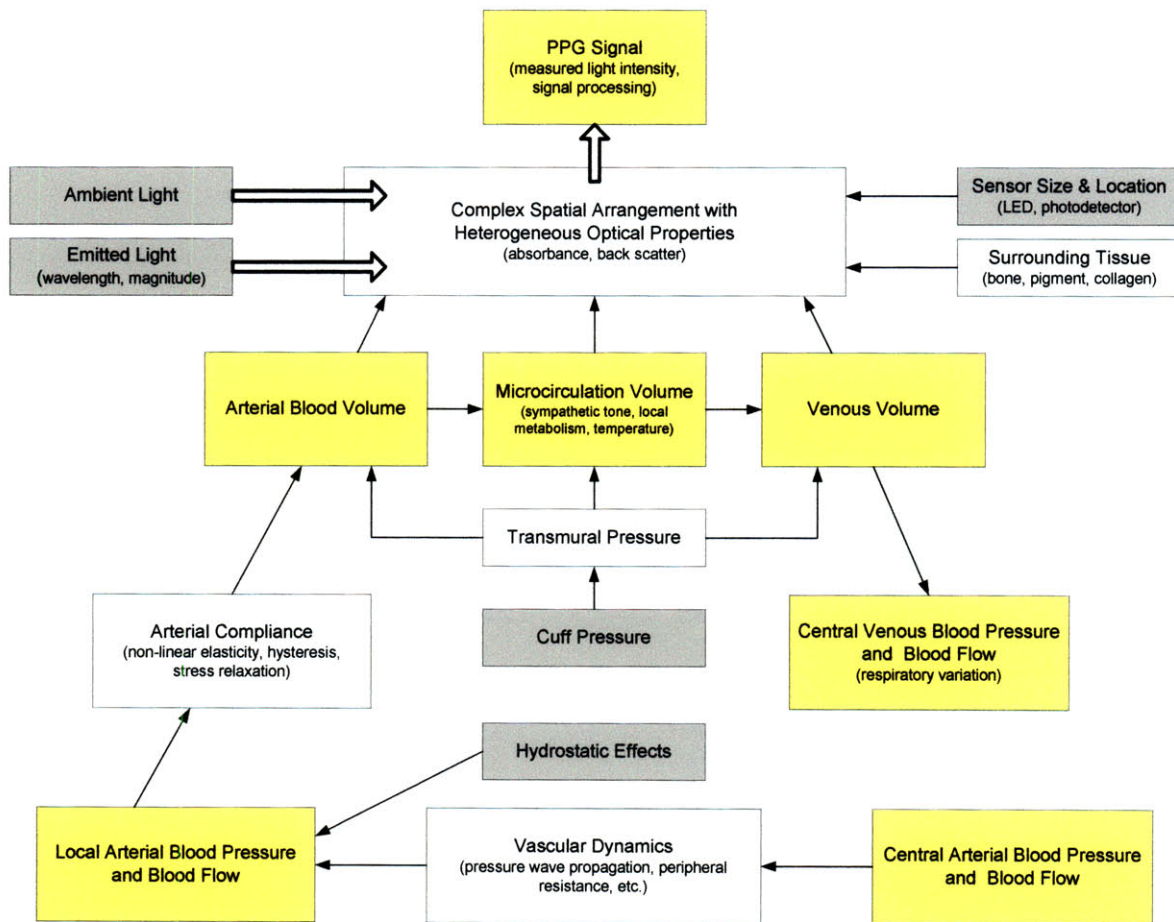


Figure 2: Hierarchy of the factors leading to a PPG signal.

Light propagation through a heterogeneous medium such as biological tissue has been the subject of extensive theoretical consideration [19,20]. In contrast to the simple exponential assumptions underlying the Beer-Lambert law, the actual geometry of tissue constituents can be very irregular, and the volume assayed by the PPG does not even have precise boundaries: tissue components along the primary optical path from LED to PD contribute more to the PPG signal, while those on the periphery are gradually less significant. Other light attenuating phenomena not considered by the Beer-Lambert relationship include reflection and scatter. The properties of

the LED (intensity, size, and location) and the PD (size, location, and photovoltaic properties) further complicate the relationship between blood volume and signal intensity. Therefore, the Beer-Lambert law does not accurately relate PPG and blood volume. However, it remains a useful starting point for many monitoring analyses.

Alternatively to transmission mode PPG, a photodetector can be placed alongside the light emitter and record the light which returns back from the tissue, known as a reflectance PPG. There is a paucity of emitted light that penetrates deeper than the skin and that returns to the PD. Analyses have suggested that the emitted photons that arrive at the PD follow a banana-shaped primary light path through the tissue, barely penetrating deeper than the skin. Under uncommon circumstances, reflectance PPG will demonstrate an *inverse* relationship with blood volume. This is because red cells are reflective, and can act as little mirrors. In vivo, this esoteric effect has been observed with reflectance PPG over a large artery [16], but in other studies, the standard PPG waveform demonstrated a positive correspondence with ultrasonic diameter measurements when placed over large superficial arteries [18]. In general, this effect is not perceptible in vivo: light reflection from deeper tissues serves to back-light blood vessels, and the more blood, the more light is attenuated by absorption, scatter, and refraction. Reflectance PPG is therefore quite similar to transmission PPG [9]. Because reflectance mode probes may not apply enough pressure to collapse the low-pressure venous system, venous volume oscillations (e.g. due to respiration) are typically more significant in reflectance mode PPG [21].

2.1.2 Physiological Considerations

Interestingly, the PPG is also a function of blood velocity, not just volume, probably because of re-orientation and/or packing of red cells [22,23]. In a rigid (e.g. constant volume) glass tube, pulsatile blood flow gives rise to a pulsatile PPG signal. Indeed, there are many classical

references to the PPG as a flow (rather than volume) measurement [14,18]. However, because pulsatile blood flow and pulse volume are highly coupled, it has been difficult to sort out the phenomena which result in the pulsatile PPG signal (e.g. AC component).

The notion that the PPG represents volumetric pulsations superimposed on a steady "baseline" signal (or "DC" component) may be misleading. In fact, the baseline PPG signal is time varying, displaying low frequency oscillations due to changes in capillary density (e.g. due to episodic sympathetic outflow [24,25] and local auto-regulation), and venous volume fluctuations (e.g. due to respiration-induced fluctuations in central venous pressure). Physiologic perturbations, such as temperature, metabolic state changes, or drug effects, cause local hyperemia or hypoemia, which can be tracked using PPG. Changes in ambient light can be a source of error in such applications if not properly accounted for by the device (e.g. if an instrumented hand moves away from an overhead light, less light reaches the PD so it may appear the digit is hyperemic). It should be noted that the PPG baseline level is not displayed by most commercial pulse-oximeters. In fact, the PPG signal is electronically processed to remove these baseline vacillations, which can also fundamentally alter the shape of each pulse [26].

2.2 Relating Plethysmography/PPG to ABP

It is natural to seek information about the ABP from a readily available PPG sensor. The arterial blood pressure and pulsatile changes in blood volume are highly coupled in the cardiovascular system, and based on observations that the morphology of the PPG is so similar to an arterial blood pressure (ABP) waveform, it is intuitive that they are related. This first requires consideration of the relationship between the ABP and classic plethysmography (see Figure 2). Overall, the pulsatile change of an arteries' diameter waveform is quite similar to the ABP

waveform, though the amplitude of diameter change, typically 1-5% of the baseline in adults, is much smaller than the respective pressure change, which is on the order of 50% [27]. Note that volume will be proportional to the square of a vessel's radius. There are two key phenomena which complicate the arterial pressure-volume relationship. First, as shown in Figure 3, on a beat-to-beat basis, it is more accurate to think of pressure-volume *loops* rather than static curves, because of hysteresis [28]. A step increase in arterial pressure leads to a secondary slower increase in blood volume over time, through vascular stress relaxation (at the same time, local microcirculatory feedback controls may attenuate the overall accumulation of blood in the tissue after the step increase); see Figure 3. The reverse occurs given a step decrease in arterial pressure. Second, arteries large [29] and small [30] are analogous to a stiff rubber hose, in that it requires pressure to either inflate or collapse the vessel from its unloaded set-point. Moreover, these vessels grow increasingly less compliant at extremes of pressure (e.g. non-linear compliance). Plotting arterial transmural pressure versus arterial volume yields a sigmoid-shaped curve.

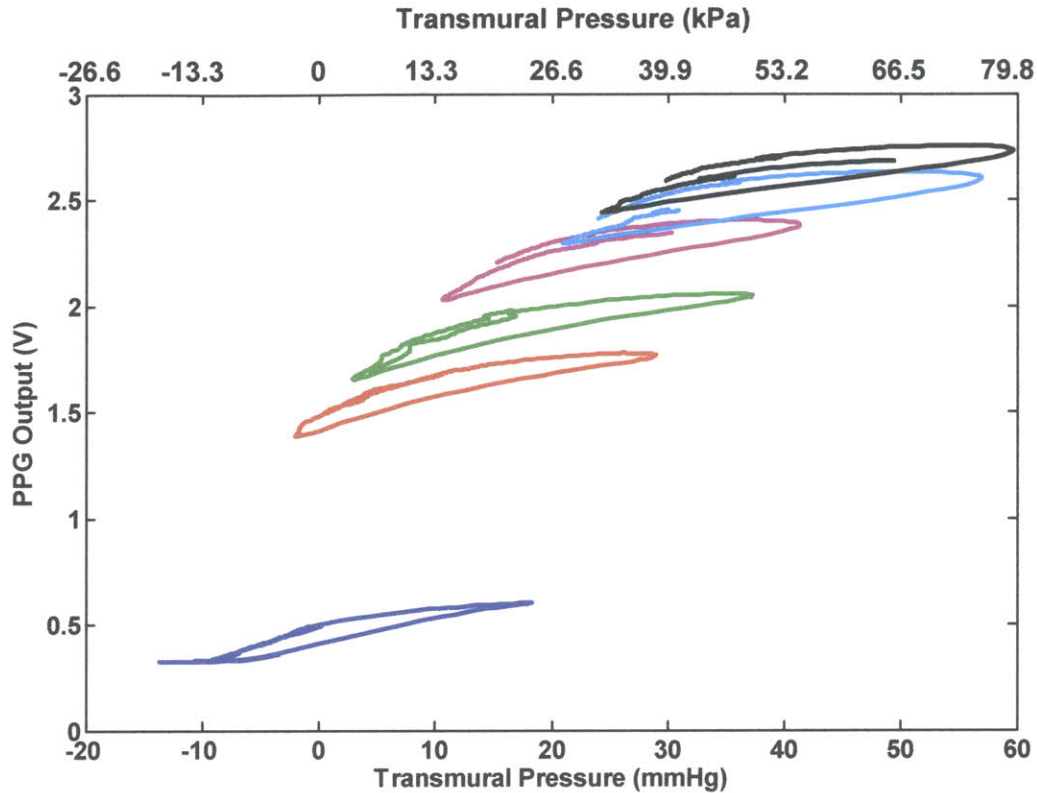


Figure 3: Plot of the pressure-volume (PPG-based) loops occurring over a range of applied transmural pressures.

In theory, high frequency components of the upstream pressure waveform will not propagate distally into the smaller branches of a vascular bed [31], and indeed, the PPG lacks some of the ABP's higher frequency components [32]. In addition, as previously noted, the PPG signal oscillates because of biologic variations in local capillary density and other non-arterial blood vessels. Still, though the PPG is not a true plethysmograph signal, it is similar enough that it possesses a similar relationship with transmural pressure: if the slower PPG baseline oscillations are mathematically removed, it has been shown that the PPG versus arterial pressure relationship is another sigmoid curve [33]. The specific shape of this PPG versus transmural pressure curve is sensitive to the subject's physiologic state. Also, it has been noted that the PPG waveform will change (both in amplitude and shape) as a function of externally applied pressure. This is

intuitive when you consider the sigmoid curve, and appreciate that it is the *transmural pressure* (internal pressure minus external pressure) which dictates vessels' volumes (see Figure 4 for explanation). Lastly, note that the slopes of the sigmoid pressure/volume curves are maximal at zero transmural pressure (e.g. maximal compliance), which is the basis for conventional oscillometric blood pressure measurement with a brachial cuff (when the external cuff pressure equals the mean arterial pressure).

2.3 Monitoring Applications

2.3.1 Arterial Blood Pressure from PPG

A variation, in which the PPG signal is used to determine when the volume pulsations are maximal, has been described [34]. Other computational devices to estimate ABP from PPG have included linear transfer functions and neural networks. Transfer functions are limited by their assumption that the relationship is linear and time-invariant. Neither method has been shown to be useful over a wide-range of physiologic states and subjects.

There have been a number of PPG waveform features which, in various investigations, correlated with central hemodynamic parameters. Features from the second derivative of the PPG have been correlated with vascular compliance. A measure of the PPG's systolic width correlated with mean arterial pressure. Another width feature correlated with left ventricular ejection time [35]. The "maximum decreasing systolic slope" correlated with peripheral vascular resistance [36]. Beat-to-beat variation in the level of the PPG has been shown to correlate with hypotension, hypovolemia, and wedge-pressure [37, 38, 39, 40]. When the PPG sensor apparatus does not collapse the veins, this effect may be enhanced by local venous volume oscillations caused by large, respiration-synchronous variations in central venous pressures [41]).

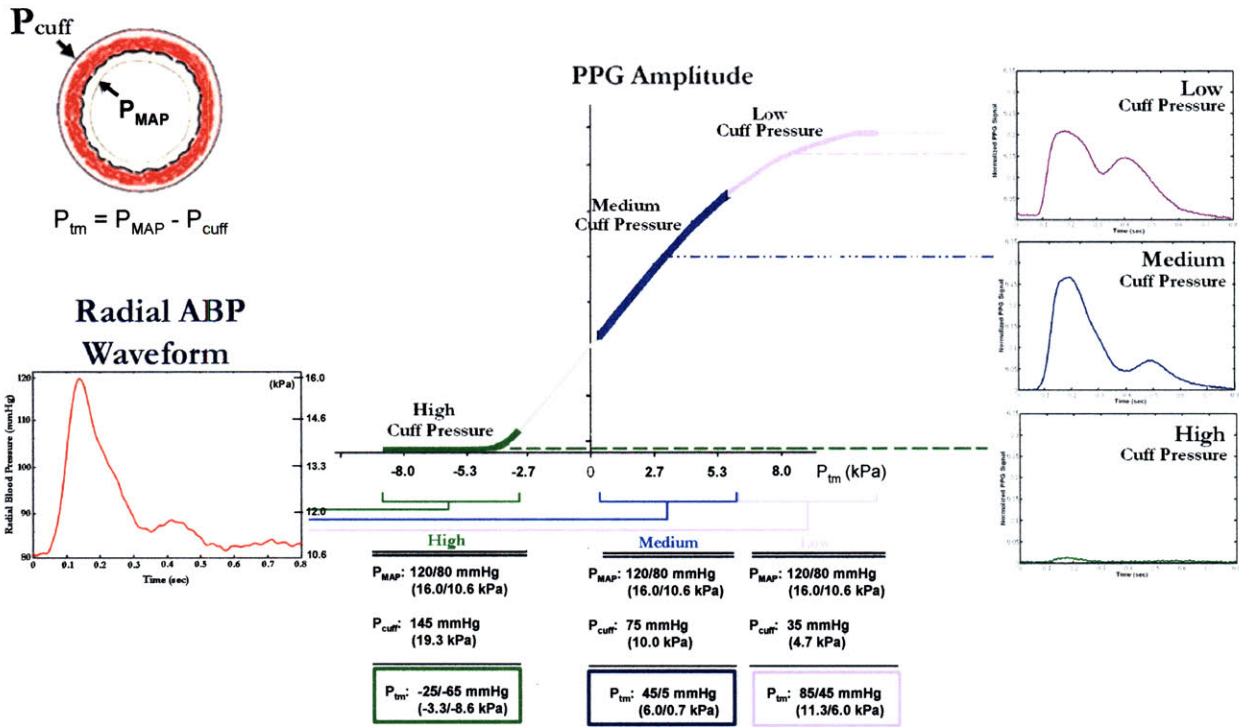


Figure 4: Illustration of the sigmoidal volume-transmural pressure relationship which governs the appearance of a PPG signal. When low external pressures are applied (large positive transmural pressure) the peaks of the waveform are distorted or saturated in appearance. As the cuff pressure is increased (transmural pressure approaches zero), the PPG waveform more closely approximates the underlying blood pressure waveform. For cuff pressures significantly larger than the internal blood pressure (large negative transmural pressure) there is almost no visible waveform as the vascular wall has been collapsed.

Such correlations should not be surprising given the paradigm that the transmission PPG is the ABP transformed by optical and vascular phenomena, all recapitulated in a sigmoid PPG / transmural pressure curve. What is important is to appreciate how a multitude of effects can confound any of the preceding PPG correlations, if not carefully controlled. For instance, it has been observed that the PPG amplitude may serve as a measure of depth of anesthesia, with higher amplitude indicating deeper anesthesia [42]. In practice, an increase in PPG amplitude could be caused by any one or more of the following, and the failure to expressly consider all of these confounding effects will lead to dangerous false positives and false negatives:

TABLE 1: FACTORS WHICH POTENTIALLY LEAD TO INCREASES IN THE AMPLITUDE OF A PPG WAVEFORM.

<i>Increase</i>	Arterial pulse pressure (common in the setting of bradycardia)
<i>Increase</i>	Arterial/arteriolar compliance due to drug effects or localized warming
<i>Increase/Decrease</i>	Height of the hand relative to the heart (changes arterial wall compliance)
<i>Decrease</i>	Mean arterial pressure (arterial compliance increases due to hypotension)
<i>Increase</i>	Ambient light
<i>Increase</i>	Optic density in the tissue due to oxygenation of chromophores

It is worth emphasizing that the correlation between a PPG waveform feature and any physiologic parameter will vary with different devices, because the PPG waveform displayed is a function of the manufacturer's post-processing algorithms, which can vary and are often proprietary.

2.3.2 PPG as a Binary Indicator of Pulsatile Perfusion

As a binary indicator of pulsatile flow, the PPG can also be used to measure the pulse travel time (PTT) between an upstream arterial pressure pulse and a more distal peripheral pulse. PTT is a function of pulse wave velocity (PWV), which is a function of blood pressure. There are three caveats which must be considered when utilizing PTT. First, to compute PTT, both a proximal and a distal measurement are necessary. Options for the proximal signal include an ECG, the sound of the mitral valve, or a proximal PPG or ABP signal. A true proximal coaxial signal is rarely available for the rigorous measurement of PTT along a length of artery, and the alternatives can introduce errors into the measurement. Second, the effective travel distance is also difficult to measure, so the PWV (distance divided by PTT) cannot be accurately computed. Third, the PWV is more accurately a function of arterial compliance, which is certainly a

function of blood pressure but also of the subject's arterial properties and physiologic state. These issues have been reviewed in detail [43, 44]. In summary, PTT correlates with blood pressure, but the relationship is complicated.

2.3.3 The Volume Clamp

The Finapres / Portapres uses the PPG to estimate ABP by applying the volume clamp method of Penaz, which exploits the following insight: if the PPG signal is not changing, neither is the arterial transmural pressure, and visa-versa. Using a rapid servo system with an inflatable finger cuff, the Finapres adjusts the pressure in the cuff to keep the reference PPG signal flat throughout systole and diastole; the method is thus known as the "volume-clamp". The servoed waveform of the cuff pressure which kept the PPG signal flat must be equal and opposite to the digital arterial ABP. The method is attractive in that it offers a truly non-invasive ABP measurement, though it requires somewhat bulky (and comparably expensive) instrumentation, it cannot be worn comfortably for long periods of time (the Portapres addresses this problem alternating measurements between neighboring fingers).

Chapter 3 Oscillometric ABP

Measurement with PPG

3.1 Oscillometric ABP Measurement with PPG

The basis of the oscillometric measurement method of mean arterial pressure is the following: when the external pressure, P_{OUT} , applied to an artery, is equal and opposite to the mean internal pressure, P_{IN} , then its volumetric pulsations are maximal in amplitude. This property stems from the typical arterial pressure-volume relationship, shown in Figure 5. Note that volume turns out to be a function of P_{tm} , the transmural pressure, where:

$$P_{tm} = P_{IN} - P_{OUT} \quad (1)$$

It is neither the internal nor the external pressure, but the balance between the two, which determines arterial volume. When internal and external pressures are in balance, the artery is most compliant: for a given pulsatile ΔP , there will be a corresponding maximal pulsatile ΔV . In conventional oscillometry, external pressure is systematically altered, typically by an inflatable cuff, until the maximal pulsatile ΔV is identified, and at that point, the mean internal arterial pressure can be assumed to equal the known external applied pressure.

The arterial volumetric change can be detected by noninvasive sensors, such as a PPG sensor placed near a palpable artery. Figure 6a illustrates a PPG sensor placed at the finger base, where a digital artery runs near the skin.

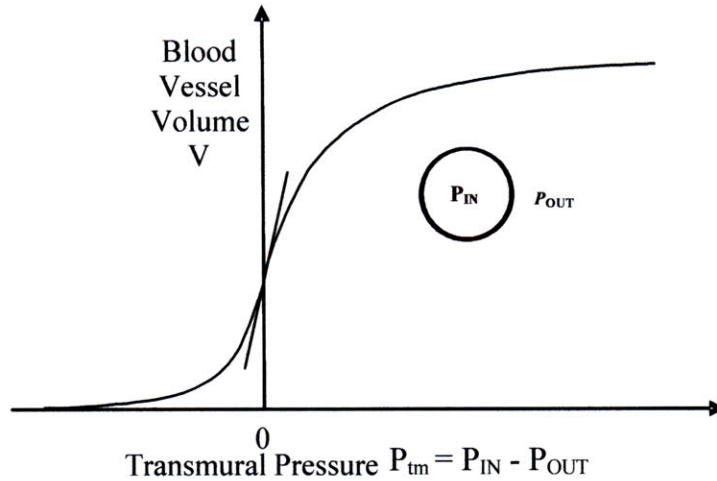


Figure 5: Sigmoidal compliance curve relating blood vessel volume change to transmural pressure [10].

The photons emitted by a light emitting diode (LED) are absorbed in part by the blood in the artery before reaching the photo detector (PD).

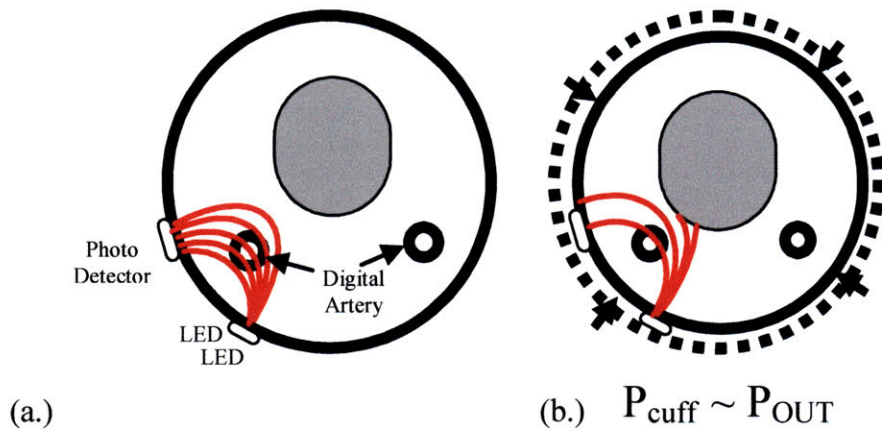


Figure 6: Finger cross-section with a PPG sensor. (a.) Illustration of basic PPG sensor principle; (b.) Illustration of how an increase in cuff pressure can affect the light paths of a PPG sensor. Changing the cuff pressure can change both the path length and the tissue sections illuminated by the sensor.

The output from the photo detector varies in response to the volumetric change of the palpable artery. It has been demonstrated that the amplitude of the PPG signal varies in relation to the transmural pressure P_{tm} , as shown in Figure 7 [45], [33]. Note that this curve is very similar in

shape to the gradient of the curve in Figure 5. The highest point of the PPG amplitude corresponds closely to the zero transmural pressure point. Therefore, an oscillometric device may alternatively employ the PPG as an indicator when pulsatile ΔV is maximum and $P_{tm} = 0$.

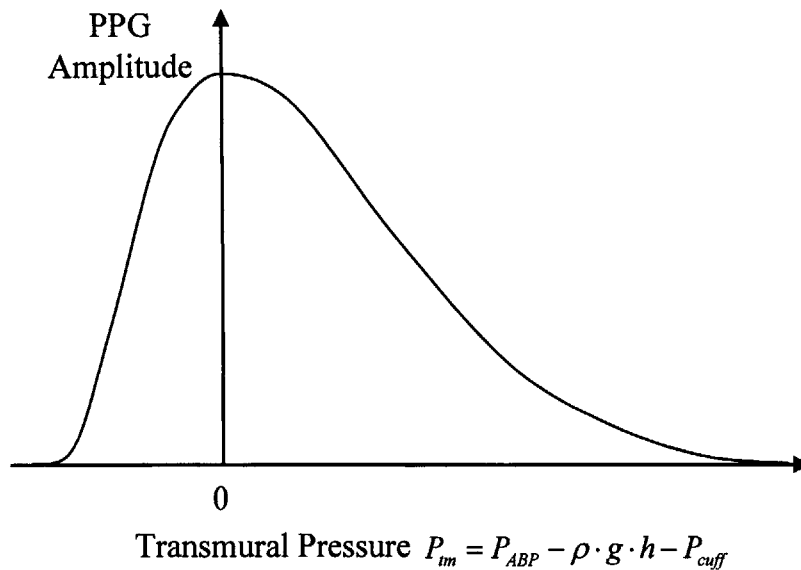


Figure 7: PPG amplitude against transmural pressure.

3.2 Hydrostatic Pressure Challenge

Blood pressure is normally measured at the proximal aorta, so if a blood pressure measurement is made at a location that is higher or lower than the heart, it is necessary to correct for hydrostatic pressure effects. The pressure inside the artery is then given by

$$P_{IN} = P_{ABP} - \rho \cdot g \cdot h \quad (2)$$

where P_{ABP} is the proximal aortic pressure, ρ is the density of the blood, g is the acceleration of gravity, and h is the height offset of the measurement site relative to the proximal aorta. See

Figure 8. Including this hydrostatic pressure $P_{hyd} = -\rho \cdot g \cdot h$ acting inside the blood vessel, the transmural pressure is given by

$$P_{tm} = P_{ABP} - \rho \cdot g \cdot h - P_{cuff} \quad (3)$$

where P_{cuff} is the pressure created by a cuff which is transmitted to the outer surface of the blood vessel, P_{OUT} . Typically any height offset between the measurement site and the heart is a potential source of error, when not properly accounted for. However, note that the external pressure, P_{cuff} , and the hydrostatic pressure, P_{hyd} , play the same role; the former pressurizes the blood vessel from outside, while the latter does so from inside. Provided one is carefully measuring the height of the sensor, it is possible to alter P_{tm} by controlled alterations in P_{hyd} , without any alterations in P_{cuff} .

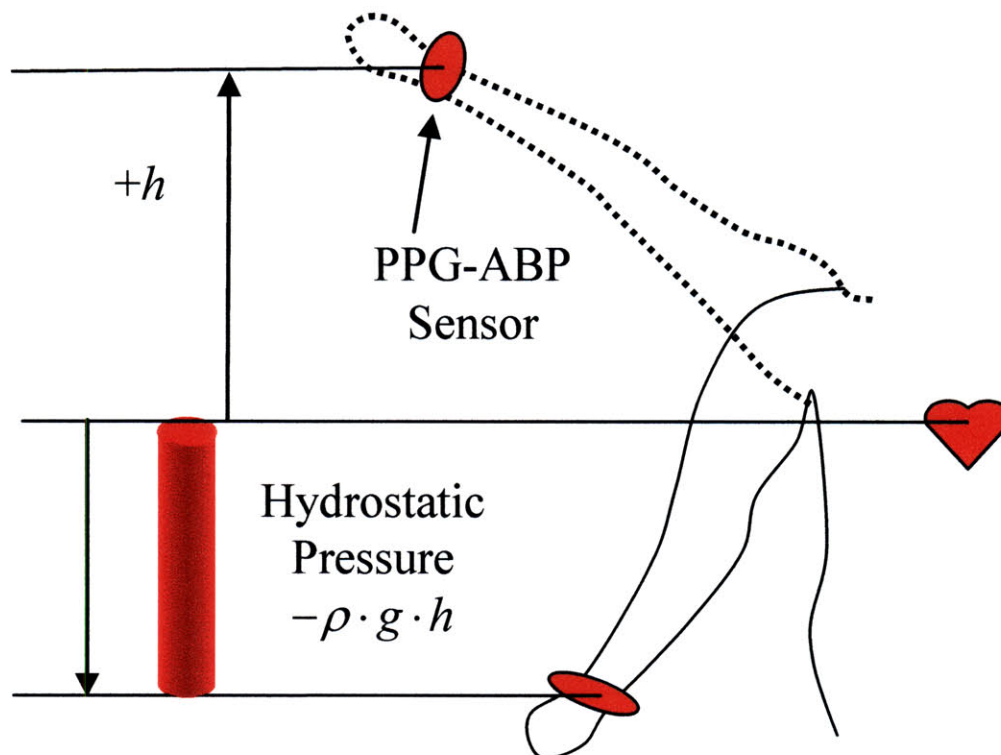


Figure 8: Hydrostatic pressure due to the arm height. Positive h points upwards. When lowered below the heart, $h < 0$ and the bottom hydrostatic pressure is $-\rho gh > 0$.

Based on this equivalence between the external pressure altering P_{tm} using an inflatable cuff and the internal pressure altering P_{tm} via hydrostatic pressure challenge, the following MAP measurement method, named the hydrostatic challenge protocol, is devised:

1. The instrumented arm is raised so that the transmural pressure P_{tm} is varied near its zero value (MAP).
2. A relatively low pressure is applied locally to a palpable artery and is measured by a pressure sensor;
3. The amplitude of the PPG signal is examined to find the zero P_{tm} point.

Let \bar{y}_{AC_PPG} be the amplitude of a PPG signal, which varies as the arm is raised, that is, as the height h varies. Assuming that the PPG amplitude takes a maximum within the reach of the arm, the sensor height associated with the maximum PPG amplitude is determined as

$$h_{zero_P_{tm}} = \arg \underset{h}{Max} [\bar{y}_{AC_PPG}] \quad (4)$$

Using this height of zero transmural pressure, the mean arterial pressure P_{MAP} is given by

$$P_{MAP} \cong \rho \cdot g \cdot h_{zero_P_{tm}} + P_{cuff} \quad (5)$$

where P_{cuff} is the relatively low pressure applied to the palpable artery.

This MAP measurement based on the hydrostatic challenge protocol has a few salient features:

- Since the transmural pressure is altered by the hydrostatic pressure, the cuff pressure does not have to be raised too much; it can be as low as 50 ~ 70 mmHg to achieve the zero transmural pressure condition, as shown later in the experiment section.

- Unlike traditional oscillometric ABP measurements, the cuff pressure can be kept constant and, thereby, no actuator is needed for inflating the cuff. Eliminating the inflation of the cuff reduces interference with daily activities, making the sensor wearable for a long period of time. Furthermore, eliminating an actuator reduces the consumption of battery power, an important requirement for wearable sensor design.

- Keeping the cuff pressure constant reduces the artifact of PPG due to mechanical interferences caused by the cuff. As illustrated in Figure 6b, the traditional method varies the cuff pressure surrounding the entire finger cross section. It can be seen that, as the cuff pressure varies, the optical path between the LED and the photo detector is altered; as the cuff pressure increases, the light path gets shorter and, thereby, the PPG output is affected. On the other hand, if the cuff pressure is kept constant, it does not alter the optical path; hence the PPG amplitude reflects the net volumetric change due to hydrostatic pressure challenges. This makes the PPG signal stable and usable for oscillometric ABP measurements.

Chapter 4 Theoretical Analysis of Sensor- Artery Interaction

Because we are now applying a localized pressure to the surface of the finger several key questions must be answered to verify both the long-term wearability of the sensor and the accuracy of the blood pressure measurements which it provides. The goal of our modeling is to better understand the following questions: (1) should the local pressure interfere with blood flow away from the ring; (2) is the design robust to ring misalignments; (3) is the surface pressure the same as the external pressure at the artery; (4) is the design insensitive to changes in tissue compliance? To this end, finite element (FE) modeling techniques were utilized to investigate an anatomically realistic model of a finger base consisting of a rigid bone, malleable tissue, and a pressurized artery. First, the procedure utilized to develop the model is described. This procedure includes the selection of the model components and geometries, the material properties, and the boundary and loading conditions of the model. Next, the simulation results are compared to a magnetic resonance (MR) image of a normal and deformed finger base. The MR images will be accompanied by experimentally measured tissue stiffness data for model validation. Finally, the questions above related to the ring sensor design are explored and the section is concluded with a discussion on the findings and limitations of the implemented FE model.

4.1 Formulating the Finite Element Model

For reference, an axial view of the current blood pressure sensor prototype being worn by a subject is provided in Figure 9.

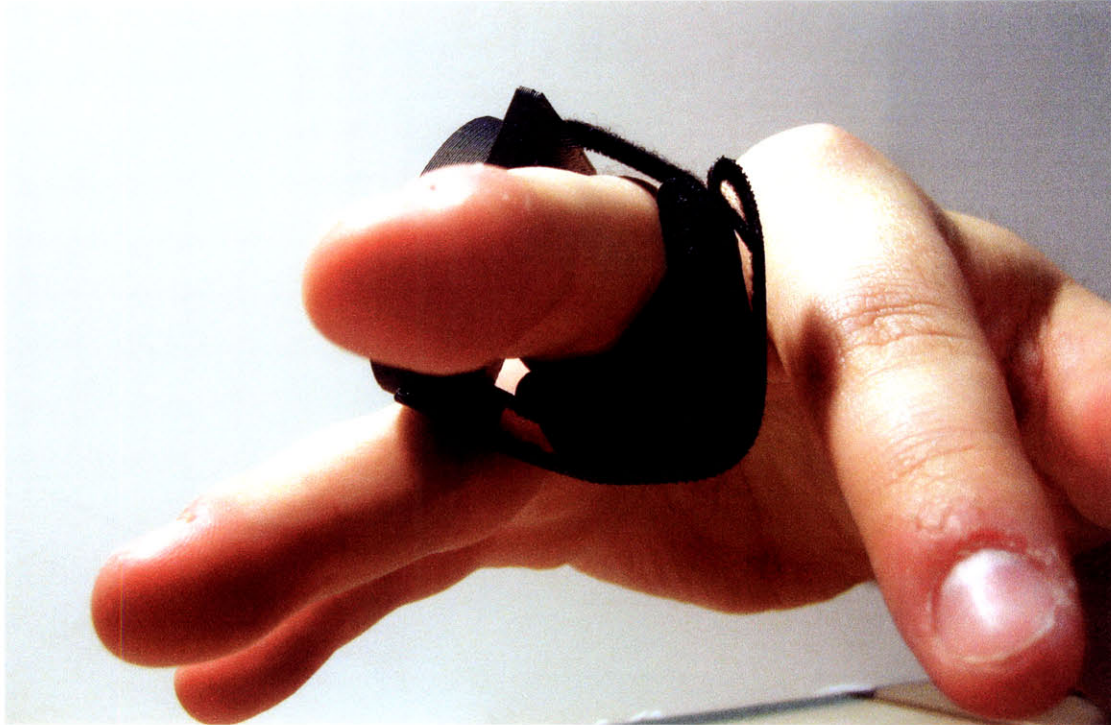


Figure 9: Photograph of the sensor unit worn at the finger base by a research subject.

Finite element packages are useful tools capable of transferring complex physical problems into tractable mathematical models. By assigning assumed model geometries, material properties, and boundary and loading conditions, it is possible to obtain a set of solutions which can be used to analyze and refine complex engineering design problems. For our analysis, a continuum model of the finger base and ring sensor is divided into a large number of discrete elements and nodes. The prescribed external loading conditions are applied to the surface element nodes. The results of this loading, in combination with the model's boundary conditions, are transmitted through the model via the governing equilibrium equations.

The stresses and strains which result for each of the nodes and elements satisfy the existing compatibility requirements and represent the solutions to a set of simultaneously solved algebraic equations. It should be noted that the resulting solutions only satisfy the equilibrium equations at the nodal points and across each element. Consequently, the stresses between elements within a coarse element mesh must be evaluated to ensure sufficient accuracy of the results. As the model's mesh is refined the solution will approach the continuum solution, provided the initial model assumptions accurately capture the true physical system. However, a finer mesh requires significantly more computing time for analysis. To this end, it is essential to refine the model to the minimum point where confidence is attained yet computation time is also minimized. Once this level of model refinement has been achieved, it is possible to perform simulations on a variety of input loading conditions.

For our analysis, we will focus on a 2-D cross section of an average human finger base as shown by the cut plane in Figure 10. The loading conditions created by contacting surfaces will be prescribed by a simplified geometry illustrated in Figure 11.

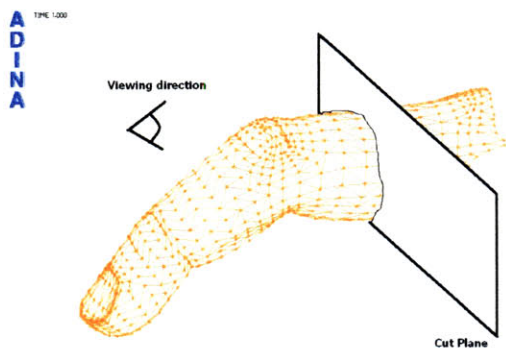


Figure 10: Finger cross-section imported into ADINA.

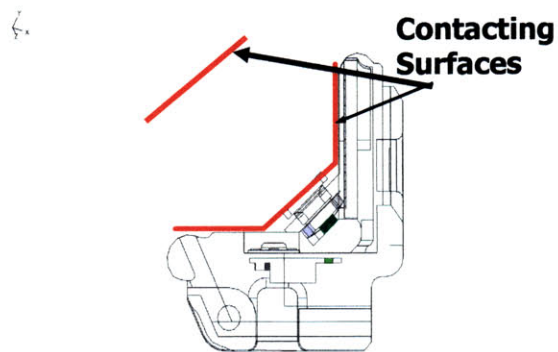


Figure 11: Illustration of the contacting surface utilized in our finite element model.

4.1.1 Model Formulation: Anatomical Component Selection

The actual geometry of the finger is quite complex and varies from human subject to human subject. However, generalized models of the fingertip and finger base have been successfully employed by various researchers [46], [47]. A typical finger is composed of three main types of soft tissue: the epidermis, dermis, and cutaneous fat (Figure 12).

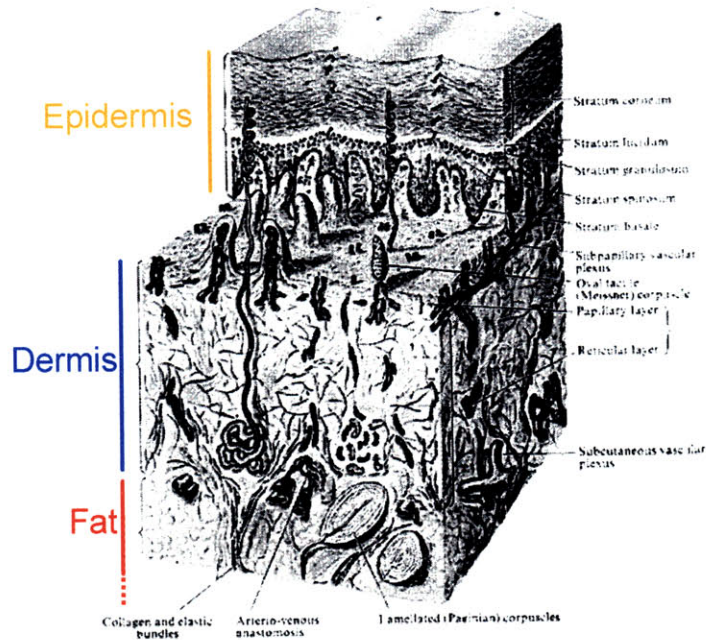


Figure 12: Illustration of a cross section of human skin [48].

The epidermis consists of four main layers: the stratum corneum, the basal layer, the malpighian layer, and the granular layer. The function of this component of the skin is to prevent water losses as well as to regulate the body temperature. The flexible dermis is located below the epidermis and consists of mainly water and elastic materials (elastin, collagen, and ground substance). The dermal layer provides support and elasticity to skin [49]. The layer of cutaneous fat consists of adipose tissue which is utilized for both energy storage as well as protective cushioning.

In addition to the soft tissue, the finger contains more rigid elements which provide support (bone) and enable function (tendons, blood vessels). A sagittal cross section of the finger illustrates several of the relevant anatomical features of the finger (Figure 13).

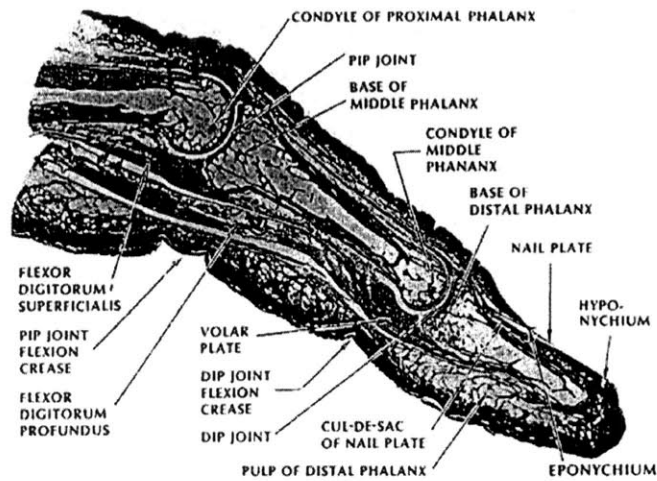


Figure 13: Sagittal cross section of a human finger [50].

We contend that the relevant components for generating the complex arterial wall loading conditions consist of the soft tissue elements, the digital artery, and the more rigid tendon and bone. Specifically, we theorize that an applied surface load is transmitted through the soft tissues to the arterial wall and ultimately to the rigid support structures. It is this complex interplay which ultimately defines the deformation mechanisms of the arterial wall for focally applied external loadings.

4.1.2 Model Formulation: Geometry Selection

A typical finger base cross-section, when viewed staring down the length of the finger is approximately oval shaped and is roughly symmetric about the local midsagittal plane (Figure 14, Figure 15).

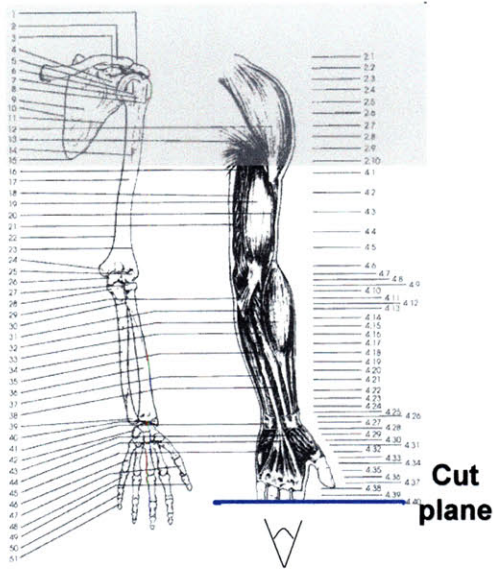


Figure 14: Sketch illustrating the location of the cutting plane used to create the finger slice to the right.

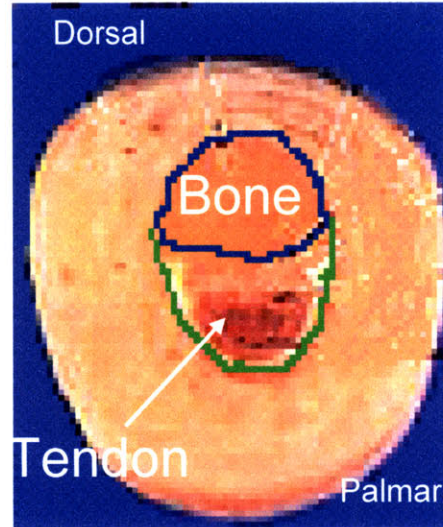


Figure 15: Cross-sectional slice of the right hand at the finger base of a cadaver [51].

In modeling the finger base, we have attempted to capture the relevant structural information wherever possible. We have assumed that the bone is symmetric about both the midsagittal plane and the transverse plane. We have further assumed that the location of the bone is laterally symmetric within the finger base, but is centered vertically, slightly above the finger base’s center of mass. The tendon is symmetric about the midsagittal plane and is located near the bone. As will be detailed more specifically, two models were created for the tendon (Figure 16).

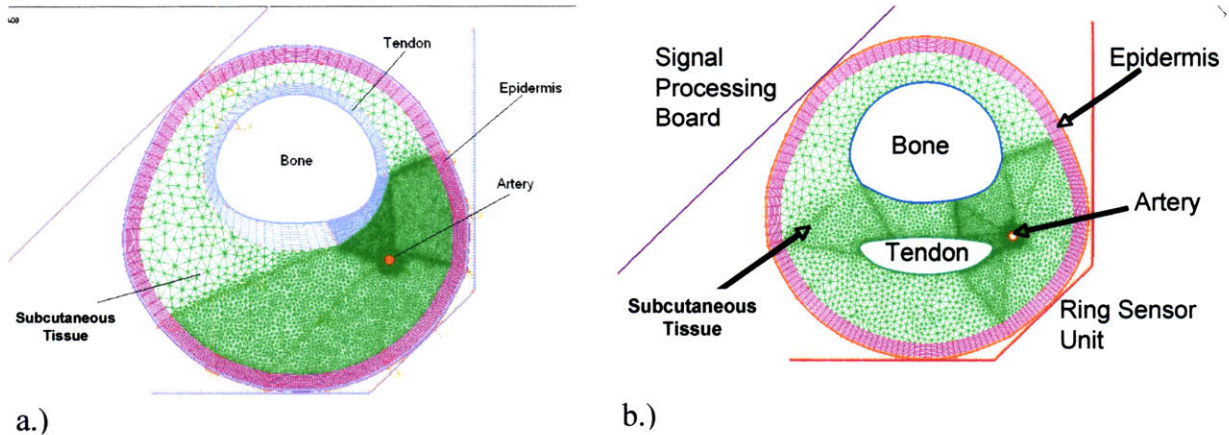


Figure 16: Complete finite element models of the finger base. a.) The tendon is modeled as a nearly rigid material surrounding the bone; b.) The tendon extends far below the bone and is rigid in structure.

The dimensions of the relevant model components are as follows: the finger base is taken to be 1.8 cm in diameter; the bone is taken to be 8 mm across and centered 2 mm above the center of the finger base; a single artery is located 1.5 mm below and 6 mm to the right of the center of the bone and is assumed to have a diameter of 0.5 mm and a wall thickness of 0.1 mm. The ratio of the arterial diameter to wall thickness was chosen based on measured values for radial arteries and arterioles [52]. It has been tacitly assumed that a digital artery will have properties between these two vessel types. The first model consists of the tendon wrapped tightly around the bone and appears to be somewhat contrary to the cross section shown in Figure 15. However, a closer examination of the anatomy demonstrates that the tendon is tightly coupled to the bone (Figure 17). For this reason, a model was proposed which did include the tight anatomical coupling.

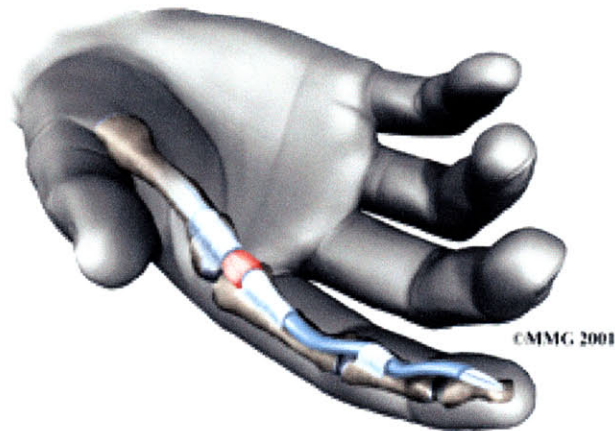


Figure 17: Illustration of how the tendon is tightly coupled to the bone through wrapping [53].

For the second implementation of the model, the tendon was positioned approximately 2 mm below the bone and has a diameter of 7 mm. This second implementation treats the tendon and bone as separate rigid structures within the finger which are capable of independently supporting loads.

The skin, although clearly made of layers which are inhomogeneous, anisotropic, and non-linear, has previously been modeled as a succession of homogenous, linear, isotropic layers under carefully controlled loading conditions [54]. The epidermal layer is roughly 800 μm thick and completely surrounds the underlying dermis and cutaneous fat layer [55], [56]. For this work, we have lumped the dermis and cutaneous fat together into a single “subcutaneous” layer. Although these layers provide unique functionality within the finger, their mechanical properties under specific loading conditions are similar enough that the lumping of these layers is reasonable and has been previously suggested by other authors [57].

4.1.3 Model Formulation: Material Selection

Since the deformation of the arterial wall is essential to our analysis, care has been taken in the selection of the appropriate non-linear compliance model. The selected arterial model is based on an Ogden rubber/foam material and encapsulates the gross combined behavior of the various constituents of the arterial wall (Figure 18). An Ogden material is typically selected to characterize an incompressible, isotropic, nonlinear material, such as rubber.

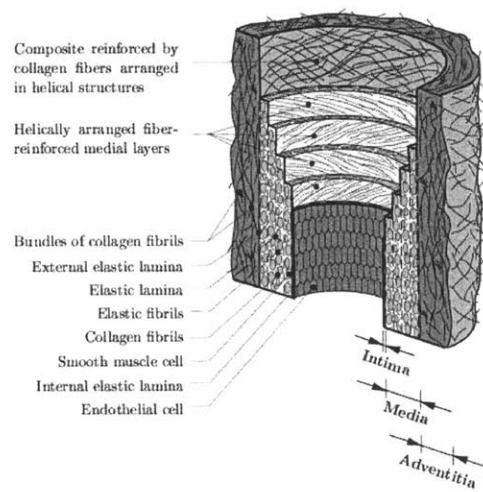


Figure 18: Illustration of the various components comprising a typical arterial wall.

The actual properties of the material are based on experimental data acquired by Sato, *et al* [58]. Stress and stretch data points were taken from the experimental results and a least squares algorithm in ADINA was then utilized to estimate the appropriate model coefficients for the material (Figure 19). The choice of this particular model type has been proposed by several other authors, including Bathe [59] and Tang [60]. The Ogden model is based on the assumption that the strain energy density function assumes the form:

$$W = \sum_{n=1}^9 \frac{\mu_n}{\alpha_n} [\lambda_1^{\alpha_n} + \lambda_2^{\alpha_n} + \lambda_3^{\alpha_n} - 3] \quad (6)$$

where μ_n and α_n are the Ogden material constants, and λ_i 's are the principal values of the stretch tensor. A plot of the resulting non-linear model is provided in Figure 19.

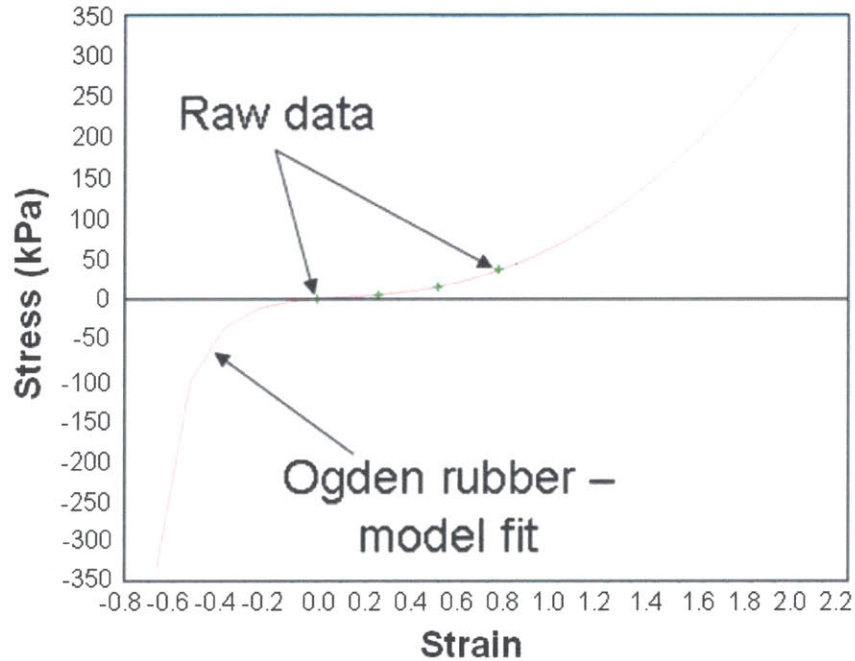


Figure 19: Plot of an Ogden model fit to arterial wall stress-strain data provided by Sato, et. al. The above compliance curve defines the non-linear compliance characteristics of the modeled arterial wall.

Although, as we mentioned previously, most biological tissue is non-linear in nature, we will make certain assumptions about the various components of the model to facilitate our analysis. For this model we will use a plane strain approximation and assume that the skin and fascia surrounding the bone can be represented as homogeneous, linear elastic, isotropic materials. Our linear elastic assumption is reasonable for relatively small strains but must be modified if large displacements are applied. Since we are representing the soft tissue with linear elements, the mechanical properties of each soft tissue layer are completely defined for static

analyses such as this when the Young's modulus and Poisson's ratio are provided. To our knowledge, no experimental data exists on the Poisson's ratio of *in vivo* skin, however all materials are assumed to have a Poisson's ratio of approximately 0.5 (implemented $\nu = 0.49$) on the assumption that the compression takes place in a relatively short period of time; a time scale which is too short to allow the interstitial fluid to be redistributed. This modeling assumption is consistent with previous publications [57], [61]. It must be noted at this point that the reason for using a Poisson value slightly less than 0.5 is necessary to minimize the likelihood of numerical instabilities resulting from the compliance matrix for plane strain systems, specifically the $(1-2\nu)$ factor which is found in the denominator of all elements of the matrix. Clearly as a Poisson ratio value approaches 0.5 numerical solvers will have difficulty working with a denominator value approaching 0.

Based on previous experimentally driven numerical analyses, the epidermis is estimated to have an elastic modulus between 0.12-0.24 MPa [62]. For this work a Young's modulus of 0.15 MPa was selected. As was previously stated, the dermis and cutaneous fat layers have been combined into a single layer of soft tissue because of their overall similar static responses to mechanical stimuli. This method of combining the layers has been suggested by several authors resulting in typical modulus of elasticity values between 0.001 MPa – 0.1 MPa [46], [57], [63]. Rhee attempted to estimate the elastic modulus by comparing published experimental data of finger volume changes under known loading conditions, from Yamakoshi, *et al* [64], with finite element simulations of a simplified cylindrical finger model. For this work, a mean value of 0.055 MPa was implemented for the subcutaneous layer. This value was near the middle of the reported elastic modulus values and roughly followed Dandekar and Srinivasan's

recommendation of the use of a 10:1 modulus ratio between the epidermis and subcutaneous layers.

The bone is assumed to be a completely rigid and incompressible member of the finger and consequently is not meshed, but instead serves as a boundary within the tissue. This assumption is reasonable as the elastic modulus for typical skeletal bone is on the order of over 10 GPa, or 10^4 times more stiff than the soft tissue of the finger [65]. The tendon may also be treated as essentially a rigid body within the finger as the published elastic modulus is on the order of 1 GPa [66]. A complete summary of the parameters utilized in the model can be found in Table 2.

TABLE 2: SUMMARY OF SMALL DEFORMATION FEM PARAMETERS

Element	Parameter Values			
	Dimensions [mm]	Material	E [MPa]	ν
Subcutaneous Tissue	$\phi = 18$	Linear, elastic	0.055	0.49
Epidermis	$\phi = 19.6$	Linear, elastic	0.010	0.49
Artery	$\phi = 0.5, h = 0.1$	Ogden Rubber	-	0.49
Tendon	$\phi = 9$	Linear, elastic	1.000	0.49
Bone	$\phi = 8$	Rigid	-	-

4.1.4 Model Formulation: Boundary Selection and Loading

As was stated previously, the bone will be considered to be a rigid boundary within the tissue; the tissue elements surrounding the bone, therefore, will be fixed in space. A rigid contact boundary is applied to the upper left side of the finger which represents the circuit board holder. A second contact boundary, representing the ring sensor, is applied to the finger directly opposite to the circuit board holder (Figure 16). For our model, only y-translations and z-translations are allowed, i.e. only in-plane displacements occur. The disturbance applied to the

tissue is initially modeled as a 2.5 mm displacement occurring at the edge of the finger base and focused in towards the artery and bone. Specifically, the two analytically rigid contact surfaces are simultaneously displaced inward towards the center of the finger with a total displacement of 2.5 mm. The model is oriented such that the applied displacement occurs along only the z-axis. Additionally, a pulsatile pressure is prescribed about the internal wall of the artery to simulate the pulsatile conditions. The prescribed pressure consists of a physiologically realistic mean pressure of 11,970 Pa (90 mmHg) with a superimposed single frequency sinusoidal pressure of $\pm 2,660$ Pa (± 20 mmHg). The main limitation of prescribing a pressure load will be an inability to capture arterial blood flow changes or dynamic fluid stresses. Additionally, we will neglect wall collapse mechanics. Since our interest is focused towards capturing static pressure propagations prior to arterial wall collapse these limitations are acceptable.

4.1.5 Model Formulation: Meshing Method

The non-linear nature of the arterial wall necessitates a careful mesh implementation. For this study the following meshing scheme was utilized:

- The artery was meshed with 600 low aspect ratio 9-node elements. The nearly square nature of the elements is optimal for large deformations and minimizes errors associated with grossly distorted element geometries.
- The tissue immediately surrounding the artery consisted of 600 9-node linear elastic elements with the same low aspect ratio as was used for the artery. In order to minimize numerical errors or stress jumps developed at the material change interface it is essential to both develop a fine mesh and to match the aspect ratio of the mesh as closely as possible.

- The remaining subcutaneous tissue within the finger was meshed with a free-form Delaunay algorithm with each element containing 8 nodes.
- The epidermis and tendon were both meshed with 9-node quadrilateral elements with a higher element density preferentially located near the ring sensor contact location.
- Finally, it should be noted that the rigid contact surfaces were defined to be 2-D planar types with a mesh density of 200 segments and the default ADINA contact rules.

The solution process implemented for the model consisted of step sizes of 0.001 with automatic alteration of step size allowed for non-convergent solutions. Additionally, to improve the convergence of the model, matrix stabilization was utilized with a solution process consisting of optimizing energy and force results.

4.2 Validating the Finite Element Model

4.2.1 MRI Studies

Finite element model validation with experimentally obtained data is important for any detailed simulation. Since it is extraordinarily difficult to obtain *in vivo* finger base stress and strain data directly alternative visualization methods must be pursued. To this end, specially acquired Magnetic Resonance Images (MRI) of a finger base deformed locally by the ring will be utilized to guide our model development. The main advantage of the MRI modality is the ability to resolve and differentiate the soft tissues of the finger while under static external loading conditions. Voss and Srinivasan [67] published several MRI images of a *finger tip* under various loading conditions. These images are useful in visualizing both the internal anatomy at the periphery as well as for predicting the effects of applied deformations (Figure 20).

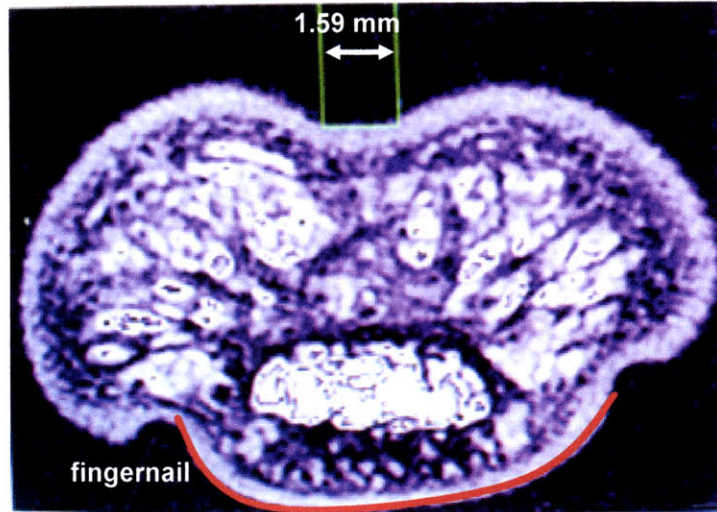


Figure 20: MRI image of a deformed fingerpad while loaded with a 1mm prescribed surface displacement [67].

We additionally pursued our own MRI studies, specifically targeting the general deformation of both the finger base and the digital artery when the proposed ring sensor design was attached. Figure 21 provides a T1-weighted image of a normal, undeformed finger base while Figure 22 shows a finger base significantly deformed by the ring sensor.

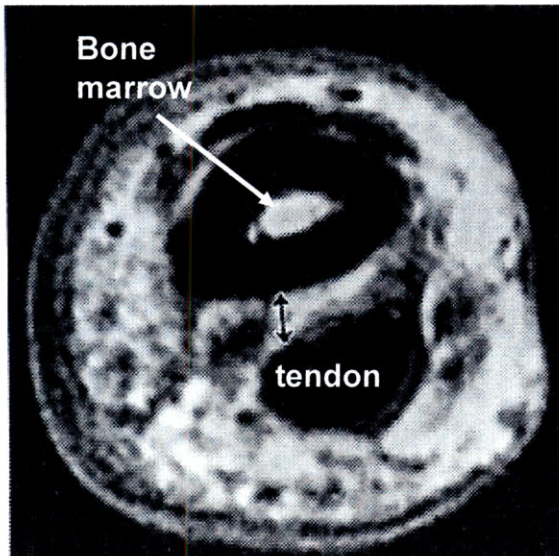


Figure 21: T1-weighted MRI of normal finger base [68].

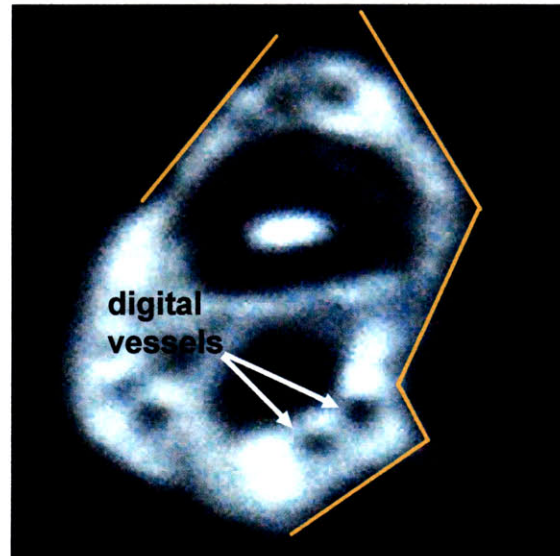


Figure 22: T1-weighted MRI of finger base deformed by passively loaded ring sensor.

Note the significant redistribution of the subcutaneous tissue in the deformed finger base image. The MRI indicates that although the tissue of the finger distorts significantly, the location of the tendon relative to the bone does not appear to change significantly. Figure 23 contains a clearer view of the ring sensor relative to the finger for a large deformation. From these figures, we anticipate that the FE models will demonstrate an increase in the amount of tissue away from the focally applied pressure. We also note that the location of the tendon relative to the bone appears to remain relatively unchanged by the large deformation. This finding gives us confidence that our assumption of treating the bone and tendon as approximately a single unit is valid for this analysis. However, we also note that the model will likely not capture the fluidic behavior of the subcutaneous tissue. The results of this limitation will likely be manifested as smaller tissue deformations and perhaps slight overestimations in internal pressures.

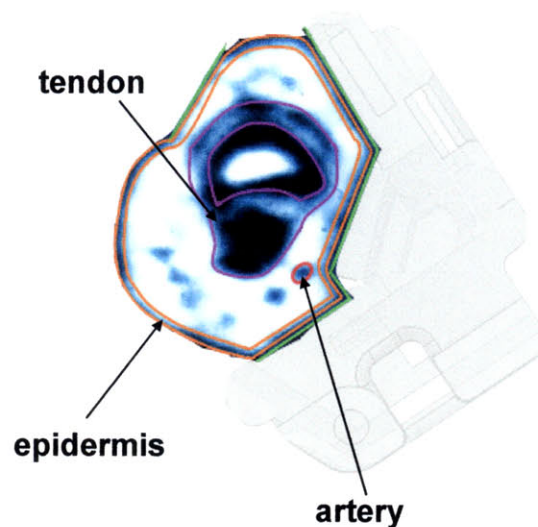


Figure 23: Labeled MRI of a deformed finger base with the ring sensor for reference.

4.2.2 Experimental Tissue Stiffness Measurements

Measurements of the global stiffness of the finger base were recorded by simultaneously measuring a prescribed displacement and the resulting pressure at the surface of the finger. Specifically, volunteers placed their fingers between the ring sensor, attached to a movable stage, and a rigid contact surface (Figure 24).

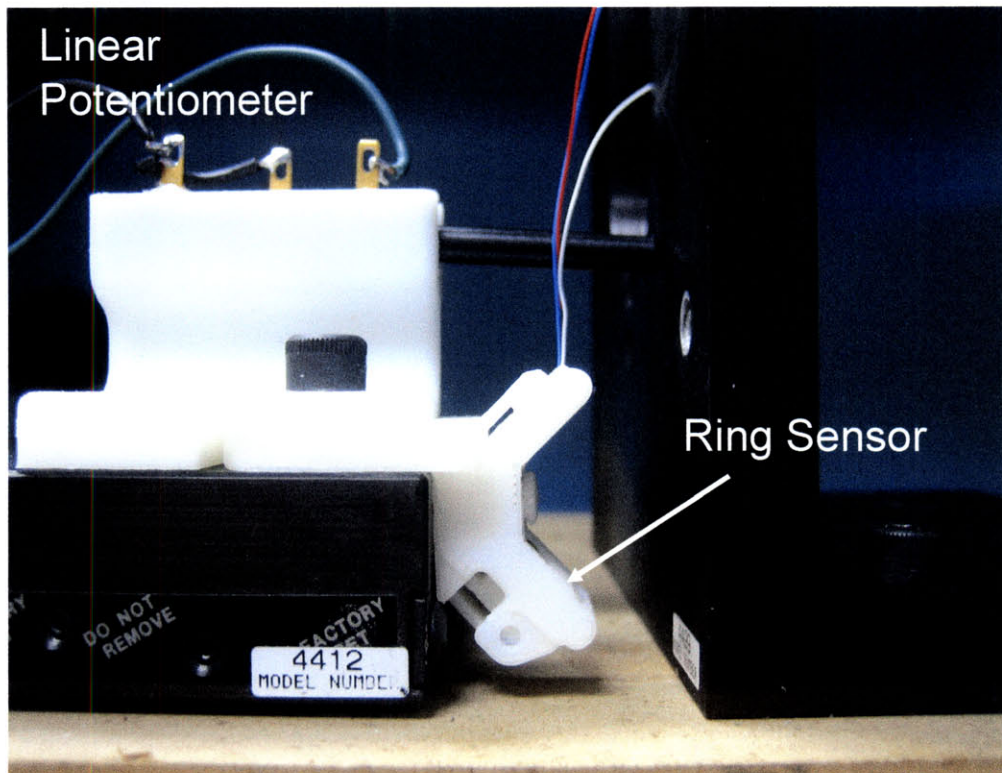


Figure 24: Picture of the finger base stiffness measurement system.

A pressure sensor (Entran EPL-D02-10P/Z1) in the ring sensor measured the resulting pressure while a standard linear potentiometer, calibrated by a simultaneously recorded micrometer (resolution = 0.025 mm) measured the applied displacement. A plot of the measured surface pressure versus the applied displacement is provided in Figure 25.

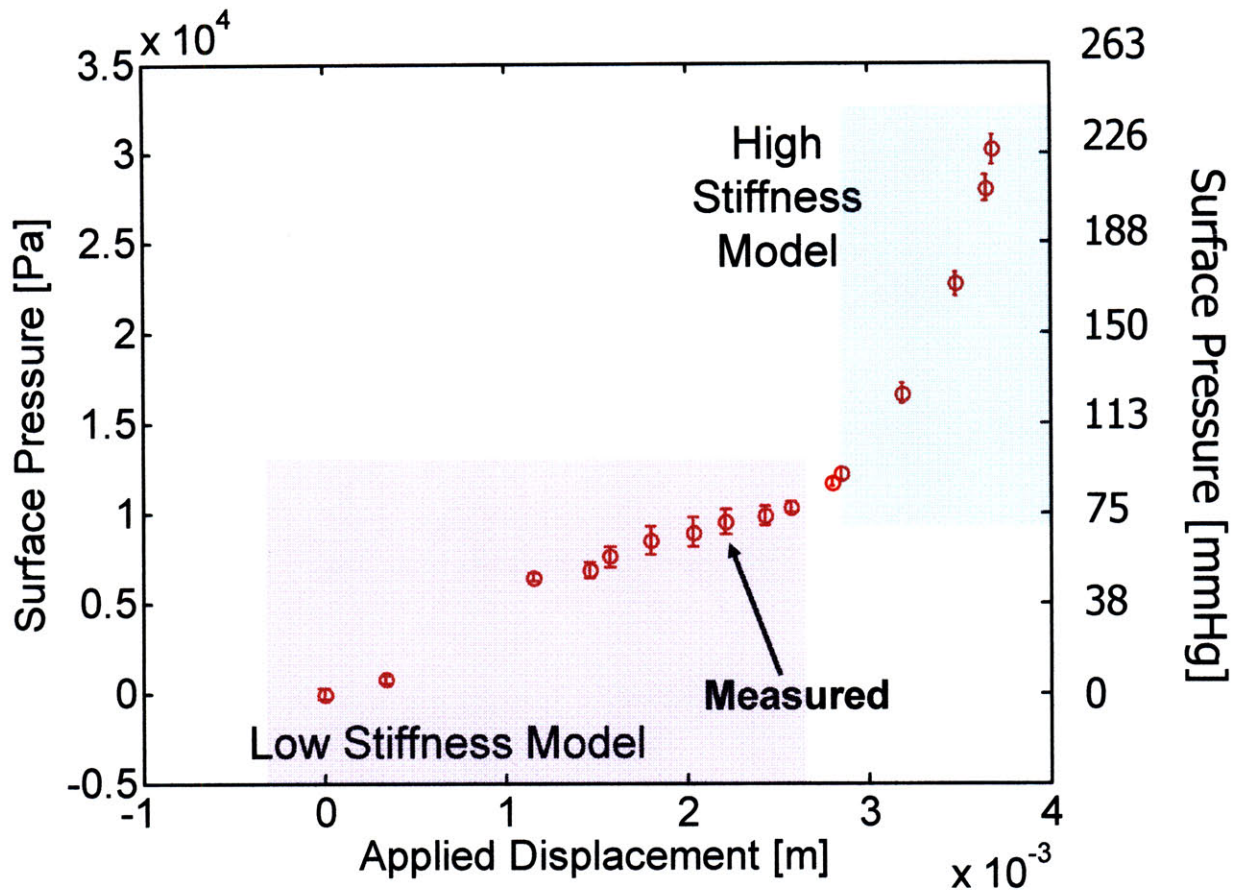


Figure 25: Human finger base compliance testing results compared to FE simulations.

The non-linear nature of the tissue within the fingerbase is clearly illustrated by the experimental results. However, it is interesting to note that there are essentially two stiffness modes exhibited by the fingerbase, a low stiffness region for surface pressures below about 12 kPa (90 mmHg) and a high stiffness region for pressures above the 12 kPa value. Since we generally plan to utilize the ring sensor at pressure below the mean arterial pressure (12 kPa) several of the questions described above can be answered with the previously described model. However, for large deformations, particularly those associated with directly simulating oscillometry, it will be necessary to augment the existing model using a piece-wise linear approach. The implementation of this technique will be described in more detail in section 4.3.5.

Initial focus was placed on the low stiffness model. The experimentally measured finger tissue stiffness for the low stiffness region was comparable to the surface pressures and corresponding applied displacements predicted by the finite element model (Figure 26). It appears that for relatively small displacements, displacements less than 3 mm, the assumption of a linear model with non-linear geometries is reasonable and capable of reliably estimating the pressures at the surface of the fingerbase. Since we typically expect the local surface pressure applied by the sensor to be less than the mean arterial pressure, these results indicate that the proposed model reliably captures pressures within the projected operating range of the sensor.

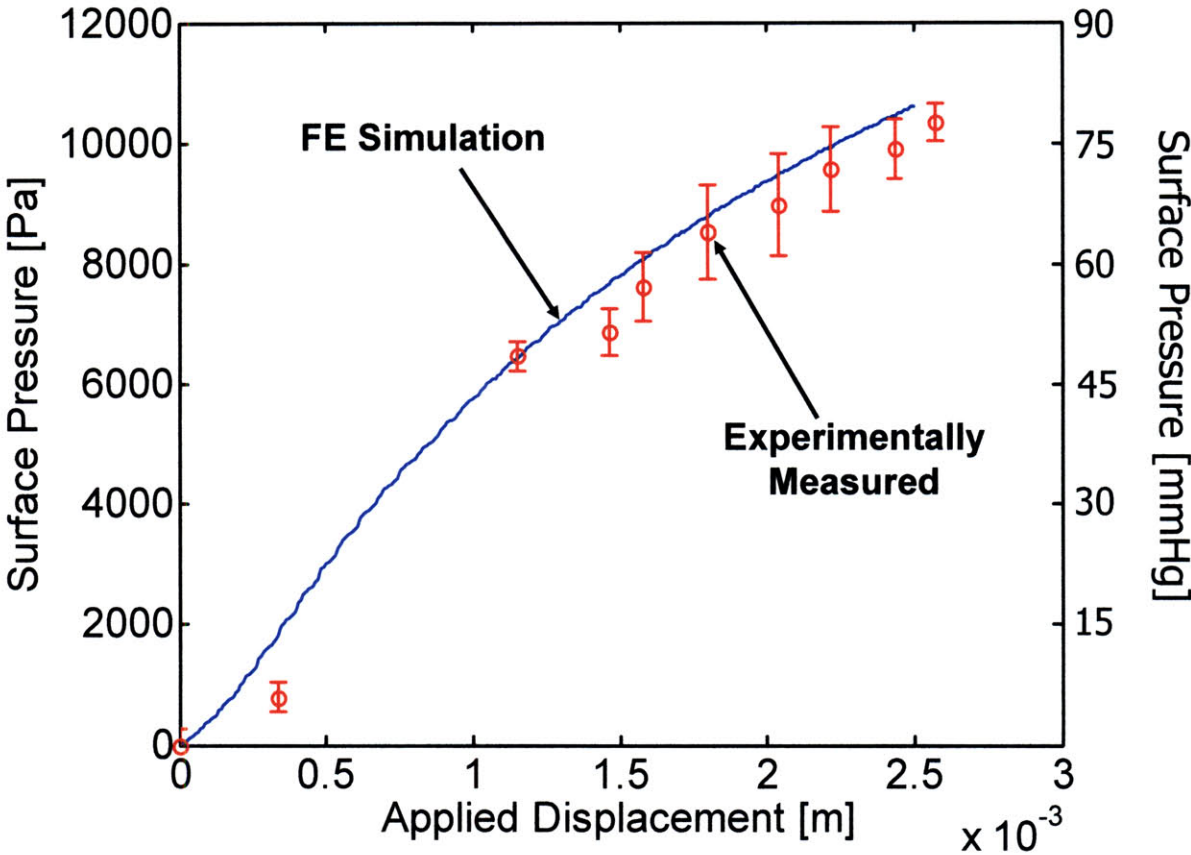


Figure 26: Comparison of the experimentally measured and FEA results for surface pressures resulting from a prescribed local displacement.

4.3 Finite Element Driven Ring Sensor Design Analysis

As stated previously, there are several objectives for our FE analysis towards verifying the sensor for long-term monitoring and gaining insight into the mechanisms controlling arterial wall deformations for focally applied pressures. In particular, we would like to verify that there is no significant interference with blood flow away from our sensor; ensure that the sensor is insensitive to device misalignments; evaluate alternative sensor designs towards a more accurate blood pressure measurement. Additionally, we would like to understand how surface pressures are propagated to the arterial wall.

4.3.1 Blood Flow Interference Prevention

An important design requirement for the ring sensor has been the minimization of the pressures away from the ring device. The advantage of a locally applied pressure is that, unlike a circumferential cuff, global blood flow is not restricted. As can be seen in Figure 27, pressures within the soft tissue away from the locally applied pressure are quite low.

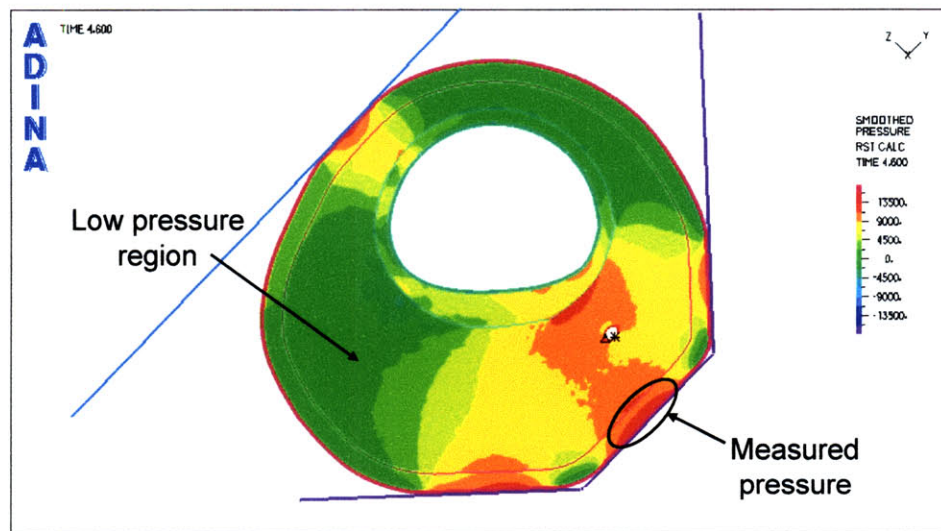


Figure 27: Nominal pressure distribution within the finger resulting from the focally applied pressure.

In fact, our simulation results indicate that the pressures away from the ring sensor do not exceed 1 kPa for up to 2.5 mm of applied sensor displacement. These results are encouraging in that these pressures are below even venous collapse pressures and should therefore enable a stable region for normal blood flow.

4.3.2 Sensor Misalignment

Since the ring sensor blood pressure monitor is intended to be worn by untrained patients away from doctor supervision, it is imperative that the device is robust against the possibility of misalignment. An example illustrating the results of a severe misalignment is provided in Figure 28. For this scenario it appears that the arterial wall is still affected by the applied surface pressure. The large contact area of the ring appears to provide a large region of relatively uniform pressure in the vicinity of the artery. These results indicate that for even severe misalignments, ring orientations exceeding reasonable placement ranges, the measurements made by the pressure sensor should be reliable for the proposed oscillometric technique.

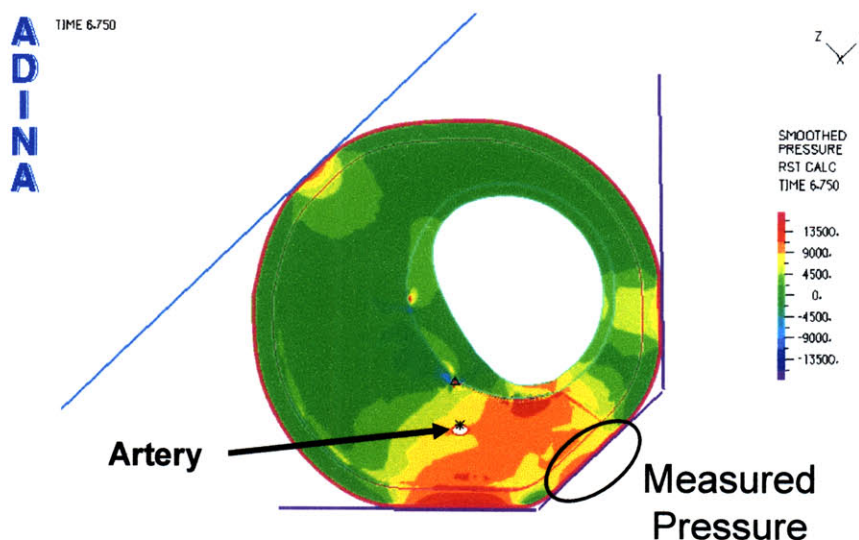


Figure 28: Pressure distribution within the finger resulting from a severe rotation of the finger relative to the position of the blood pressure sensor.

4.3.3 Ring Sensor Contact Geometries

Several different ring sensor contact geometries were implemented to examine the influence of the contact surface on the pressure propagation to the arterial wall (Figure 29, Figure 30).

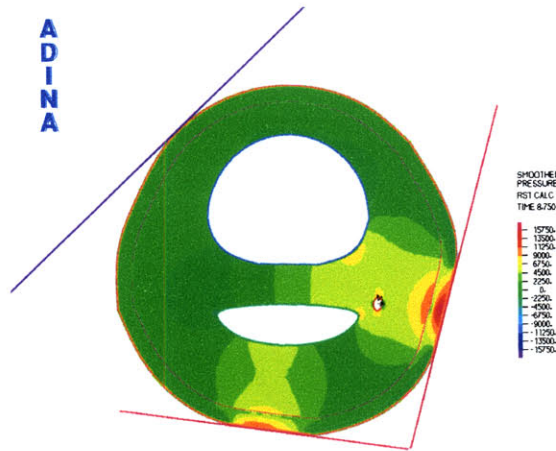


Figure 29: Simple L-shaped contact surface.

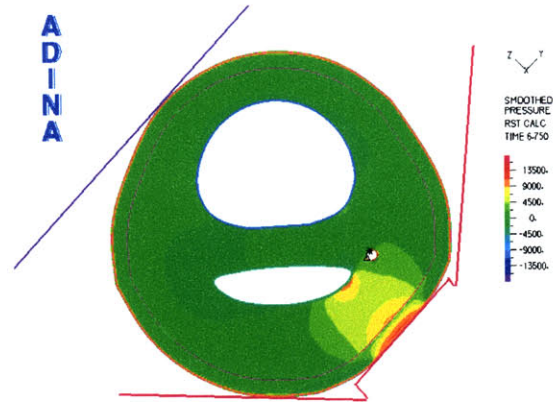


Figure 30: Representation of the existing ring sensor contact surface with larger local protrusion.

In general, we found that as length of the contact surface was increased up to about 45% of the entire circumference of the finger the match between the measured surface pressure and the pressure applied to the arterial wall improved. Protrusions smaller than about 10% of the circumference generally lead to pressure concentrations at the surface of the skin which did not correspond to uniform internal pressures (Figure 30). Additionally, the locations of the contacting surfaces relative to the artery are important. Figure 29 illustrates the effects resulting from an L-shaped contact surface. In this particular design, regions of the finger are unnecessarily pressurized.

4.3.4 Influence of the Tendon on Pressure Propagation

Figure 31 provides the results of our FE analysis of the pressure distribution within the finger resulting from a prescribed 2.5 mm displacement of the ring. For clarity, the direction of displacement is illustrated by the block arrow.

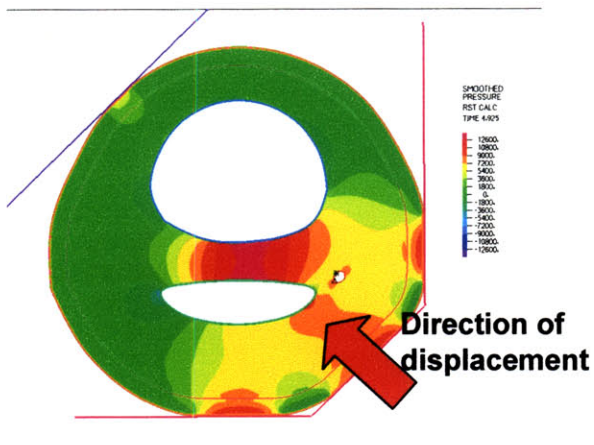


Figure 31: Pressure distribution within the finger base resulting from a 1 mm prescribed displacement of the ring sensor unit.

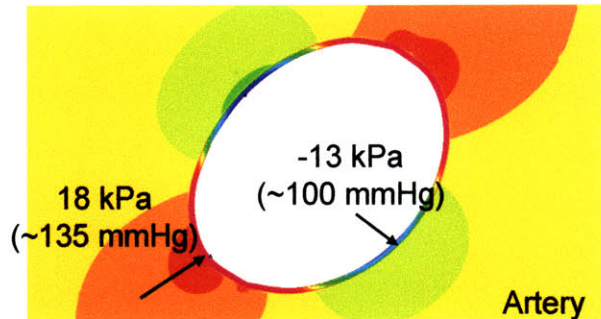


Figure 32: Close-up view of the of the pressure acting around the circumference of the arterial wall. Note the large range of applied pressures.

The results of this analysis indicate that if the tendon is decoupled from the bone, the pressure propagates from the surface of ring contact to the tendon and ultimately to the artery (for the given ring orientation). The measured surface pressure does not appear to change significantly and the region of pressure around the artery is relatively constant. Furthermore, the uneven pressures acting around the arterial wall potentially make it difficult to characterize the pressure within the wall. As can be seen from Figure 32, the pressures within the wall appear to promote wall collapse as they are significantly unbalanced orthogonally. However, since the balance of pressures acting around the arterial wall does not appear to be uniform, it is perhaps more appropriate to consider the net result of all of the different pressures operating across the wall as it is manifested in the alterations in the overall beat-to-beat amplitude changes of the

artery area. Specifically, for locally applied pressures, instead of a single uniform P_{out} , there is a range of pressures operating around the wall which lead to a net volume change. This result is explored in the following section.

4.3.5 Focally-applied Pressure Oscillometry

One of the critical questions initially proposed for the FE investigation was whether or not the pressure measured at the surface of the finger was equivalent to the external pressure acting at the arterial wall. The previous results have demonstrated that there is a clear disconnect between these pressures. However, given the results of our analysis indicating a non-uniform pressure around the artery, it is perhaps more appropriate to determine whether the measured surface pressure corresponds to the maximum pulsatile amplitude of the artery. To determine the answer to this question it is necessary to simulate an oscillometric measurement made by using the ring sensor.

In order to simulate oscillometry using the proposed ring design it is necessary to augment the existing model. The large experimentally demonstrated nonlinearity resulting from large deformations in Figure 25 can not be captured by our initial model. To this end, a scheme using a piece-wise linear approximation is applied to the model to enable simulations involving the required larger displacements (Figure 33). Specifically, the existing model is run to the maximum applied displacement allowed for the model. The deformations and loadings resulting from this deformation are recorded and used as the initial conditions for the second model.

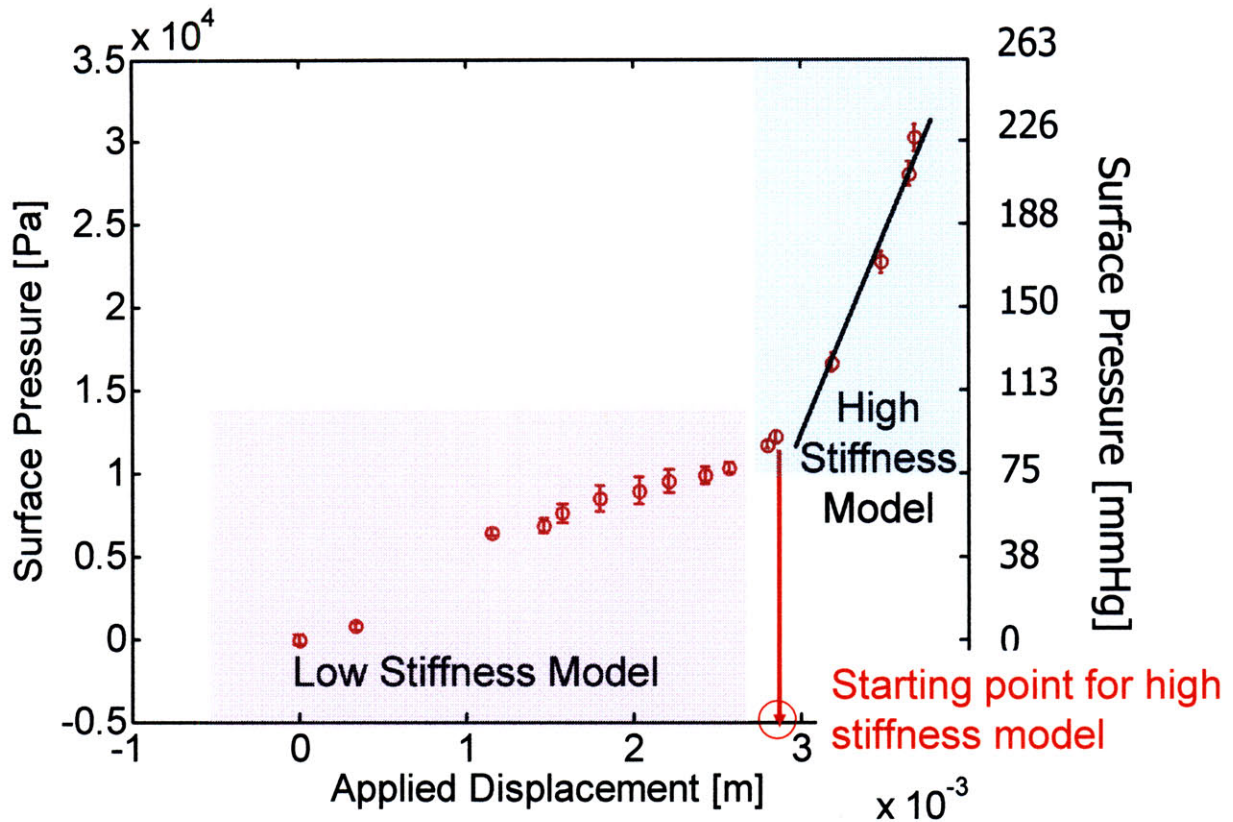


Figure 33: Illustration of piece-wise linear method used with experimentally measured tissue stiffness results.

The second high stiffness FE model, shown in Figure 34, incorporates the boundary conditions from the first model with the experimentally measured tissue compliance for large deformations. Although this model is simpler than our first model, it maintains the salient structures and geometries. The boundaries of the geometry have been selected to be sufficiently far enough away from the loaded artery such that errors in the boundary conditions should have minimal effects on the results of the artery pressurization.

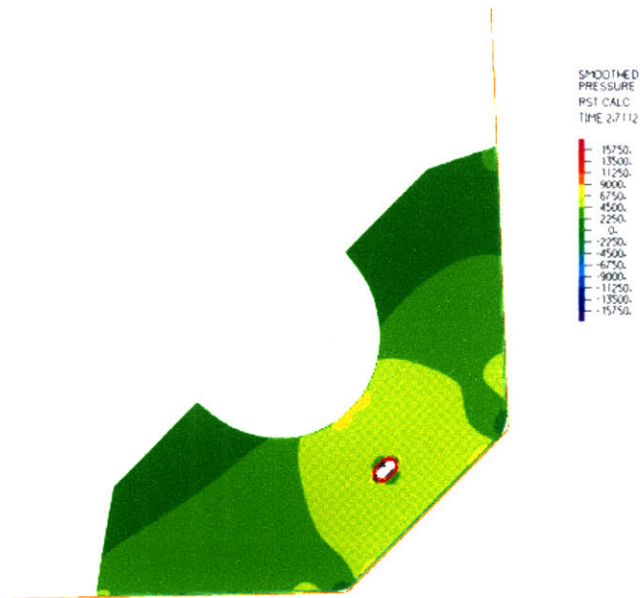


Figure 34: FE model implemented for directly simulating oscillometry.

The results of this analysis indicate that the focally-applied oscillometric measurement is capable of accurately capturing the mean arterial pressure (Figure 35). The predicted maximum pulsation amplitude appears to occur at a transmural pressure of 200 Pa (1.5 mmHg) which is quite reasonable for our oscillometric measurements.

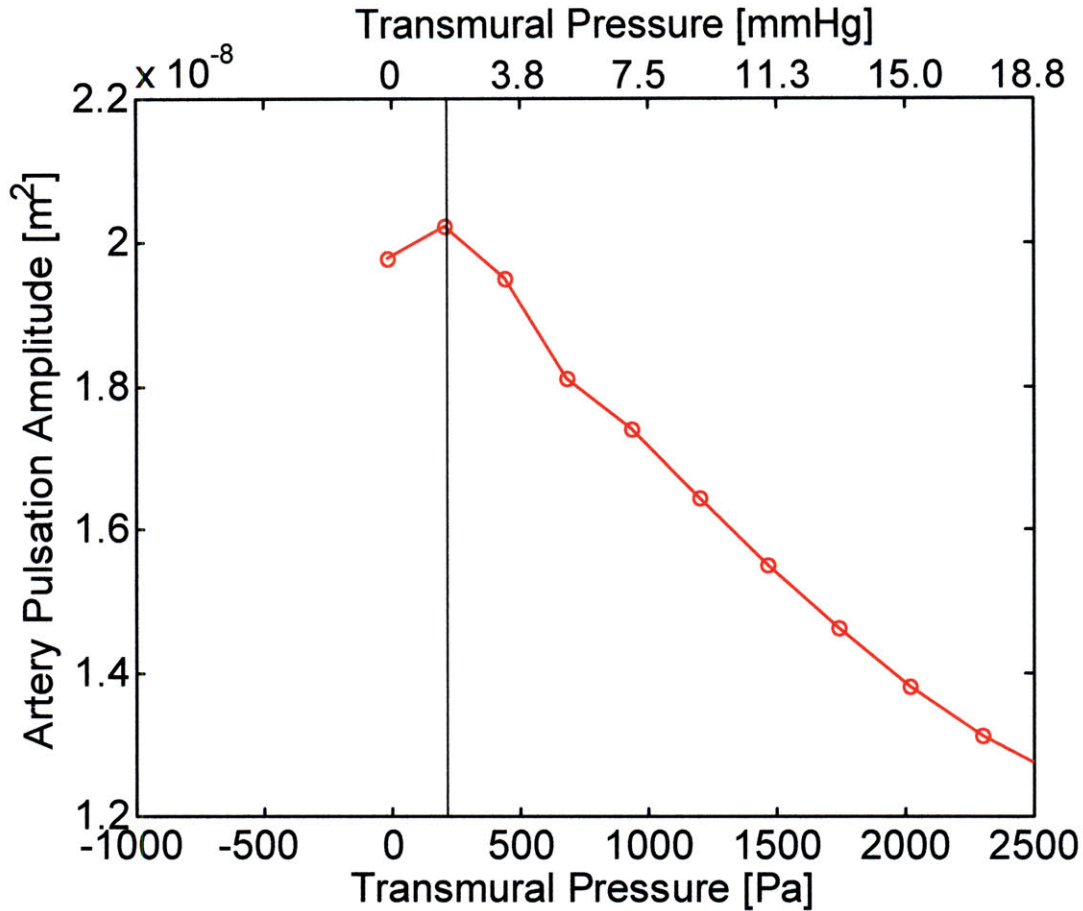


Figure 35: Comparison of artery pulsation amplitude vs. transmural pressure for locally applied loading conditions.

It appears that the pressure does not propagate directly from the ring sensor surface to the arterial wall. Instead, the model indicates that the artery is gradually squeezed between the bone and the focally applied load. Furthermore, it appears the method is reasonably insensitive to changes in the compliance of the surrounding tissue. See Figure 36. The FE results indicate that for a 20% change in the elastic modulus of the surrounding tissue only a 0.1 kPa (0.9 mmHg) change in the estimated MAP is expected.

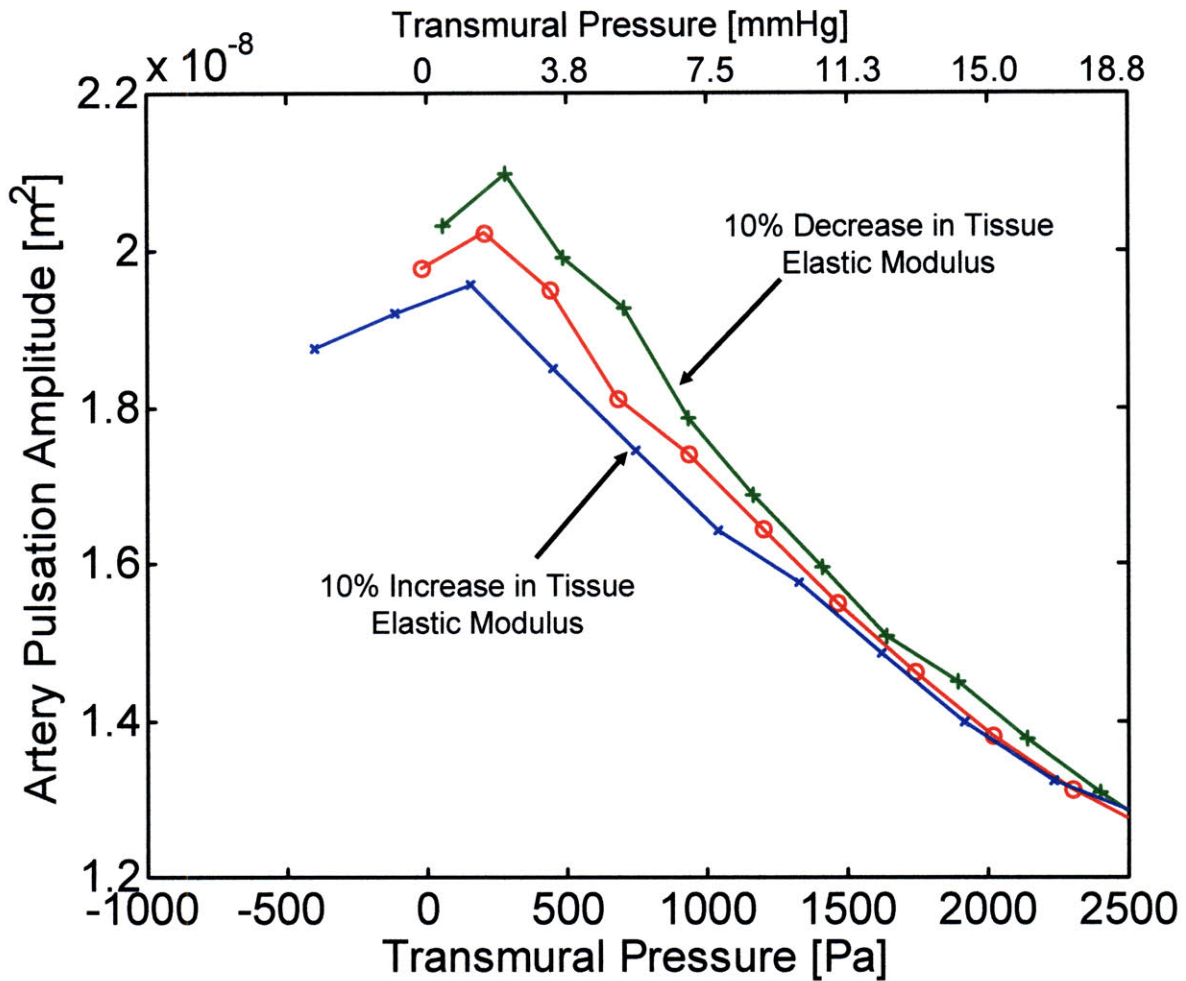


Figure 36: Comparison of the oscillometric results for a 20% change in the elastic modulus of the surrounding tissue.

4.3.6 Limitations of the Model: Circumferential Oscillometric Cuff Simulation

Using the proposed techniques, we attempted to additionally simulate a traditional oscillometric cuff to provide a reference point for the focally applied pressure analyses. Unfortunately, due to what appear to be numerical instabilities within the model, the modeling method was not capable of simulating this particular scenario. Figure 37 illustrates the results of

the circumferential simulation. Although a maximum pulsation amplitude was found, the sudden “jumps” in pulsation amplitude do not make sense physiologically and therefore require caution when interpreting the results.

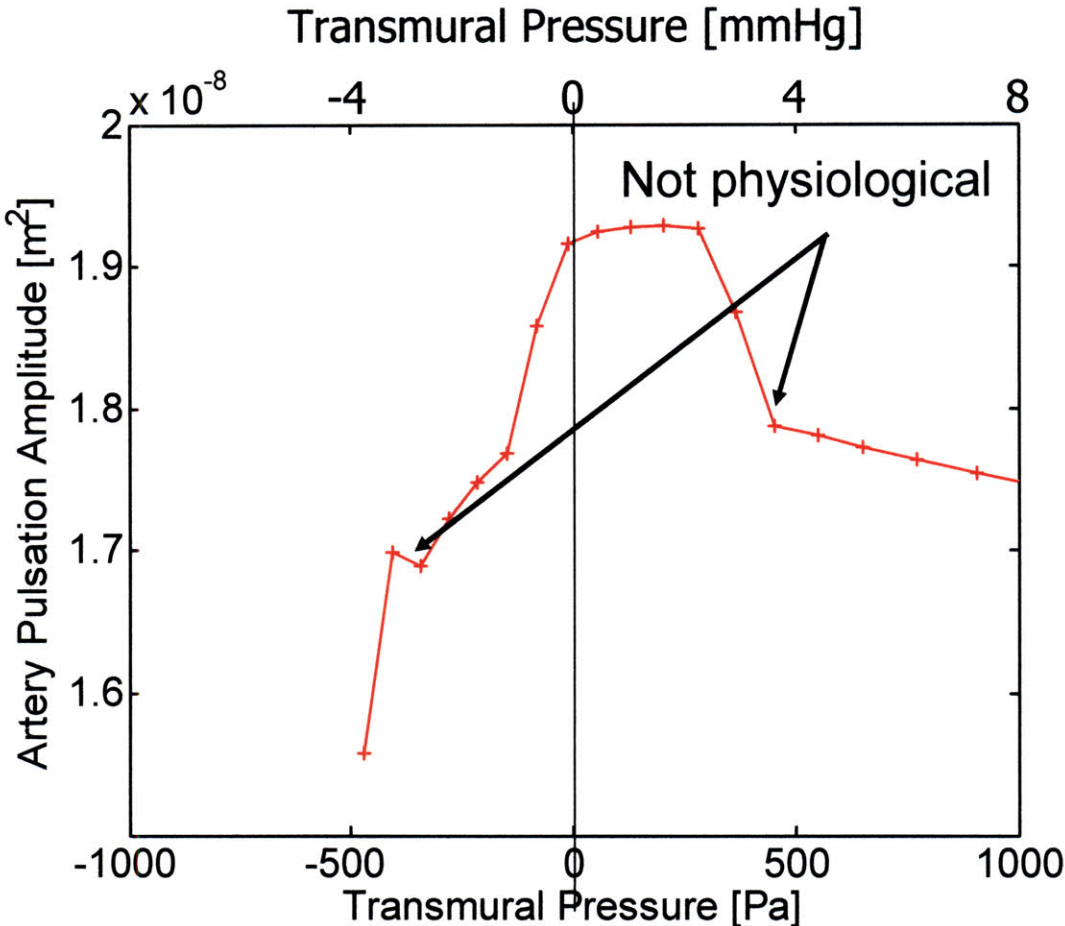


Figure 37: FE simulation of a circumferentially applied pressure illustrating the relatively uniform pressure distribution within the finger.

It is also important to reiterate that the model is not capable of capturing any of the fluid mechanics associated with pressurizing the arterial wall. Furthermore, since the model chosen is solid in nature the reader should be cautioned in the extracting the exact numbers yielded by the model for use in designs. A more complete model would include a combination of solid and fluidic components, perhaps in the form of a porous material choice. Based on the comparison

with direct surface pressure measurements, though, the model designed for small displacements is adequate for analyzing several aspects of the proposed ring sensor design.

4.4 Finite Element Modeling Results Summary

As was stated at the beginning of this analysis, answers to several questions related to long-term wearability and accurate blood pressure were investigated which could not be determined using experimental techniques. Through the course of the analysis we have found that,

- The local pressure design should not significantly interfere with blood flow away from the locally high pressures. In fact, the model indicates that the pressures away from the sensor are below venous collapse values.
- The ring design, although applying a local pressure, is robust to ring misalignments due to the large, relatively even contact region pressurizing the area near the location of the artery.
- The surface pressure is not exactly the same as the external pressure at the artery wall. Moreover, the pressure at the artery wall is not uniform, as is the case with circumferential pressures. However, the surface pressure does correspond to the set of pressures around the artery which yield the maximum pulsation amplitude. In particular, the model indicates an offset of around 200 Pa (1.5 mmHg) when using oscillometric techniques.
- The ring design is robust against changes in the tissue compliance, indicating that the design is capable of providing accurate blood pressure measurements for a variety of finger sizes and types.

Chapter 5 Sensor Design and Implementation

Figure 38 shows a prototype PPG ring sensor for measuring blood pressure at a digital artery based on the hydrostatic challenge protocol and FE analysis described above. The ring design represents a departure from the traditional inflatable cuff to a more wearable localized pressure design alternative. This design promotes long-term monitoring and is miniaturizable, while providing the necessary conditions for oscillometry. The device consists of a circuit unit, a sensor unit, and a Velcro band which wraps around the finger and holds the circuit unit and the sensor unit together. The sensor unit contains two LEDs, a photo detector array, a micro pressure sensor, and a MEMS accelerometer. Technical details of each component are described below.

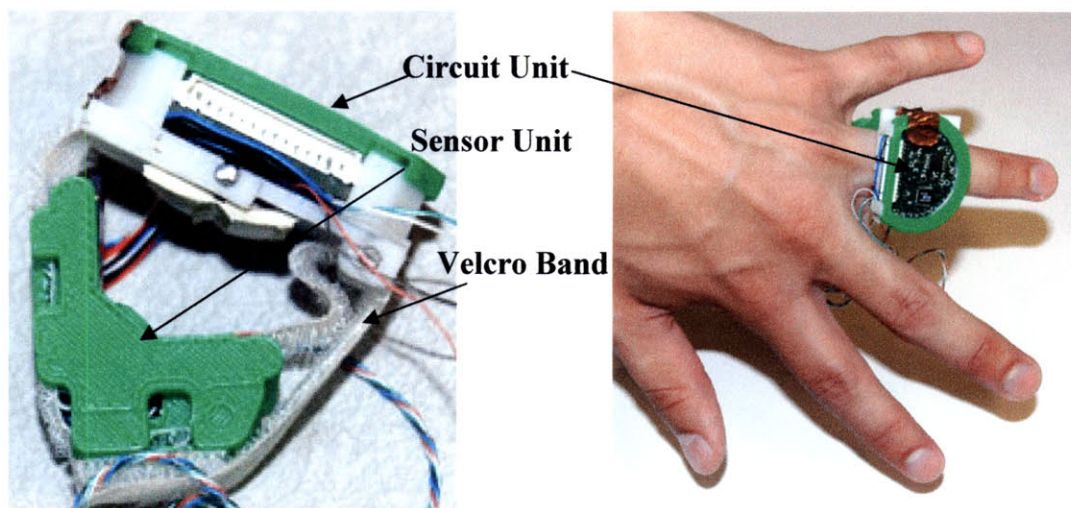


Figure 38: Prototype PPG ring sensor for MAP monitoring.

5.1 Mechanical Design

5.1.1 Optical Components

PPG waveforms are susceptible to disturbances, as mentioned previously. Care must be taken in attaching optical components to the skin so that the optical path may not be disturbed and that a high signal-to-noise (S/N) ratio may be obtained. Based on preliminary tests from 9 subjects (average finger circumference: 72 ± 4 mm), we have found that the optimal positioning of a PD and that of an LED are 85.3° and 15.1° , respectively, measured in a clockwise direction along the medial side of the finger. See Figure 39. This arrangement ensures that a digital artery is within the banana-shaped optical path [30], as illustrated in Figure 6a, and approximately agrees with our previous ring sensor design for measuring pulse and saturated oxygen level [69]. However, the shape of the structure holding the LED and the PD is substantially different from the previous design. We have also found through preliminary tests that the most stable PPG signal having a high S/N ratio is obtained when arranging the LED and PD in an L-shaped structure, as shown in Figure 39. Compared to the previous circular arrangement this rectangular configuration provides a stable light path from the LED to the PD by capturing the digital artery securely within the bend of the L-shaped structure.

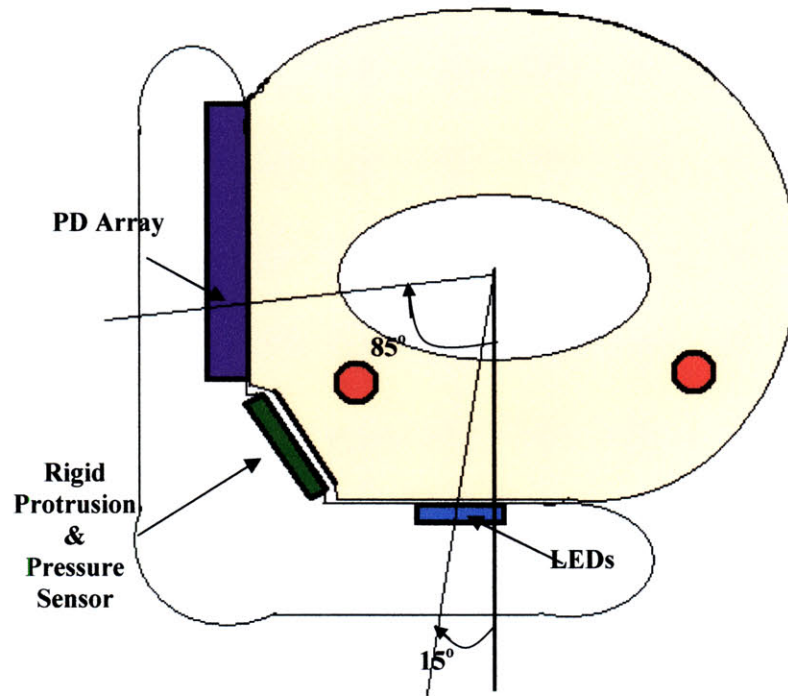


Figure 39: Illustration of the finger base with sensor unit.

The LED assembly (Elekon ELM-3003) consists of two independently controlled LEDs with wavelengths of 660 nm and 940 nm, respectively. The wavelengths provide maximal absorption of light by arterial blood. Additionally, these wavelengths are standard for pulse oximetry devices. The corresponding, spectrally matched 16-element photodetector array (Hamamatsu S8558) is positioned along the medial surface of the finger-base at an angle of approximately 90 degrees to the LEDs.

5.1.2 Applied Pressure Measurement Components

The proposed hydrostatic challenge protocol entails the measurement of pressure P_{cuff} in eq. (3). Conventional oscillometric NIBP sensors encircle an extremity with a cuff and apply a known pressure with an inflatable bladder. As shown in Figure 39, we apply a uniform pressure,

P_{ext} , to an underlying artery by way of a small rigid protrusion, pressing in a uni-axial direction. There are several advantages to this approach. Device miniaturization is possible since a bulky actuator is no longer required to inflate a circumferential cuff. Instead, a very small (6 mm diameter) DC motor is capable of controlling the applied pressure. More importantly, though, depressing directly over the artery minimizes the discomfort associated with total venous occlusion. Applying a high circumferential cuff pressure may incur interference with blood circulation. The proposed sensor design, however, overcomes this problem by applying a low pressure only to a small area near a digital artery such that P_{ext} replaces P_{cuff} in eq. (3).

See Figure 40. To measure the pressure, P_{ext} , a pressure sensor (Entran EPL-D02-/Z1) is sandwiched between a simple cantilever and a small, rigid protrusion. The diaphragm of the sensor is placed directly over the rigid protrusion and faces away from the surface of the finger. The back side of the pressure sensor is in contact with the rigid cantilever mechanism (maximum deflection = 0.5 mm) which protrudes from the surface of the ring and presses directly into the medial-palmar surface of the finger base.

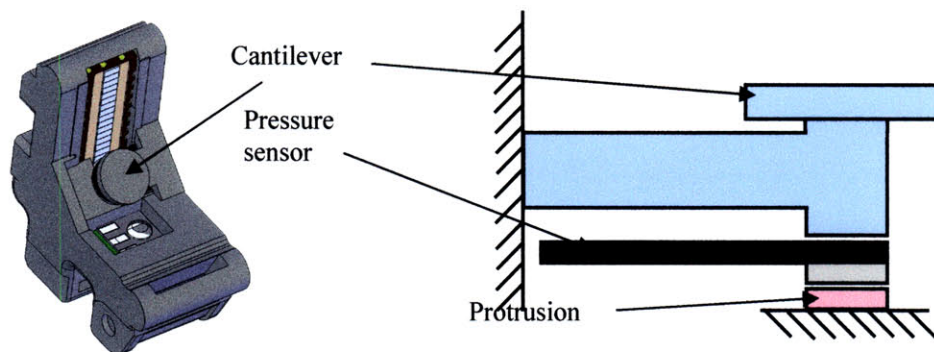


Figure 40: CAD drawing and illustration of the cantilever mechanism used to apply localized pressure.

The selected low-profile pressure sensing element consists of an encapsulated 68.8 kPa (517-mmHg) strain gauge unit attached to a stainless steel diaphragm. Measuring approximately 5 x 10 x 1 mm, the pressure sensor is carefully positioned between the PPG sensor elements at an angle of 45 degrees relative to the palmar side of the finger base. The pressure sensor utilized in the design represents a trade-off between a low-profile unit and a sensor design for solid mechanical contact. Since this particular sensor is designed for immersion in fluid environments, it was important to design the mechanical system such that it would not damage the sensitive diaphragm. Optimal measurements were found to occur only after the sensor was placed between two solid surfaces. Attaching the sensor unit directly to the skin surface tended to yield a significant underestimate of the actual pressure which was applied.

5.2 Motorized Sensor Units

5.2.1 DC Motor Driven

Through the course of our research we have noted that the pressure applied by the ring sensor generally changes with arm height. This result is most likely due to the changing amount of blood in the finger as the arm is raised and lowered. By actuating the pressure sensor it is possible to ensure that any changes in applied pressure are compensated. The motorized ring sensor has several advantages over previous models. In particular, the motorized pressure stage makes it possible to automatically set and regulate the pressure applied to the finger. Additionally, by controlling the applied pressure, hydrostatic calibrations should be significantly easier to perform. An illustration of the motorized ring sensor is provided in Figure 41.

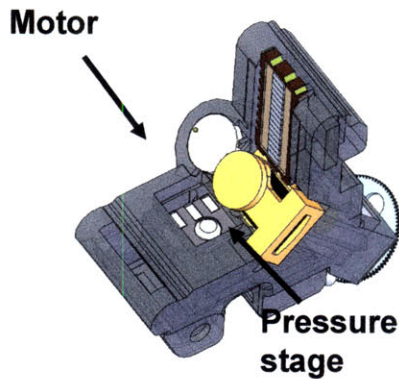


Figure 41: Motorized ring sensor design with movable pressure stage.

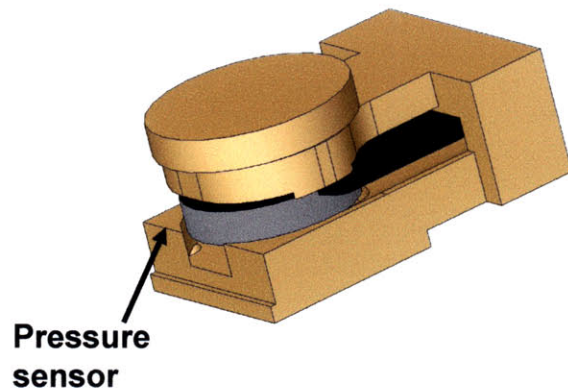


Figure 42: Close-up view of the actuated pressure stage with the pressure sensor.

The motorized ring sensor is actuated by a small, powerful DC gearhead motor (diameter = 6 mm, length with gearbox = 15.85 mm, $T_{\text{stall}} = 1.96 \text{ mN-m}$, $\omega = 1200 \text{ rpm}$) purchased from RobotMaker [70]. The selected motor provided the largest torque-to-size ratio of the commercially available DC-type motors. A list of alternative motor possibilities can be found below (Table 3).

TABLE 3: LIST OF SPECIFICATIONS FOR A FEW OF THE AVAILABLE MINIATURE DC MOTORS.

		T_{stall} [N-m]	d [mm]	L [mm]
RobotMaker	Nanogears	0.0019613	6	15.85
	Microgears	0.2451663	11	25
Smoovy	DC-Servo	0.00007	5	14
	Thin-Brushless	0.00005	12	1.83
BG Micro	Pager Motor		4.75	16
	Little Bitty	0.00026	12	15
RC Micro	1.6		5	12
Faulhaber	0620+64:1 gear	0.035	6	24

A simple 4:1 pinion-spur gear combination made by Didel [71] or a belt-drive power transmission system constructed in the lab have been utilized to increase the torque supplied by the motor (Figure 43).

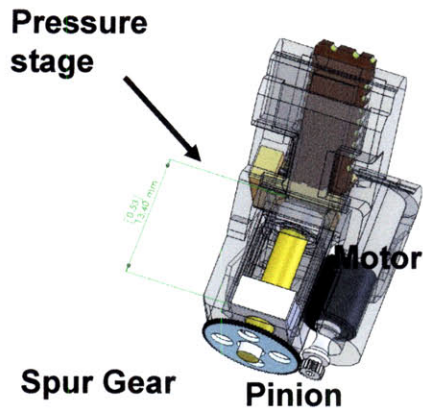


Figure 43: Isometric view of the lifting mechanism contained within the motorized ring sensor.

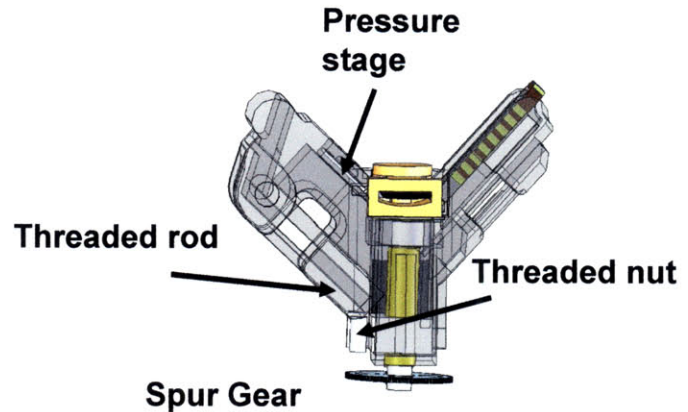


Figure 44: Side view of the motorized ring sensor illustrating the travel available to the threaded nut and pressure stage as the motor is activated.

The large spur gear is rigidly attached to a threaded rod. Riding along the length of the threaded rod is a matched nut attached directly to the pressure stage. The nut is prevented from rotating by sliding along a channel within the ring sensor. Preventing rotations changes the rotational motion of the motor and gear system into linear motion. The total allowed travel of the pressure stage and nut is 7 mm, which is sufficient to provide the desired loading pressure for all finger sizes (Figure 44). To calculate the torque required by the motorized sensor first note the maximum pressure we wish to apply to the finger surface.

For this work, a pressure of 13.3 kPa (100 mmHg) was selected on the assumption that the hydrostatic challenge will be able to provide the additional pressure necessary to exceed the patient's mean arterial blood pressure. The area of the contact surface of the sensor is provided by the dimensions of the small circular protrusion of the pressure stage. However, to add a small

safety factor to our calculations, we will assume that the entire rectangular pressure stage surface will be in contact with the finger, leading to a contact surface area of,

$$A = l * w = 5.4 \cdot 10^{-5} m^2 \quad (7)$$

Therefore, the force which must be supplied to achieve the desired pressure is found to be,

$$F = P * A = 0.72 N \quad (8)$$

where P is the design pressure previously noted and A is the contact surface area provided by eq. (7). We must next determine the amount of torque required by the motor to lift a nut loaded by the result given in eq. (8). This torque can be estimated by applying the following equation,

$$T = \left(\frac{F \cdot D_p}{2} \right) \left(\frac{\Lambda + \mu \pi D_p}{\pi D_p - \mu \Lambda} \right) \quad (9)$$

where F is the load given in eq. (8), D_p is the pitch diameter (0.004 m), Λ is the lead (0.008 m), and μ is the coefficient of friction (0.08). The resulting torque with the inclusion of a safety factor is found to be,

$$T = 2.6 \text{ mN-m} \quad (10)$$

Therefore, additional gearing was required to ensure that the torque supplied by our motor is sufficient to achieve the desired applied pressure.

5.2.2 Piezo-based Linear Actuator

Further device miniaturization can be achieved by utilizing commercially available piezo-based linear actuators [72]. The “Squiggle” actuator provides up to 15 mm of linear travel at up to 8 mm/s (Figure 45 a). The reported stall force of the motor is 1.5 N which is sufficient to support our loading specifications. Since the maximum diameter of the actuator is less than 2.4

mm, the entire assembly easily fits into the ring body without significantly increasing the size of the unit (Figure 46).

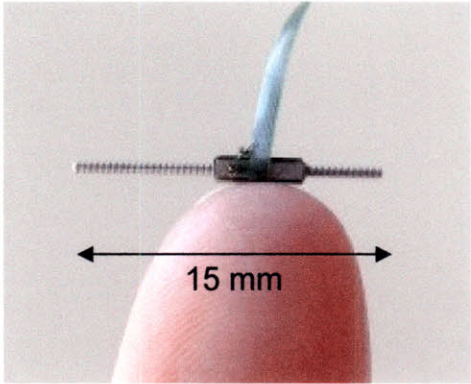


Figure 45: (a.) Squiggle series linear actuator; (b.) Ring Sensor using miniature piezo actuator.

The main trade-off in selecting a piezo-based actuator is the large DC-DC power conversion that is required to provide the 100V actuator supply voltage. Currently, a separate power conversion and controlling board is required to actuate the motor. In the future these limitations may be removed as the boards are migrated to a smaller form factor.

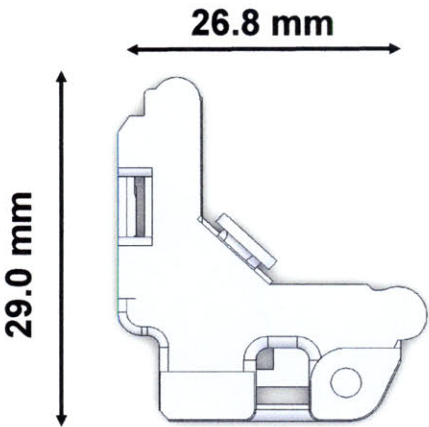


Figure 46: Initial BP prototype with dimensions. The additional analog and digital conditioning circuitry are not pictured.

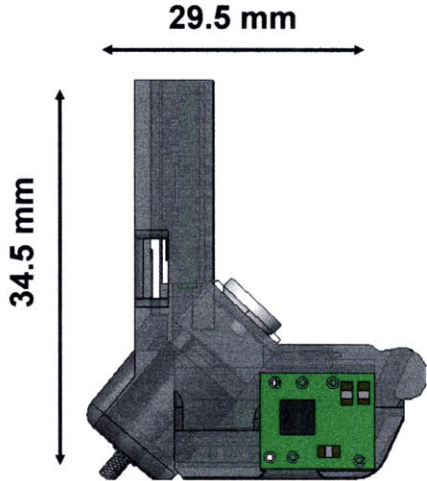


Figure 47: Actuated BP prototype with all required conditioning circuitry.

5.3 Height Sensor

5.3.1 Theory and Implementation

Any oscillometric MAP measurement, include the proposed method based on the hydrostatic challenge protocol, requires a sensor that can measure the height of the blood pressure sensor relative to the heart. To make the system truly wearable, the height sensor must be compact and lightweight, comfortable to wear, and non-interfering with daily activities. Existing height measurement options, which include water filled manometers [73] and video motion tracking, are not ideal for remote patient monitoring.

In this thesis a new method for estimating the height of the hand using two small, wearable accelerometers is developed. The first accelerometer is placed on the upper arm, with its axis aligned along the longitudinal direction of the humerus. When the upper arm is straight down, the accelerometer axis is aligned with gravity, and its output is approximately 1 G. As the accelerometer is tilted together with the upper arm its output decreases accordingly. This indicates the orientation of the humerus relative to gravity, as denoted θ_1 in Figure 48. The second accelerometer placed within the ring itself reports the approximate orientation of the radius/ulna, θ_2 .

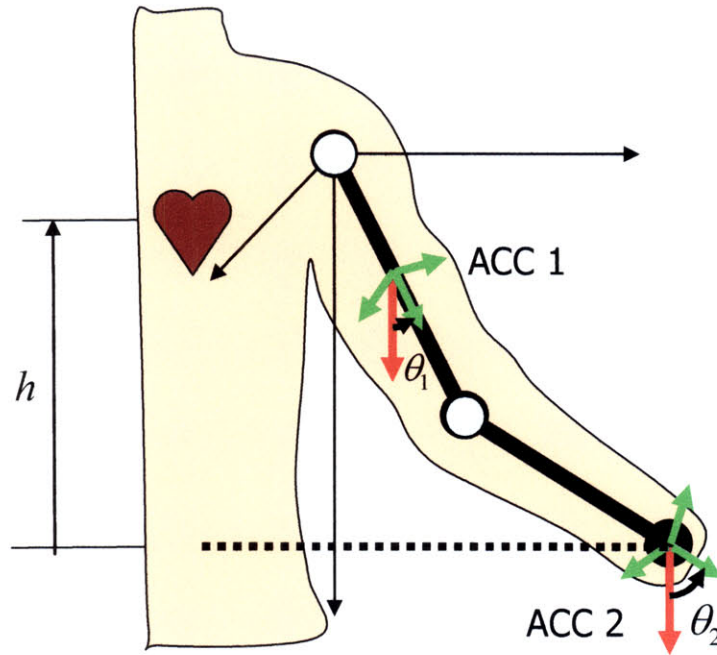


Figure 48: Illustration of the proposed height sensor using two MEMS accelerometers.

Using basic geometry and a model of the upper extremity as a two-link kinematic chain, it is possible to estimate the height, h , of the hand relative to the shoulder (Figure 49).

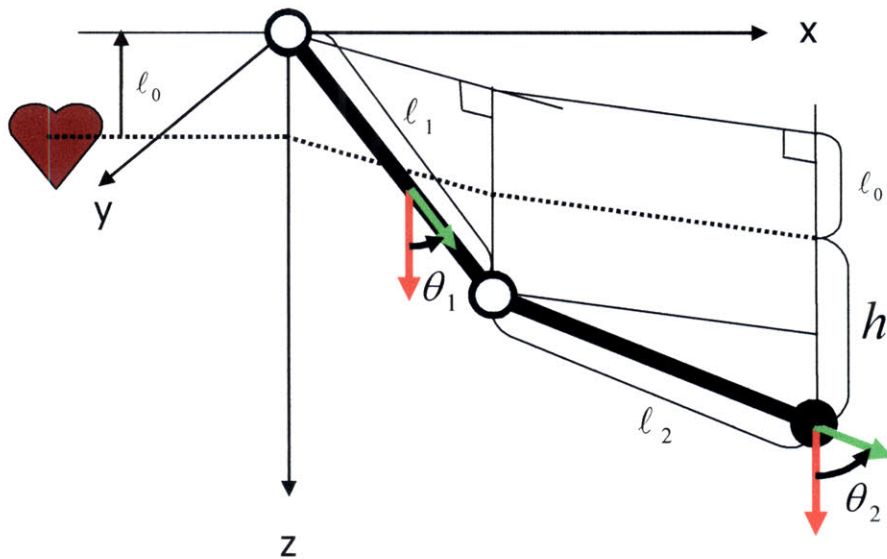


Figure 49: Definition of height measurement terms.

Let ℓ_1 and ℓ_2 be the lengths of the upper arm and the forearm, respectively, and ℓ_0 be the height of the shoulder joint relative to the heart (Figure 48). From the figure the height of the heart relative to the PPG sensor is given by

$$h = \ell_1 \cdot \cos\theta_1 + \ell_2 \cdot \cos\theta_2 - \ell_0 \quad (11)$$

The approximate values of link lengths ℓ_1 , ℓ_2 , and ℓ_0 can be estimated from the height of the wearer or by measuring the length of the arm itself. Three-axis micro accelerometers using the micro-electro-mechanical-systems (MEMS) technology are smaller than the size of a dime, even when including all electronics and power sources. They can be imbedded into the PPG sensor as well as attached separately to the upper arm.

5.3.2 Height Sensor Considerations

Vertical offset between the measurement location and the proximal aorta are a major potential source of measurement error. Conventionally, this is solved by training the users. The Portapres, which monitors continuous arterial blood pressure, uses a fluid-filled column attached to the upper extremity to monitor the height of the sensor. In this work, we offer a novel solution to height sensing which only requires a second, small sensor worn on the proximal arm. The current embodiment of the height sensor consists of two three-axis MEMS type accelerometers (Analog Devices, ADXL330).

An important consideration associated with the height sensor is that the performance of the height sensor is limited to low acceleration monitoring conditions. Large accelerations, accelerations several times larger than gravity, would easily overwhelm the measured gravity influence and consequently limit the accuracy of any corresponding height change measurements. For this reason, we recommend that hydrostatic challenges be performed

following the time interval guidelines described in Chapter 6, so that the height is measured when the arm is at rest.

5.4 Electronic Component Design

The finger ring blood pressure sensor consists of a completely self-contained signal control and conditioning system. The individual components have been designed modularly for easy export to other embodiments of the sensor. The required components consist of the photodetector array, the LED, the pressure sensor, the motor driver, and the accelerometer. The control and conditioning circuitry for each of these elements will be detailed in the following sections.

5.4.1 Photodetector Array

As was previously mentioned, a 16-element photodetector array is used for detecting the amplitude changes of an underlying artery. A typical unaltered PPG waveform is manifested as a very small change in current (on the order of a few microamps) at the output of most photodetectors. It is therefore necessary, whenever working with PPG-based sensors, to include a few essential elements into the system design. First, because of the extremely small amplitude of the signal, any wiring connections between the optics and the conditioning circuitry should be as short as possible and include shielding whenever possible to prevent environment noise corruption. It is generally important to immediately convert the incoming current-based signal into a voltage before data acquisition. Converting current to voltage is typically accomplished with a transimpedance amplifier which can be purchased either preassembled or constructed from an op-amp with a feed-back resistor. See Figure 50.

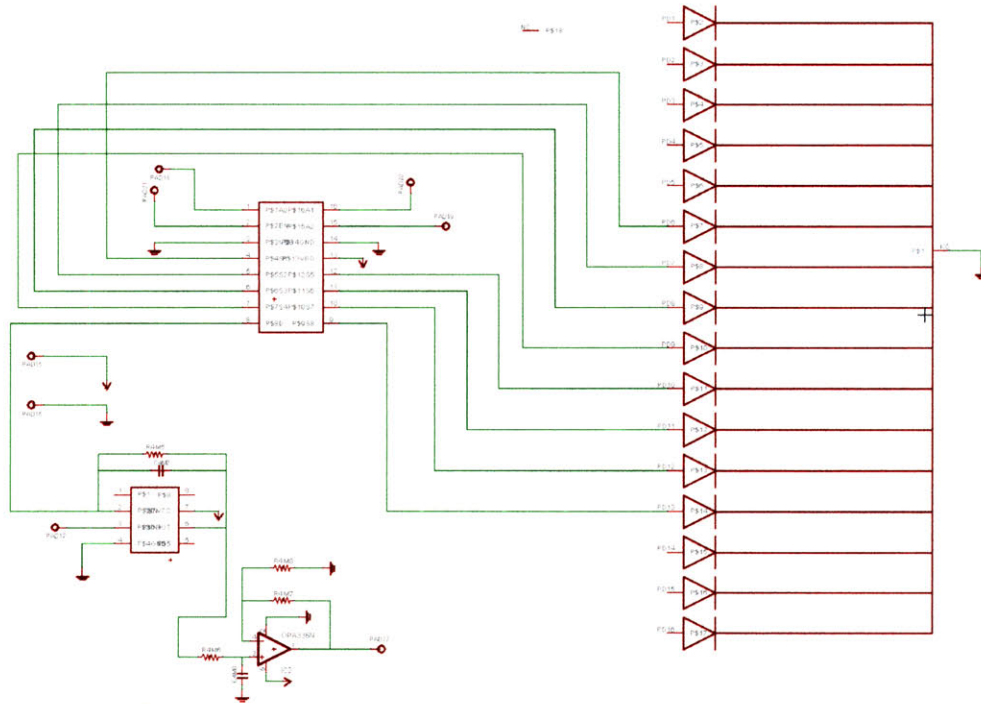


Figure 50: Schematic of multi-plexed PD array circuit.

To minimize the connection length between the photodetector array and the conditioning elements, a small modular circuit board was designed (Figure 51). Eight of the outputs of the photo detector array, which are linear with current, are connected to a multiplexer which allows for selection of a single, optimal channel. The selected photodetector channel is next sent through a low-noise, high-bandwidth transimpedance amplifier with adjustable gain to convert the current to a voltage stage before continuing through a band-limiting stage with amplification (1st order low-pass Butterworth filter, $F_c = 30$ Hz, Gain = 200). Band-limiting the signal is necessary to prevent Nyquist related aliasing from occurring when the signal is sampled.

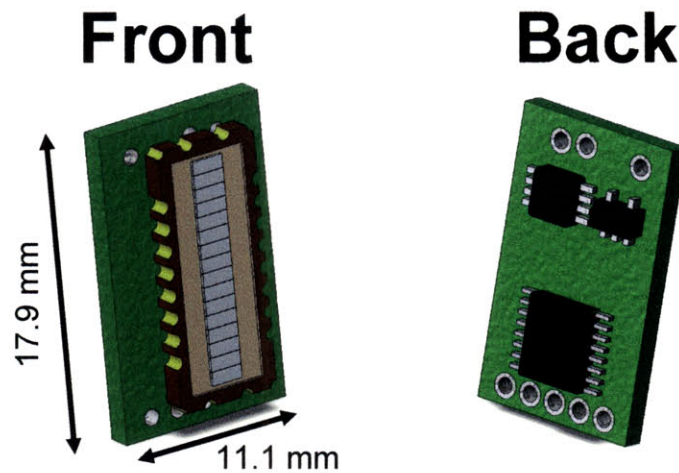


Figure 51: CAD illustration of assembled PD array circuit.

5.4.2 LED Control

The intensity of the LED component of the PPG requires a simple transistor-based current control circuit (Figure 52). In general, if a microprocessor is used to control the state of the LED, it is necessary to buffer the control signal by adding an op-amp follower to the base of the transistor. In this implementation, the current can be adjusted manually by changing the resistance value of the potentiometer. The typical operating current for the LED is 15 mA. The current supplied to the LED can be manually adjusted by changing the resistance at the emitter of the transistor by way of a potentiometer.

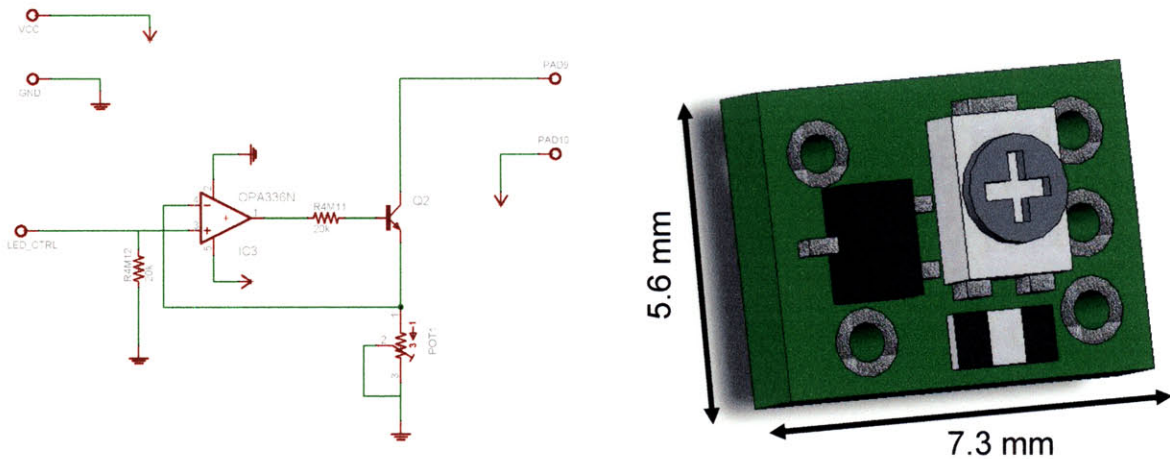


Figure 52: Schematic and accompanying CAD illustration of the LED control circuitry.

5.4.3 Pressure Sensor Conditioning

The low-profile pressure sensor previously described is designed to operate with a 10 V excitation voltage. The excitation voltage may be lowered, however, at the expense of sacrificing output resolution. In this design an excitation voltage of 5 V was found to be sufficient for blood pressure monitoring with the given list of circuit components. To condition the output of the sensor the signal is amplified and conditioned with a precision instrumentation amplifier (Texas Instruments INA326E) and 1st order Butterworth low-pass filter ($F_c = 1$ Hz). The instrumentation amplifier is necessary to remove common-mode noise from the differential outputs of the sensor as well as to amplify the signal of interest. After conditioning, it is possible to achieve a nearly 1 volt swing in output over the operating pressure range (Figure 53).

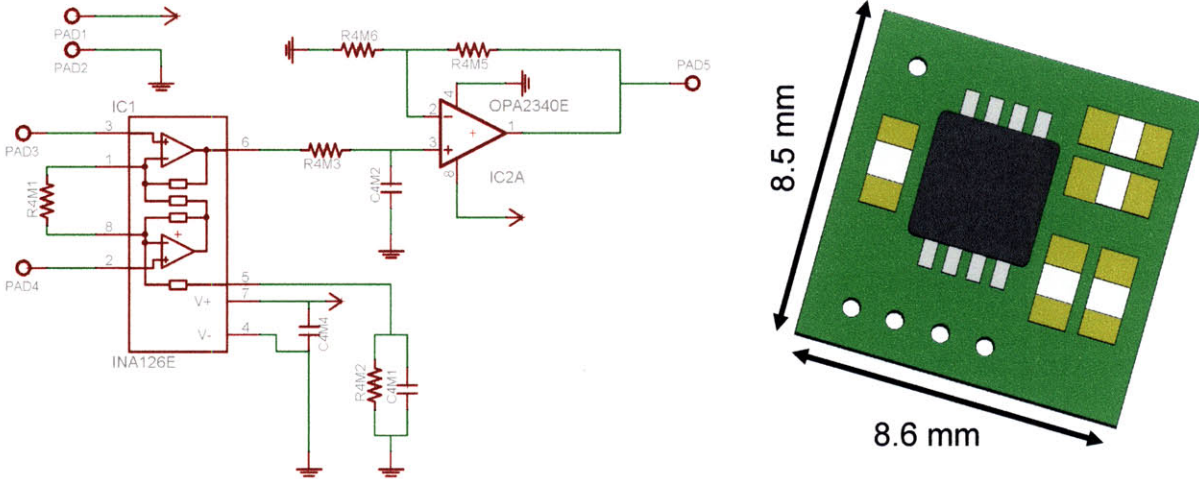


Figure 53: Schematic and CAD illustration of the circuit used to condition the output signal of the pressure sensor.

5.4.4 Accelerometer Conditioning

The low-profile accelerometer is based on the 3-axis ADXL330 chip. A capacitor is placed between the input voltage and ground to remove noise from the excitation voltage as recommended by the manufacturer. The band-width of each of the outputs is set by adding a capacitor tied to ground. The cut-off frequency for the height sensor was set to $F_c = 1\text{Hz}$.

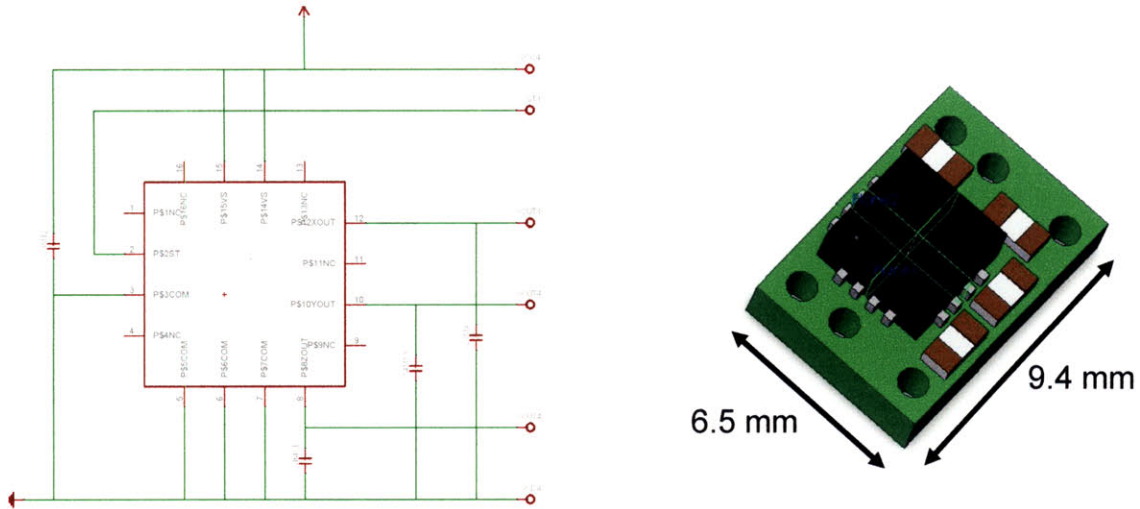


Figure 54: 3-axis accelerometer schematic and CAD illustration.

5.4.5 Motor Driver

A low power (3V, 400mA), low profile motor driver made by Allegro is used to control the current supplied to the DC motor (Figure 55). The motor driver circuit consists of a dual H-bridge with two pull-up resistors at the control input to ensure that unless the motor is commanded to be on it will not spin as there is no voltage difference between the channels. The small signal Schottky diodes at the driver output protect the driver chip from back emf voltages associated with the motor.

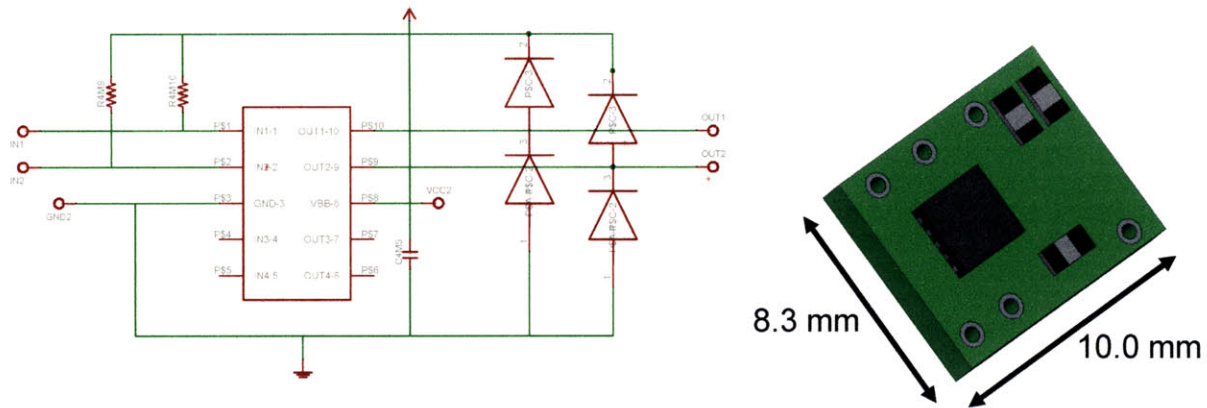


Figure 55: Low power DC motor driver schematic and CAD model.

5.5 Sensor Registration and Signal Processing

A few more technical issues must be addressed in order to make this protocol feasible and reliable for MAP measurement. First, a stable PPG signal providing consistent amplitude measures must be obtained. The PPG sensor must be attached correctly to a palpable artery, and the cuff pressure must be applied in such a way that it may not interfere with blood perfusion for extended periods of time. The zero-transmural point must be detected accurately despite spontaneous movements of the patient. The following section addresses these technical details.

PPG waveforms are sensitive to misalignment as well as to disturbances. Signals often corrupt if not properly positioned at the finger base. One of the difficulties in using health monitoring sensors in the field is that the sensor may not be placed properly without close supervision by medical professionals. For the prototype PPG ring sensor two techniques have been developed to cope with the sensor registration problem. One is to use a multitude of photo detectors arranged in an array, as shown in Figure 56.

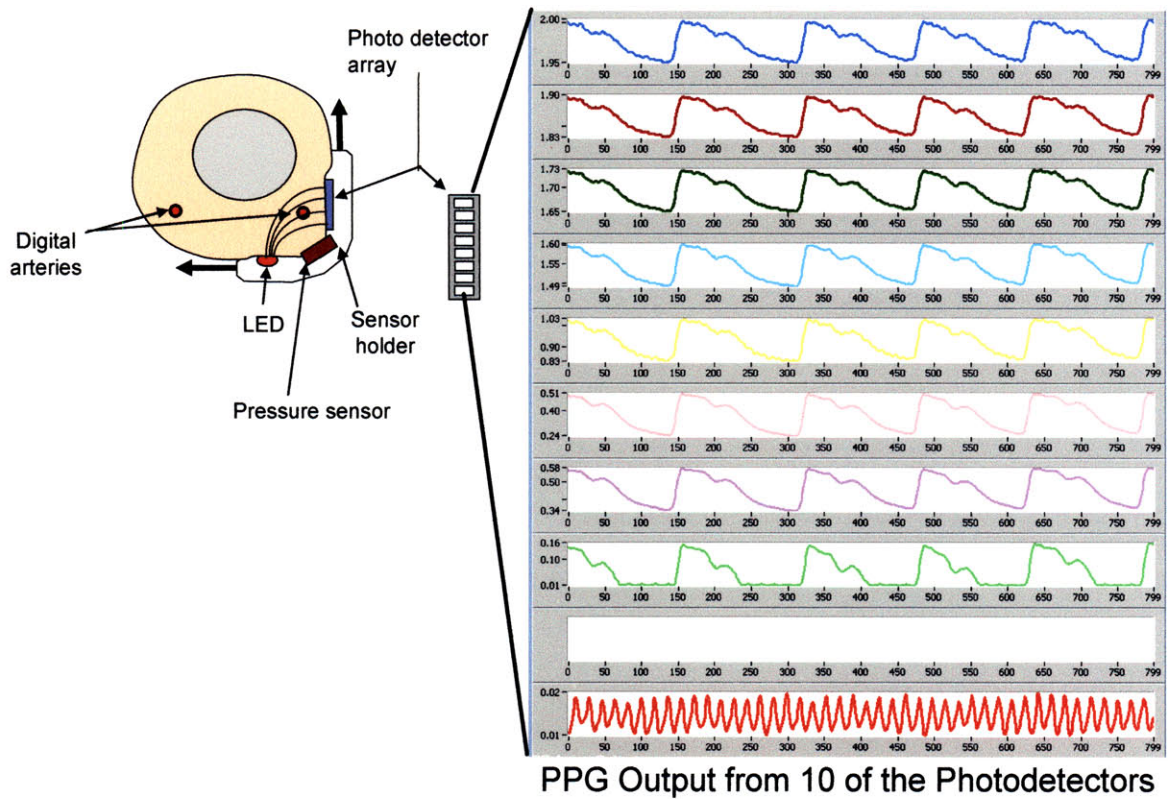


Figure 56: Simultaneous waveform outputs from multiple photodetector array elements.

Although the sensor unit is not accurately placed relative to the digital artery, 16 channels of the PD array can cover a wide area, so that a proper signal can be obtained from one of the PDs in the array (Figure 57). The other is a semi-automatic sensor registration algorithm.

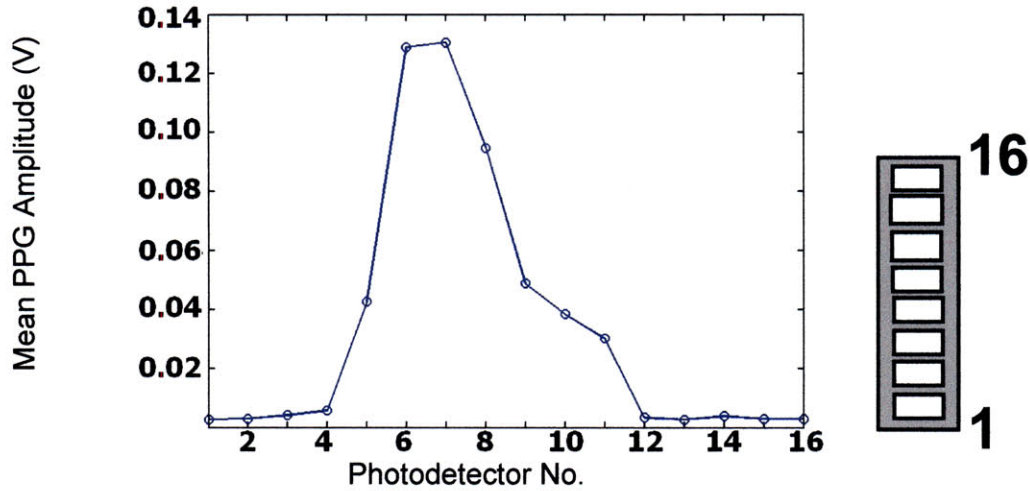


Figure 57: Plot of the mean PPG amplitudes vs. photodetector element which illustrates a properly registered sensor. The maximum amplitude signal is found to occur near the middle of the photodetector array.

Once the ring is initially positioned, i.e. the LED is centered under the palmar surface of the finger base and the PD array is pressed into the finger tissue, the system identifies the best channel among the 16 PDs in the array, together with the best combination of LED intensity. There is an intricate relationship among the length of the LED light path, the LED intensity, and the location of the PD. A search algorithm can find the optimal combination among them, once the sensor is attached to the finger. Furthermore, the system assists the patient in accommodating the external pressure, P_{ext} . The nominal pressure is set to 8.0 kPa (60 mmHg), which is compared with the actual pressure sensor measure, and if it is out of the range, a warning is given to the patient.

A two parameter registration algorithm, consisting of the LED intensity, I , and the PD array element PD_i , is performed. First, the LED intensity is slowly increased from a low intensity (< 1mA) to a relatively high intensity (15 mA). Simultaneously, the photo detector outputs are scanned to determine which elements of the array contain the pulsatile signal. Figure 57 shows

the distribution of the signal strength among the 16 channels of PD array. Once the intensity range has been scanned, the LED intensity is set so that two criteria are optimized as follows: the photo detectors in the center of the array contain the maximum amplitude pulsatile waveform; the maximum amplitude is above a pre-defined threshold (typically 100 mV peak-to-peak in this work).

PPG signals often corrupt when the sensor is misaligned. The new sensor design based on a local, low pressure arrangement does lead to a new difficulty: improper positioning of the probe (relative to the underlying artery) will likely lead to measurement errors. As mentioned before, one of the major difficulties of wearable health monitoring for home and field use is proper positioning of the sensor for optimal measurements, because users may not be professionals, and conditions will not be controlled. We addressed this problem with the use of a PPG array and signal registration algorithm which, by assaying the optic location of the strongest PPG signal, can (a) determine whether or not the sensor has been properly positioned, and (b) optimize the quality of the PPG signal used in the blood pressure determination. Depending on the location of the digital artery, the signals captured by the individual photo detectors in the array may be different, as demonstrated in Figure 57. Some photo detectors along the light path going through the artery may capture strong pulsatile signals, whereas others may contain weak or no signals. Although the exact location of the artery is unknown, the photo detector having the largest signal may be identified by scanning all the signals coming out of the array. First, the device ensures that the best PPG signal is from one of the central PDs; if not, it indicates that the PDs are either too close or too far from the artery, and that the pressure probe is likely misplaced too.

The conditioned PPG analog signals are sampled and digitized. The data are passed through a 2nd order high-pass digital Butterworth filter ($F_c = 0.7$ Hz) to remove the non-pulsatile DC

component of the waveform. The filtered waveforms are next passed through a peak detection algorithm, such that the beat-to-beat maximum and minimum values of the PPG waveforms can be separated (Figure 58).

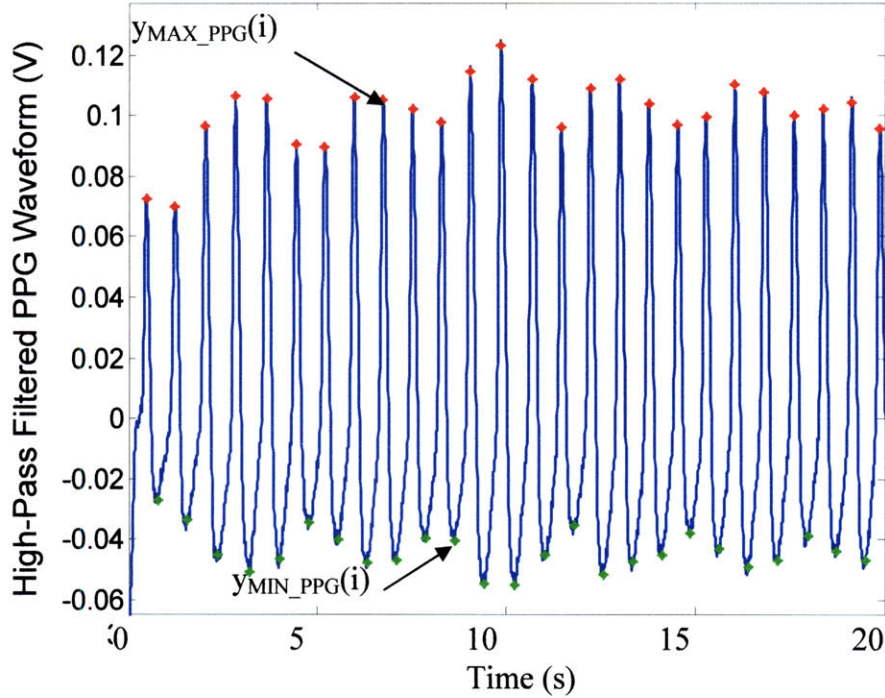


Figure 58: High-pass filtered PPG waveforms with detected maximum and minimum values (*).

Beat-to-beat amplitudes ($y_{AC_PPG}(i)$) are then calculated by subtracting the i^{th} beat's local minimum ($y_{MIN_PPG}(i)$) value from the corresponding beat's maximum value ($y_{MAX_PPG}(i)$).

$$y_{AC_PPG}(i) = y_{MAX_PPG}(i) - y_{MIN_PPG}(i) \quad (12)$$

Once each of the beat-to-beat amplitudes are calculated, spurious data points are removed by first averaging the amplitudes over five consecutive beats and by then further passing the averaged data points through a moving window 3-element median filter such that a single conditioned amplitude is yielded for every five beats, denoted $\bar{y}_{AC_PPG}(k)$. The measured external sensor pressure and the hydrostatic pressure measurements are simultaneously averaged

over the duration of each detected beat. Next, the maximum PPG amplitude \bar{y}_{AC_PPG} is extracted from the data set. Based on eq. (4) the zero-transmural pressure point is determined, and the mean arterial blood pressure is obtained as in eq. (5).

The scanning of the PPG amplitude data may be vulnerable to outliers. Therefore, a curve-fitting method is utilized on the preceding data. In particular, the conditioned amplitude data is fit to a Gaussian function of the form,

$$\hat{y}_{AC_PPG} = \beta_1 \exp \left[- \left(\frac{P_r - \beta_2}{\beta_3} \right)^2 \right] \quad (13)$$

where P_r is the applied reference pressure, $P_r = \rho \cdot g \cdot h + P_{ext}$; \hat{y}_{AC_PPG} is the estimate of the PPG AC amplitude predicted by the Gaussian model; and $\beta_1, \beta_2, \beta_3$ are the fitting coefficients of the model.

A traditional Levenberg-Marquardt algorithm [74, 75] was used for identifying the parameters $\beta_1, \beta_2, \beta_3$ from a set of data, P_r and \hat{y}_{AC_PPG} . To best elucidate the location of the true maximum, the non-linear curve is fit to the set of measured data points with amplitudes greater than 50% of the measured maximum conditioned PPG amplitude. Once the curve fitting is completed, the MAP is immediately obtained as

$$P_{MAP} = \arg \underset{P_r}{\text{Max}} \left[\hat{y}_{AC_PPG} \right] = \beta_2 \quad (14)$$

since the peak value of the Gaussian curve is at β_2 as shown in Figure 59.

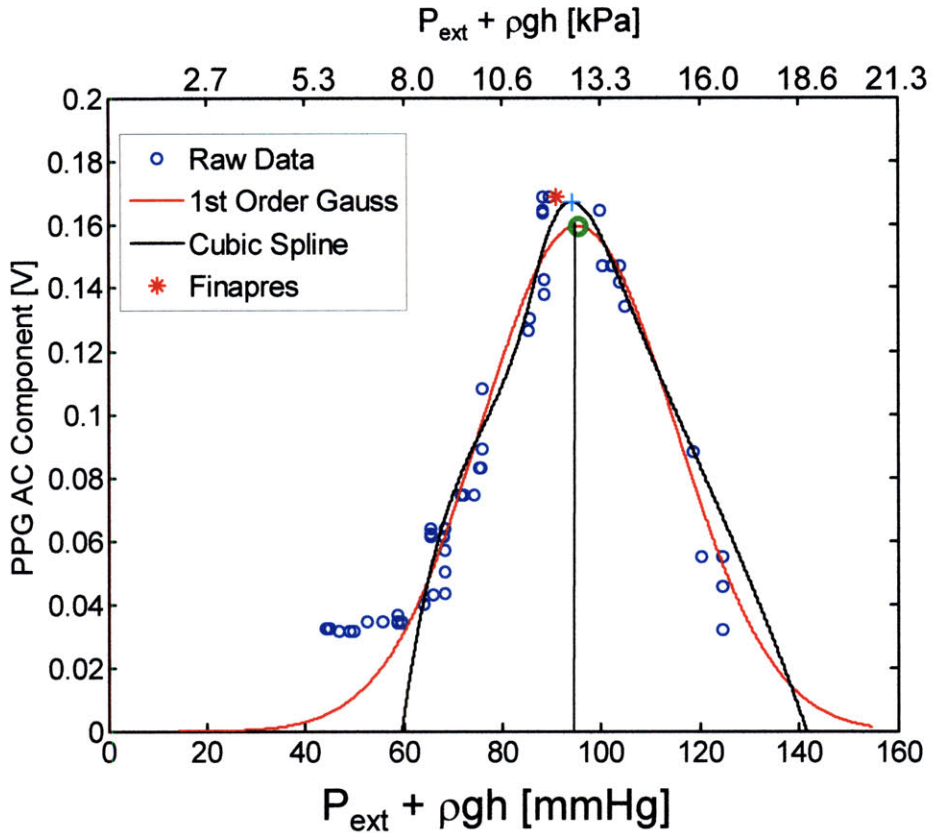


Figure 59: Example of the raw data with Gaussian curve fit.

The performance of two different methods for MAP estimation was compared, an estimation based on the discrete measured data points and a non-linear Gaussian fit estimation. Although the discrete method proved to be a reasonably reliable method for estimating the subject's MAP, we believe that less controlled settings may yield less consistent results. For example, it is likely that during the hydrostatic challenge, the true maximum will be between two arm height positions. The resulting data would then indicate an estimated MAP as much as 1.3 kPa (10 mmHg) away from the underlying true value.

A Gaussian model is able to represent the general bell-type shape anticipated from each challenge while providing a clear maximum value, represented by the model coefficient, θ_2 , in eq. (13). The bell-type shape could provide further utility in the estimation of both systolic and

diastolic blood pressures, as has been suggested by other authors [76]. The Gaussian fit may provide a better tradeoff between the estimations of these multiple parameters. For the work presented in this paper, the complete shape of the curve was less important than the curve's ability to accurately estimate the MAP (denoted by the location of the maximum value). To this end, we focused our data fitting to the conditioned PPG amplitudes with values greater than 50% of the discrete measured maximum value.

5.6 Data Acquisition and User Interface

The user interface for the sensor unit consists of two main sections, a sensor system calibration interface and a data acquisition/monitoring interface. Figure 60 illustrates the sensor calibration interface. Once the calibration interface is initiated, the user is able to calibrate all aspects of the ring sensor. The pressure sensor is calibrated by applying known loading conditions to the ring performing a linear transform to the measured voltages. Once the pressure sensor is calibrated, the user is then requested to attach the sensor and tighten the band to a pre-defined pressure range. Once the ring has been attached successfully, the height sensor is calibrated. After entering arm section lengths into the GUI, the program animation guides the wearer's arm through a series of orientations which are sufficient to fully calibrate the height sensor. The program next performs the PPG registration program before finally requesting that the user perform the hydrostatic blood pressure measurement procedure. During the hydrostatic measurement the user is again asked to follow the on-screen animation. Once the measurement is complete, the calibration GUI closes and the monitoring GUI is displayed.

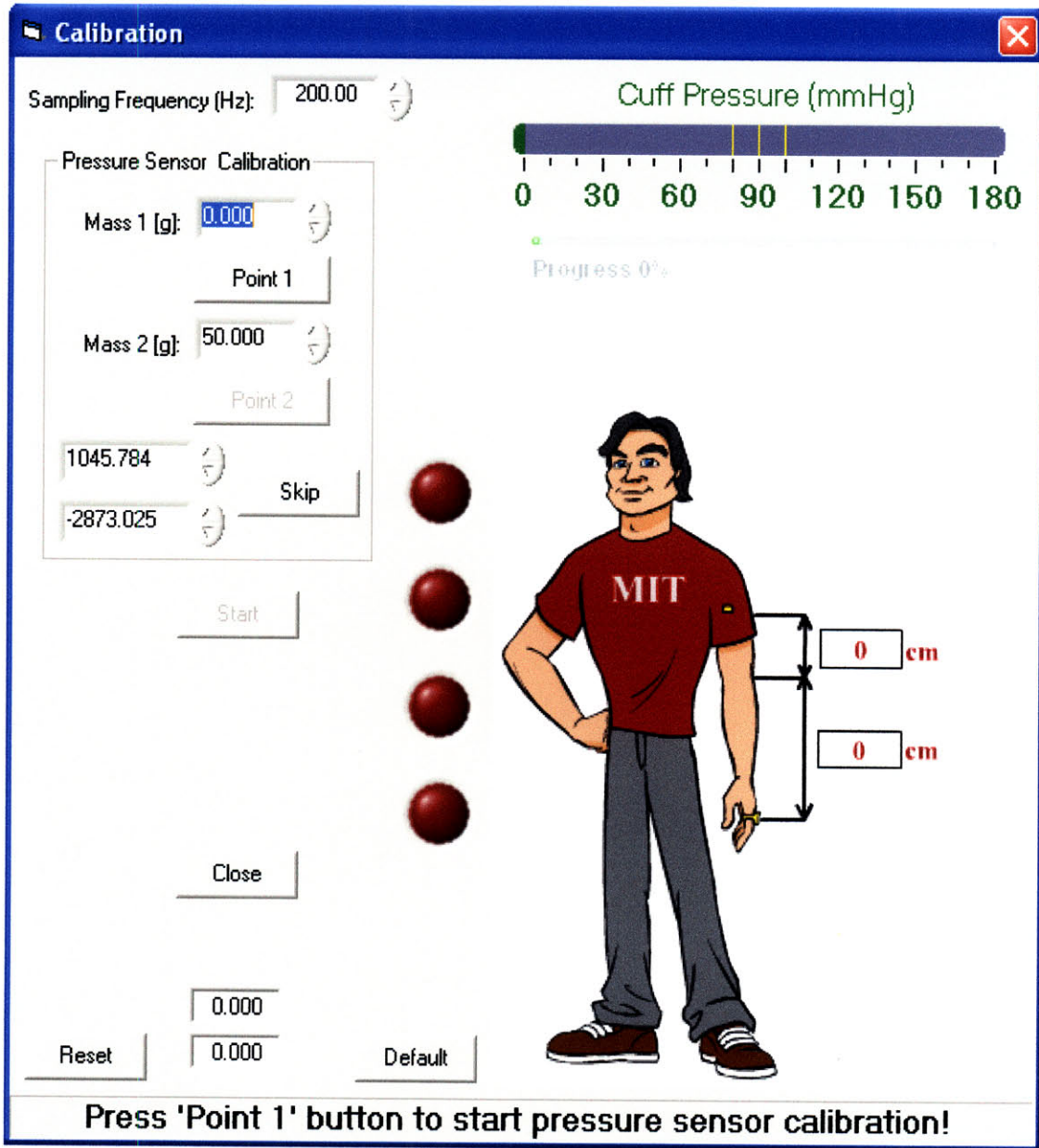


Figure 60: Windows-based GUI for the blood pressure sensor calibration and registration.

See Figure 61. The data acquisition and monitoring GUI provides output information for all of the on-board sensors. The Gaussian curve resulting from the initial sensor measurement is displayed along with the raw data and the measured blood pressure. Additionally, the program provides estimates of the systolic and diastolic blood pressures based on the Gaussian curve. Once started, the monitoring interface can independently re-register the PPG sensor and will then

display continuous PPG waveforms along with updating heart rate, cuff pressures, and arm heights.

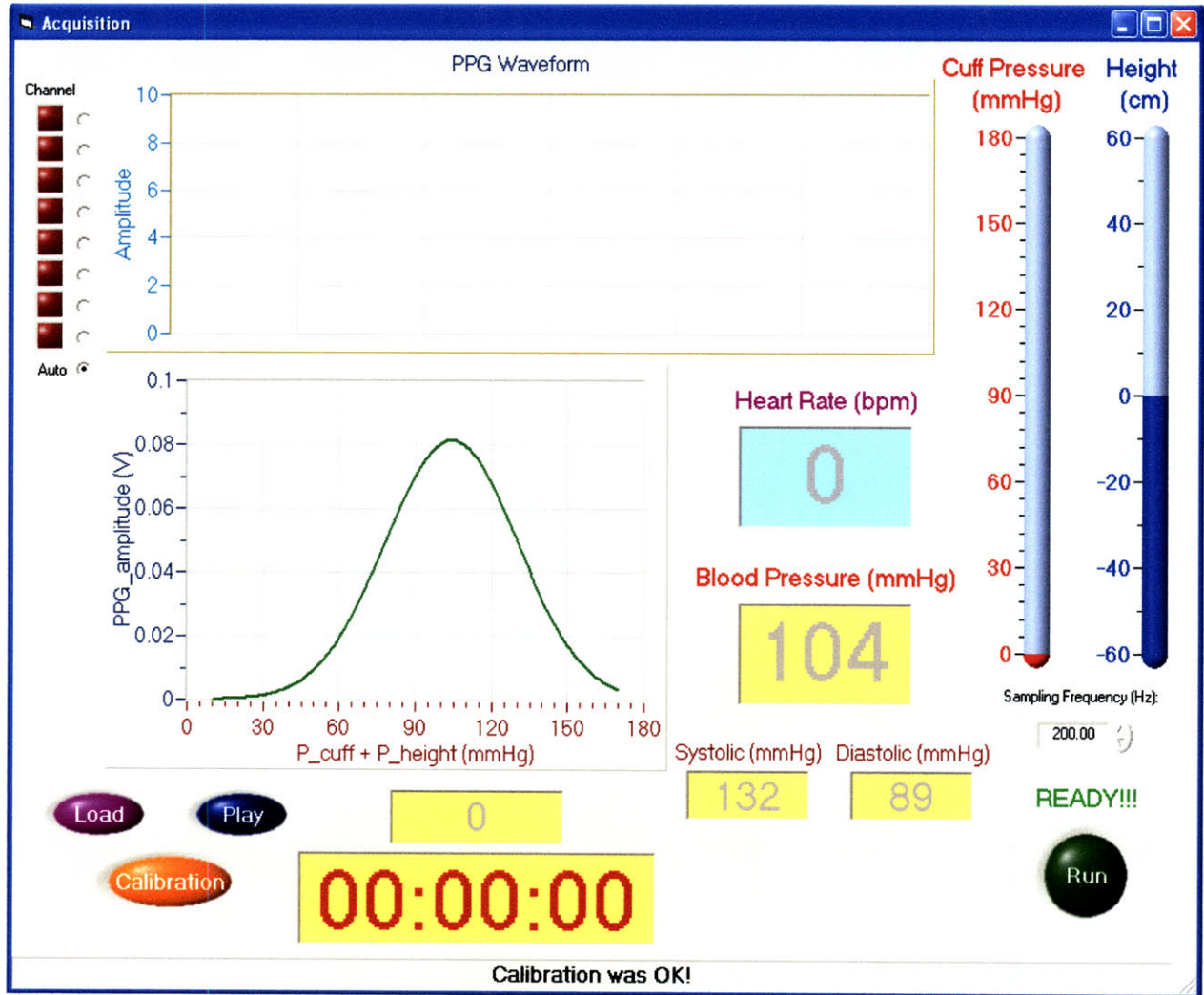


Figure 61: Data acquisition and sensor monitoring GUI.

5.7 Design Concept Considerations

The objective of this thesis is to develop technology leading to truly wearable blood pressure sensors based on oscillometry. It is recognized that blood pressure measurements made at the finger may be too distal to continuously recover central aortic pressure. However, it is also noted

that the increased convenience of a ring-based sensor may provide long-term ambulatory monitoring advantages which supersede other disadvantages of such a distal location. Furthermore, many of the same technologies implemented in this ring sensor embodiment may also be applicable in other implementations intended for use over the radial, femoral or even carotid arteries. Specifically, the traditional inflatable cuff design was replaced by one using an instrumented protrusion applying a low pressure locally to a palpable artery. The advantages of this approach were three-fold. First, this solid design (e.g. no inflatable cuff) enables a truly miniaturizable sensor, only a small probe the size of an artery flanked by the PPG sensor arrays. Second, depressing directly over the artery with a low pressure significantly minimizes venous occlusion associated with inflatable cuffs worn for long time periods. The traditional cuff squeezes circumferentially, subjecting much more tissue to elevated pressures, and causing distal hypoperfusion because of total venous occlusion. Third, application of pressure by an instrumented protrusion ensures that focal pressure to the underlying tissue isn't accidentally (and unaccountably) applied by any neighboring portion of the sensor's frame, which would be a source of error.

In addition to the cuff-less design, several functional requirements must be met to provide a non-invasive oscillometric blood pressure measurement. The sensor design and experimental protocol described in this thesis aim to achieve these requirements using a unique methodology and list of techniques summarized in Table 4.

TABLE 4: COMPARISON OF HOW A STANDARD OSCILLOMETRIC CUFF AND THE RING SENSOR SATISFY THE REQUIREMENTS FOR OSCILLOMETRY. EACH OF THE SOLUTIONS LISTED FOR THE RING SENSOR REPRESENT SPECIFIC INNOVATIONS.

Oscillometry Requirements	Standard NIBP cuff	Cuff-less PPG Ring Sensor
Apply pressure while allowing pulsatile volume changes	Air bladder	Uni-axially applied pressure by a solid contact
Measure relative volume changes	Pressure sensor connected to the air bladder measures pressure oscillations	PPG sensor unit measures optic oscillations
Measure <i>local</i> pressure / volume changes of artery	Large air bladder in circumferential cuff, not sensitive to location	PPG array ensures proper positioning over artery
Ensure negligible hydrostatic offset between measurement location and proximal aorta	Reliance on proper human technique taught to caregivers and home users	Height measurement with two wearable MEMS accelerometers
Vary transmural pressure	Pneumatic pump	Hydrostatic challenge protocol

The first column of the table lists the functional requirements for oscillometric solutions, the second column contains the traditional cuff-based oscillometry solutions, while the third column presents alternatives and the innovative solutions of the cuff-less PPG, ring sensor.

5.8 PPG for MAP Measurement Consideration

The PPG has long been held as a relative 'index' of blood volume [17]. However, prior to this work, it was not certain that the PPG signal could be used for oscillometric blood pressure measurement because there are many non-arterial blood vessels within the tissue whose blood content oscillates, altering the PPG [27]. Moreover, according to well-established optic theory, various focal pulsating vessels will have a complex non-linear effect on light-propagation through the tissue [20]. Therefore, it was hypothetical that the PPG signal could provide a suitable index of relative arterial volume without other blood vessels and non-linear optic effects as sources of major error. Our results suggest that, for the implementation described in this

paper, oscillometric photoplethysmography is suitable for mean arterial blood pressure measurement.

This oscillometric PPG was made possible using several key insights and technological advancements. First, only used the pulsatile AC component of the PPG waveform is used. In the course of this thesis, the DC component was extremely sensitive to environmental perturbations. These perturbations include non-arterial blood volume changes introduced by the attachment of the sensor, sympathetic changes associated with stress, or even changes in the surrounding ambient light levels. Although the AC component is occasionally affected by these disturbances as well, it has been found that the DC aspect of the PPG waveform is generally far less stable and consequently inappropriate for use in our current system design.

Chapter 6 ABP Measurement Protocol

6.1 Hydrostatic Protocol

The instrumented wearer's hand is raised to a comfortable height above the heart; typically this is between 40 – 60 cm. After an initial rest period of two minutes, the arm height is decreased from the highest position above the heart to the lowest position below the heart in decrements of 10 cm. Data are collected at each arm position for a period of 20 seconds before offline post-processing (Figure 62).

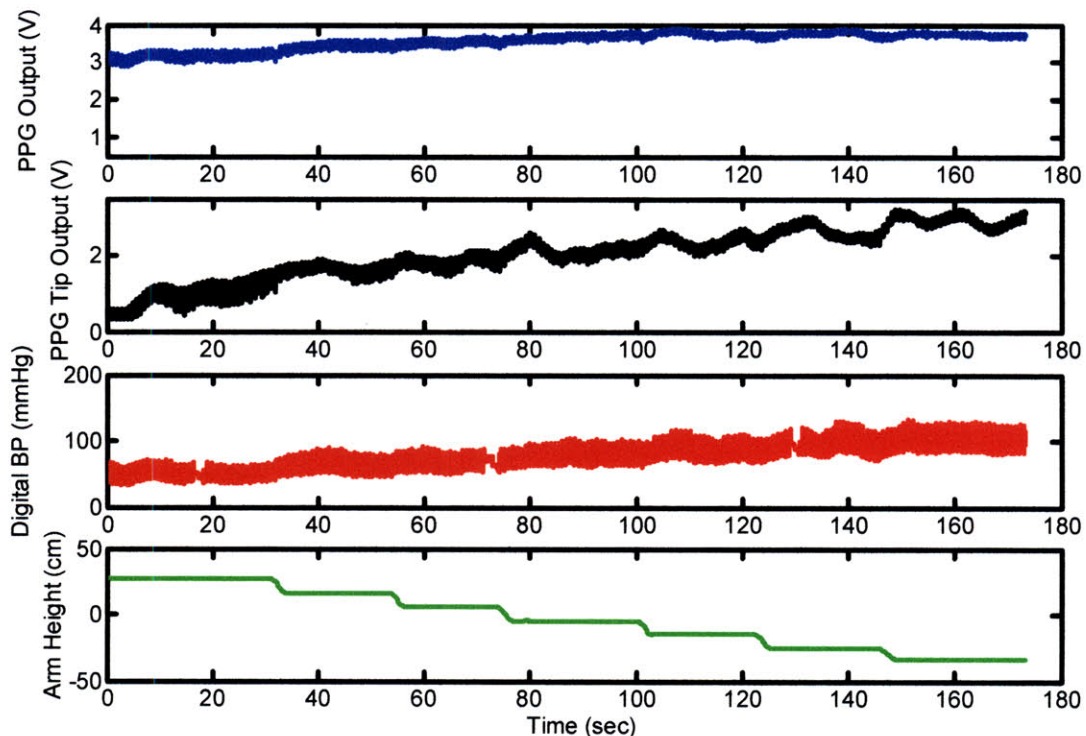


Figure 62: Plots of the (a) Fingerbase PPG output; (b) Fingertip PPG output; (c) Digital blood pressure; (d) Measured arm height during a typical 20 second/height experiment.

Each of the results was compared to the MAP provided by a simultaneous Finapres (Ohmeda 2300, Finapres BP Monitor) measurement. The MAP for the Finapres is determined from the averaged systolic and diastolic blood pressure values as follows:

$$\bar{P}_{MAP,Finapres} = \bar{P}_D + \frac{1}{3}[\bar{P}_S - \bar{P}_D] \quad (15)$$

where $\bar{P}_{MAP,Finapres}$ is the Finapres MAP, \bar{P}_D is the measured diastolic pressure averaged over five beats and \bar{P}_S is the measured systolic pressure averaged over five beats.

Tests conducted in the lab have indicated that rapidly performed calibrations (complete hydrostatic challenges which occur within 20 seconds) tend to be unrepeatably and may lead to inaccurate estimates of the subject's MAP [77]. Our studies have shown that hydrostatic challenges occurring over time frames of at least one minute lead to far more repeatable curves, as shown in Figure 63. The rest period of 20 seconds between each height change was conservative and intended to optimize the accuracy of PPG amplitude measurement at each height.

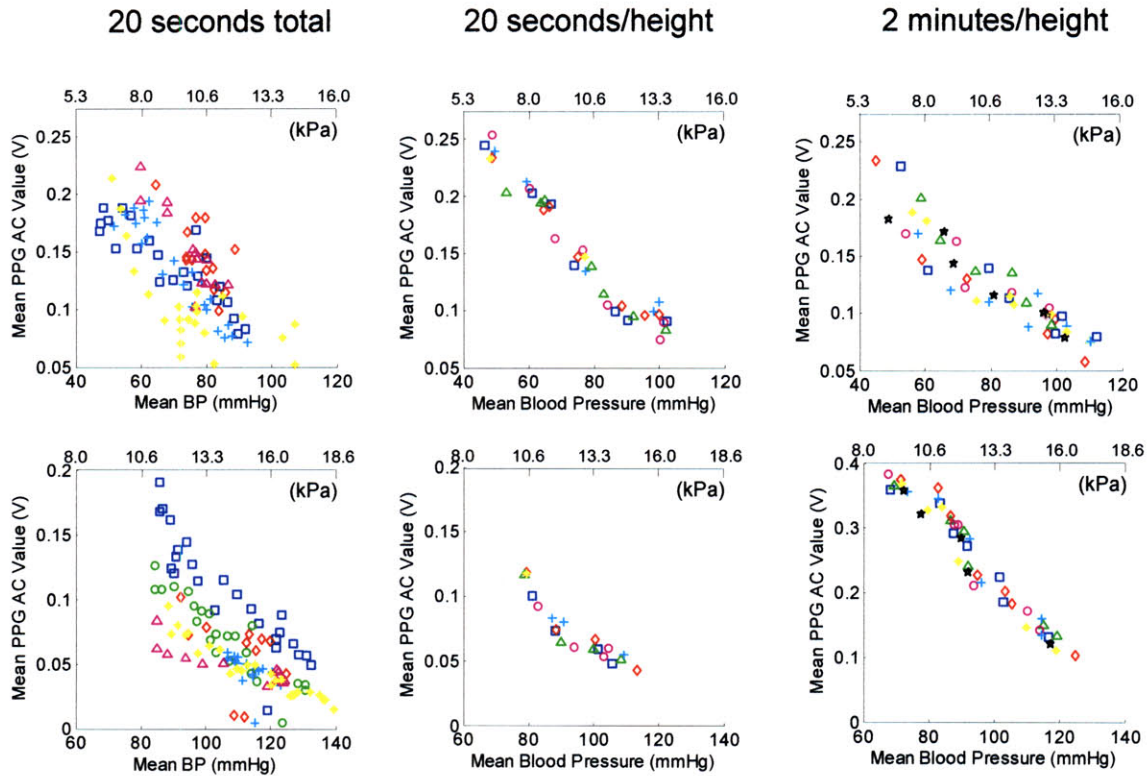


Figure 63: Plots for two subjects (Subject A shown in the top row, subject B in the bottom) comparing the repeatability of the hydrostatic challenge for various height change rates. Rapid calibrations appear to be less reliable than more gradual hydrostatic calibration routines.

6.2 Hydrostatic Protocol Considerations

One note about the pressure applied by the sensor: it was observed that this sensor design has a loading effect on the underlying PPG signal, which reaches steady-state within a minute or two, as shown in Figure 64. Therefore, for the experimental protocol, an acclimation period was provided before beginning the hydrostatic challenge protocol. A rest period of at least two minutes prior to the experimental protocol reduces the effects of rapid hydrostatic changes. It should be noted that the starting position of the arm has not been found to significantly affect the results of the challenge. However, it is important to allow time for the internal physiology to adjust to the altered pressure conditions.

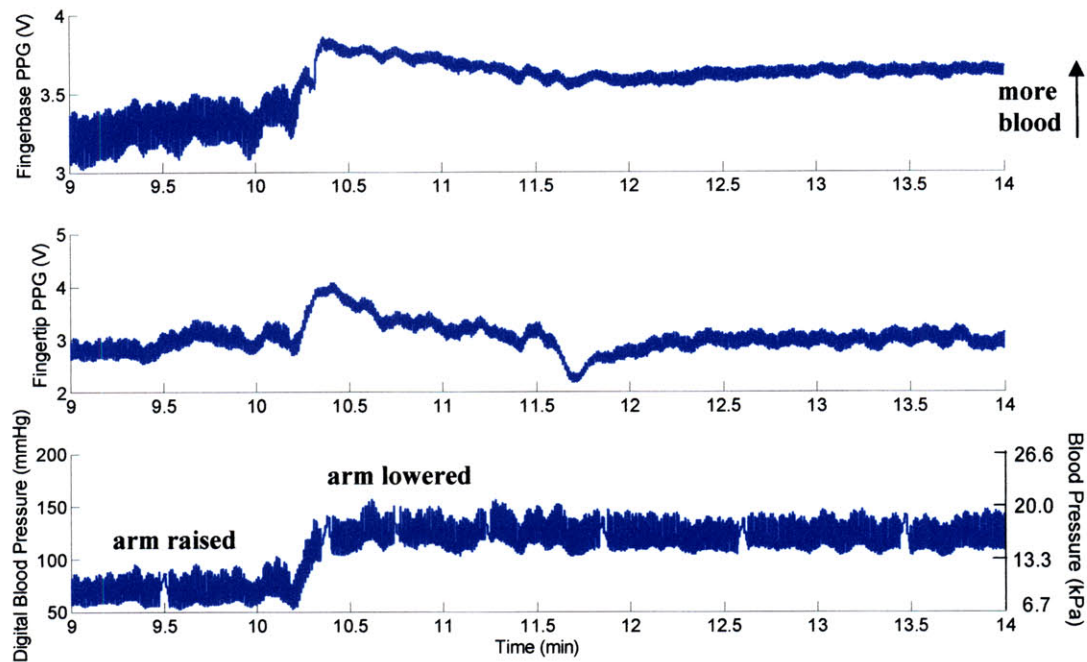


Figure 64: Plots comparing the measured responses of the finger base PPG, fingertip PPG, and blood pressure sensor (from top to bottom) during a large hydrostatic pressure change.

A novel oscillometric methodology was validated, in which the hydrostatic pressure in the artery is altered rather than the external pressure applied by the sensor. This approach offers a set of advantages: (a) there is no need for a large, power-thirsty, bulky external actuator (e.g. pneumatic pump, etc); (b) in theory, any time a user raises/lowers the extremity is an opportunity to make a “passive” blood pressure measurement; (c) because the external pressure is augmented by the hydrostatic pressure as shown in eq. (3), the external pressure does not have to be as high as the MAP, making the device more comfortable; and (d) it was found that the PPG signal is extremely sensitive to a sensor’s motion and position changes, and that the PPG amplitude can have an erratic relationship with P_{tm} if the external pressure is increased/decreased (e.g. externally squeezed / released the sensor). It is hypothesized that changing the applied sensor pressure can alter the optical path length and cause small alterations in sensor placement, relative

to the underlying artery, and therefore change the optic PPG signal. Although there are reports of a PPG used as part of an oscillometric device [78], the sensitivity of the PPG to small changes in applied sensor pressure can be a liability for novel PPG applications. Our hydrostatic challenge methodology offers a solution to this liability.

There are two limitations to the hydrostatic challenge methodology. Most importantly, it relies on an experimental protocol in which the user performed controlled extremity raising / lowering over a multiple-minute interval. In practice, it is unlikely that many real-world users would tolerate this on a regular basis. Secondly, although an applied pressure above the MAP is not required for measurements, a constant bias pressure of at least 8.0 kPa (60 mmHg) was still required for the experimental protocol (since the range of available transmural pressures is limited to the length of the of subject's arm, typically between 40-60 cm, a bias pressure is required to ensure that the zero-crossing point of the transmural pressure will be achieved). For both of these reasons, we anticipate that a truly wearable oscillometric blood pressure sensor will require some form of active sensor actuation, as described in this thesis which will require overcoming any path length change-related phenomena. Practically, it is expected that the hydrostatic challenge methodology will be complimentary to active sensor actuation: we can make use of the natural motion of the wearer, saving actuator power and regularly updating the PPG- P_{tm} curve from which ABP is estimated.

Chapter 7 Human Subject Testing

7.1 Blood Pressure Measurements

7.1.1 Compliance Curve Identification

Following the experimental procedure outlined previously, experimental protocol data were collected for 9 healthy volunteers (7 male, 2 female, average age: 29 ± 10 years). All data were collected in accordance with an experimental protocol approved by the Massachusetts Institute of Technology's Committee on the Use of Humans as Experimental Subjects (COUHES Approval No. 0403000233) and following Federal regulations for the protection of human subjects established by 45 CFR 46. Figure 65 shows both the raw data and the accompanying non-linear Gaussian fits for each of the nine subjects tested. Recall that the Gaussian fits for each of the subjects were applied to the conditioned PPG amplitude data with values greater than 50% of the maximum value only.

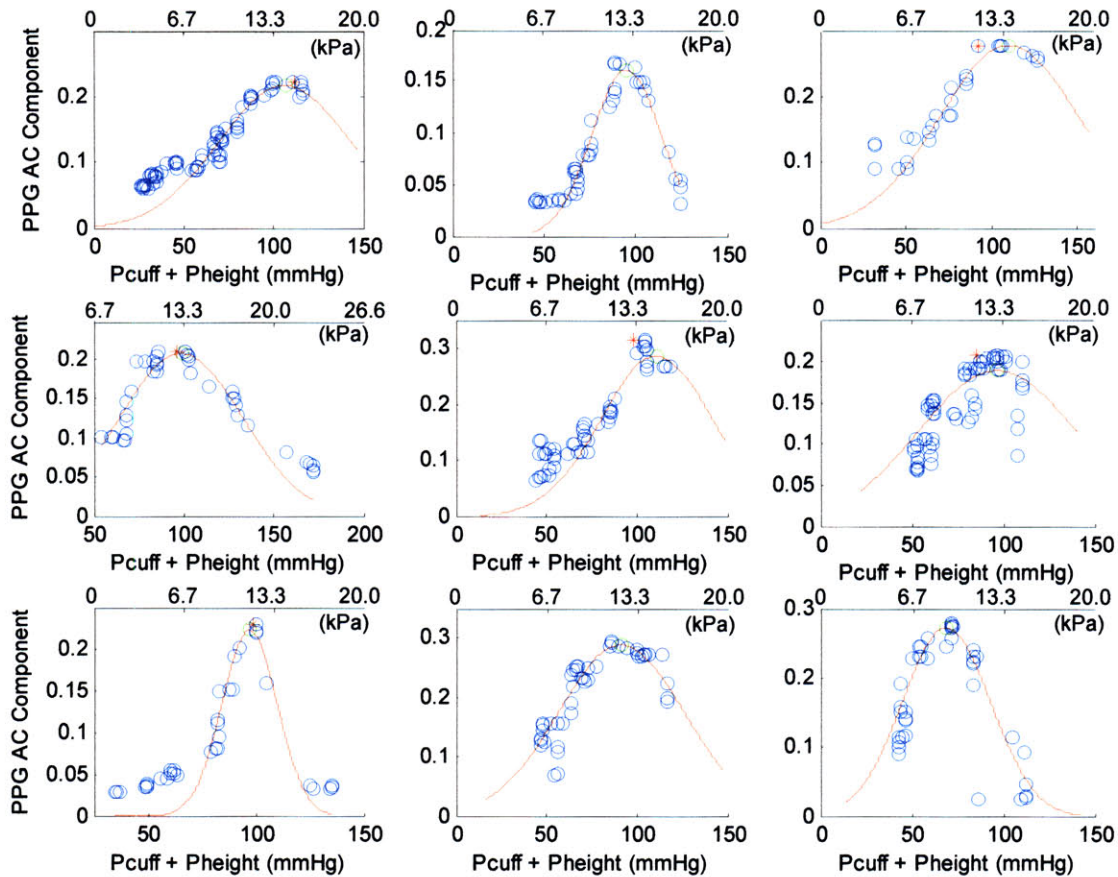


Figure 65: Comparison of the compliance curves with Gaussian fit models generated by the hydrostatic challenge. The conditioned PPG amplitudes are represented by discrete data points (o); Gaussian fits applied to the raw data are shown with continuous lines.

As a result of this strategy, there is a divergence between the models and the data points below the threshold amplitude. Each of the provided figures demonstrates the bell-shaped relationship existing between the applied reference pressure and the conditioned AC amplitude component of the PPG waveform.

7.1.2 Systolic and Diastolic Pressure Estimation

In addition to MAP measurements, systolic and diastolic blood pressures can be invaluable tools for proper diagnosis and treatment. Using a technique analogous to methods employed in

traditional oscillometry, the systolic and diastolic blood pressures can be estimated from the curve generated by the proposed hydrostatic challenge. For the proposed method, the systolic pressure was estimated to occur at a particular fraction of the measured maximum pulsatile PPG amplitude, particularly,

$$\bar{P}_S = 0.51 * \underset{P_r}{\text{argMax}}(\hat{y}_{PPG_AC}) \quad (16)$$

It is then straightforward to estimate diastolic pressures by substituting the mean and systolic pressure measurements into (15). Graphically, the relationship of the three pressure measurements to the hydrostatic challenge compliance curve is illustrated in Figure 66.

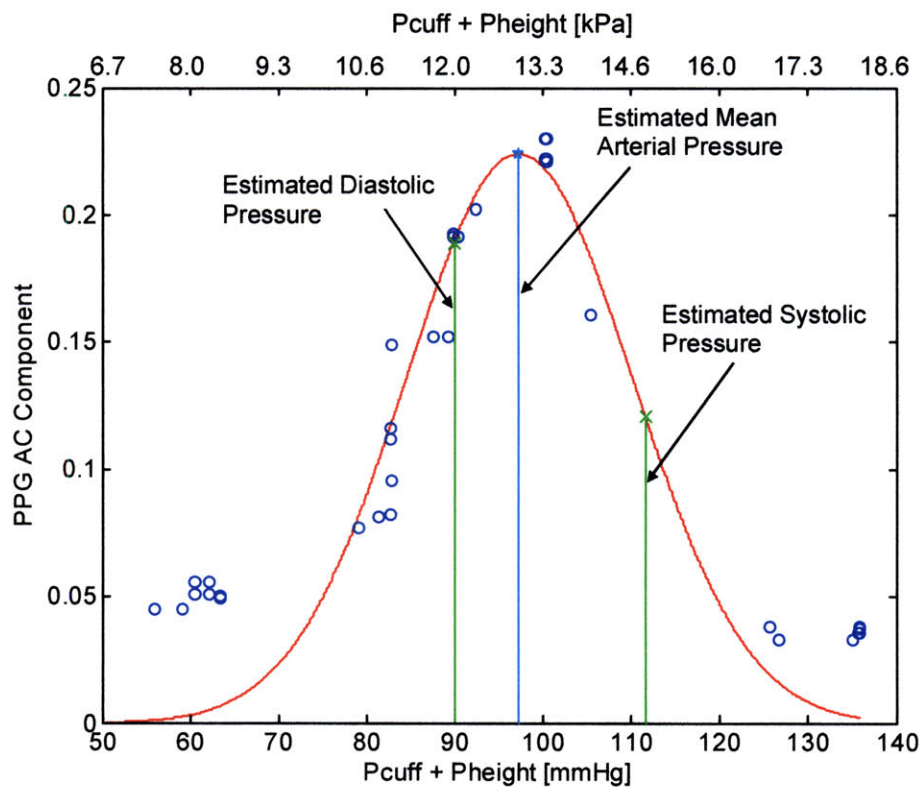


Figure 66: Hydrostatic challenge derived compliance curve with Gaussian fit model. PPG amplitudes are represented by discrete data points (o); Measured values for the mean, systolic/diastolic blood pressures are illustrated in the figure. Specifically, for the hydrostatic method (in mmHg): MAP = 97, Systolic/Diastolic = 113/90; for the Finapres (in mmHg): MAP = 97, Systolic/Diastolic = 121/85.

The results of this method for measuring the systolic and diastolic pressure are shown in Figure 67. The results demonstrate an excellent correlation between the ring sensor's blood pressure measurements and the Finapres measurements.

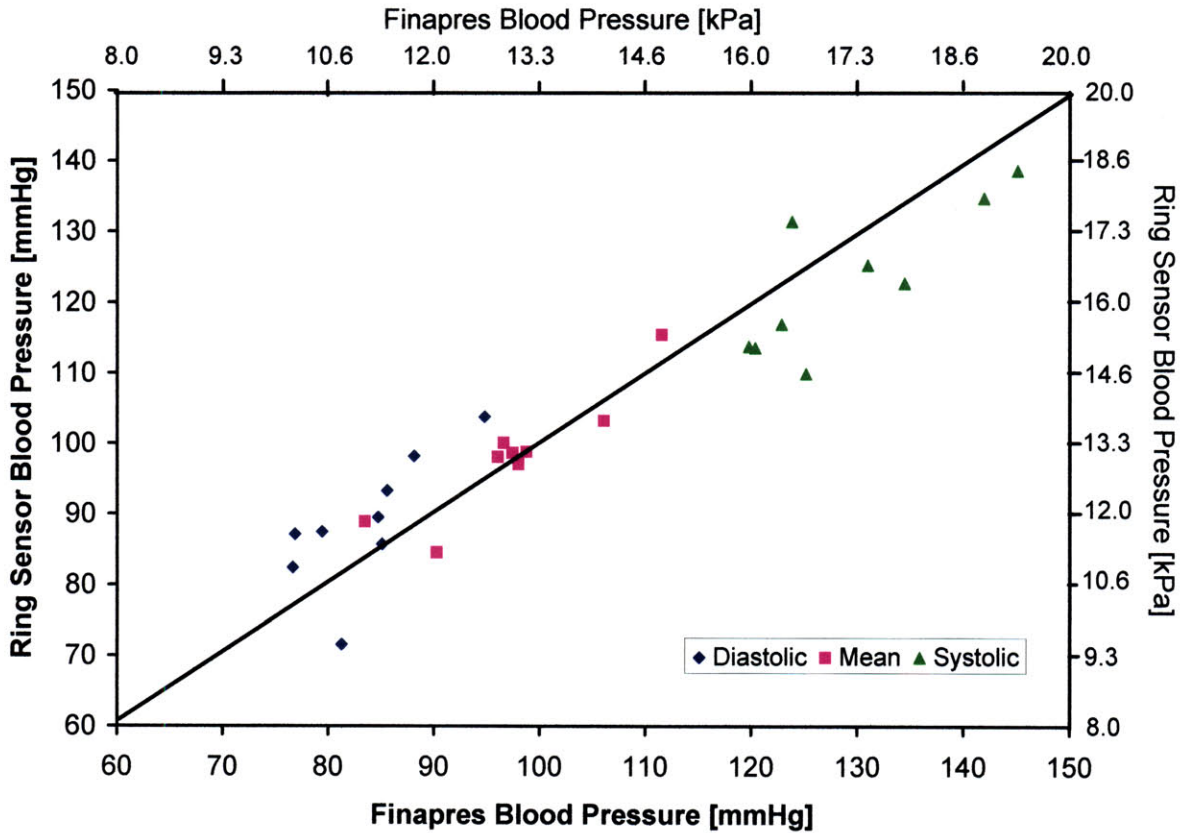


Figure 67: Comparison of the Finapres and Ring Sensor diastolic, mean and systolic blood pressure measurements for nine subjects.

7.1.3 Bland-Altman

The performance of the various methods for estimating the patients' mean arterial pressures was compared using a standard Bland-Altman comparison. The Bland-Altman statistics (limits of agreement represent the 95% confidence interval) are provided in Table 5 along with the accompanying percent error between the Finapres MAPs and the estimated MAPs.

TABLE 5: BLAND-ALTMAN 95% LIMITS OF AGREEMENT AND THE PERCENT ERROR BETWEEN THE FINAPRES AND THE PROPOSED MAP ESTIMATION METHODS.

Comparison Pair	Bland-Altman	Percent Error (%)
Finapres – Raw Data	[6.91, -9.04]	3.02
Finapres – Gaussian Fit	[10.57, -17.79]	6.45

Chapter 8 Continuous ABP Estimation

Up to this point, the thesis has focused on the requirements for one-time blood pressure measurements acquired using the proposed hydrostatic challenge. Although this method demonstrates a significant advancement in wearable blood pressure monitoring, it is believed that the true potential of the method and device will only be realized as a part of a continuous blood pressure monitoring scheme. To this end, a simple approach to continuous blood pressure monitoring is now offered. The proposed method incorporates the hydrostatic challenge as a means of first calibrating the non-linear relationship between transmural pressure and the measured PPG signal and subsequently using this calibration curve as a reference for future blood pressure measurements.

The primary assumption of the implemented continuous method is that the non-linear curve relating the PPG output to the underlying BP is reasonably static in nature. Using this assumption, it is possible to update the estimated BP parameters using the PPG amplitude, height sensor, and cuff pressure measurements. See Figure 68.

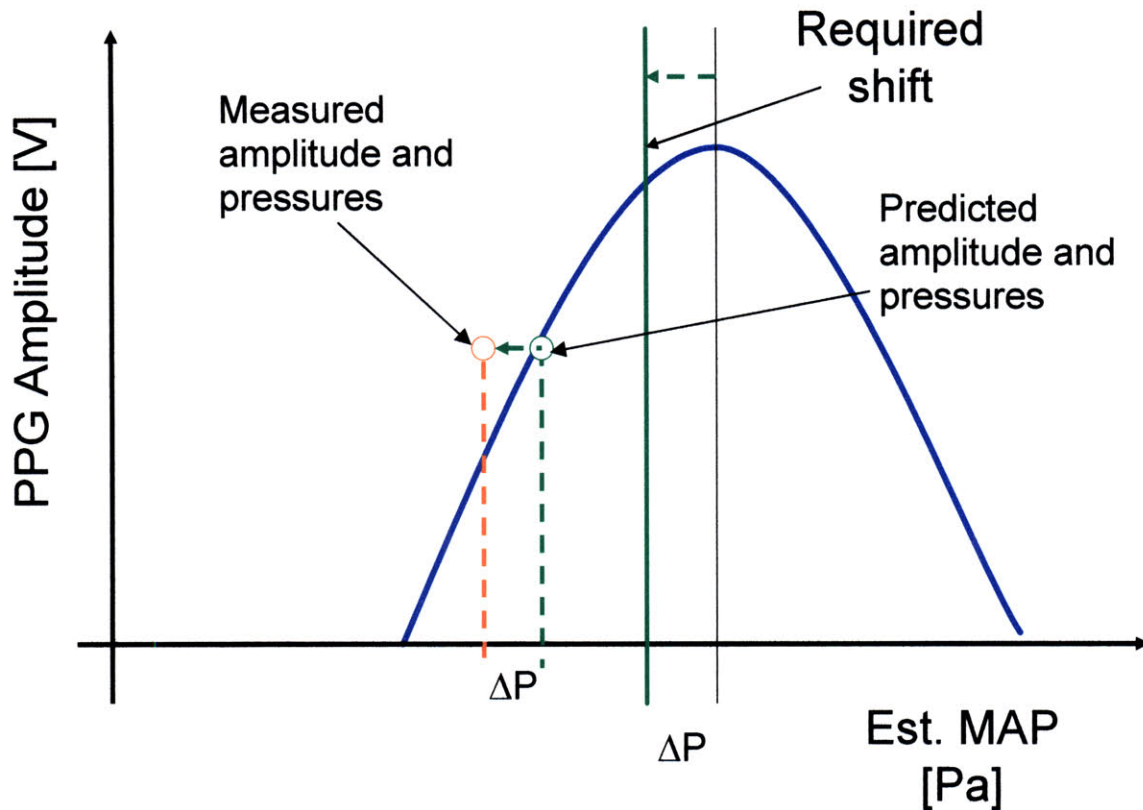


Figure 68: Illustration of a method for continuous blood pressure measurements.

Starting with the hydrostatic calibration curve, a new set of sensor measurements is read into memory. The operating point on the calibration curve is located by examining the new PPG amplitude data. From the operating point, a corresponding pressure value is located and compared to the sum of the new height and cuff pressure measurements. If the new pressure values are different than the predicted calibration curve pressure, the mean blood pressure has changed. As a result, the calibration curve is shifted such that the estimated PPG amplitude corresponds to the correct measured pressures. The pressure corresponding to the maximum amplitude is the new mean arterial pressure. This procedure is then repeated for each new set of sensor measurements.

The validity of this method was tested on healthy volunteers under controlled laboratory conditions. The first set of experiments focused on demonstrating the consistency of the calibration curve over the span of one hour. In particular, the hydrostatic calibration was repeated several times over the course of an hour and the resulting calibration curves were subsequently compared. The experiment was straight-forward and consisted of only the ring sensor with height sensor. After a two-minute acclimation period, the volunteer was asked to perform a hydrostatic challenge. Upon completion of the challenge, the subject's instrumented arm was returned to a rest position at heart level for a time of five minutes. This procedure of performing a hydrostatic challenge followed by a brief rest period was repeated for one hour.

In general, it was found that under controlled laboratory conditions a single calibration curve remained representative of the PPG-BP system for time spans up to ~10 minutes (Figure 69).

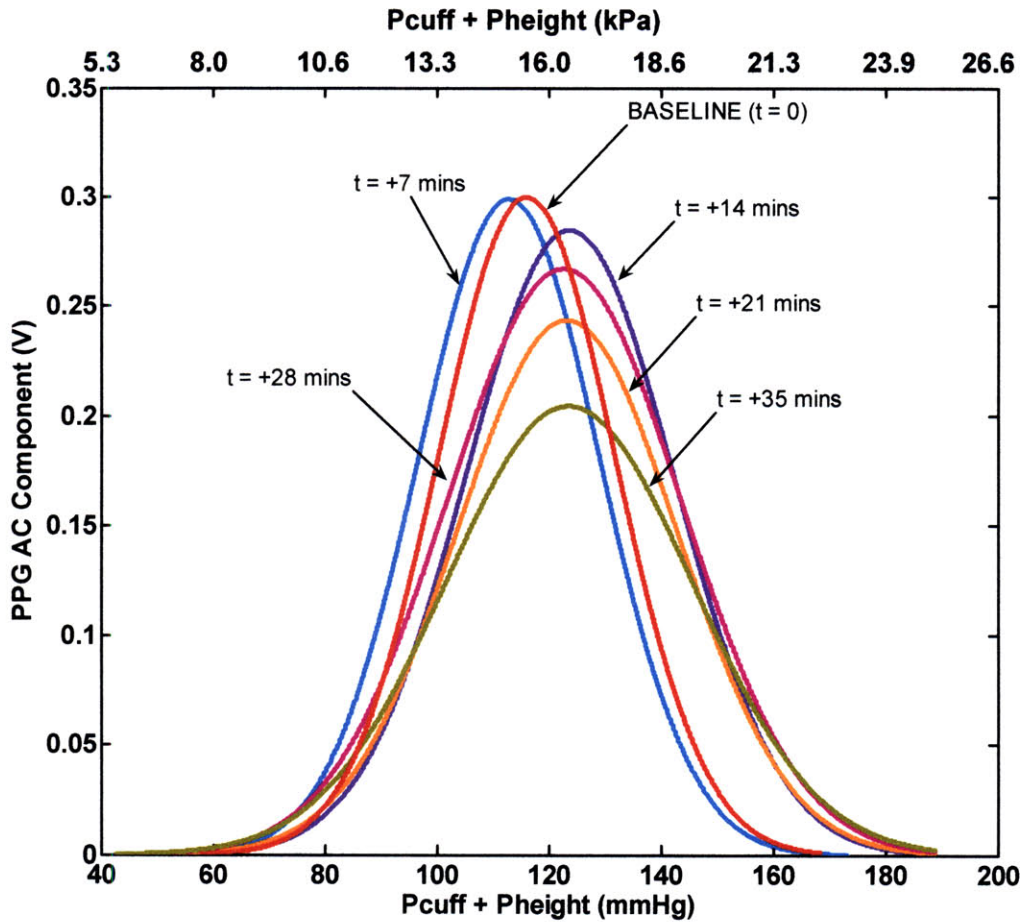


Figure 69: Comparison of the hydrostatic calibration curves generated over a 35 minute period of time.

After 10 minutes, both the observed amplitude and the width of the calibration curve appeared to change significantly. In fact, the amplitude of the calibration curve appeared to oscillate over the course of the hour. The oscillations could be due to local regulatory mechanisms or could possibly be related to the overall sympathetic tone of the volunteer. Changes in the width of the calibration curve are likely associated with changes in pulse pressure which occurred over the course of the experiments.

A second set of experiments was conducted to compare the continuous mean arterial blood pressure estimates resulting from a single hydrostatic calibration with an established non-invasive alternative (Finapres). Under controlled laboratory conditions, the volunteer was first

instrumented with the ring sensor positioned at the base of the middle digit; the Finapres was attached to the index finger of the corresponding hand. Following a two minute acclimation period of rest with the arm kept at heart level, the subject was instructed to perform the hydrostatic challenge before returning the instrumented arm to heart level. Once completed, continuous data from the ring sensor and Finapres device were sampled and stored for 45 minutes. Using the procedure outlined previously continuous mean arterial blood pressure values were estimated from the PPG amplitude data. Figure 70 demonstrates the findings from this work. It is interesting to note that using only a single hydrostatic calibration the mean arterial blood pressures track closely for about 15 minutes before diverging.

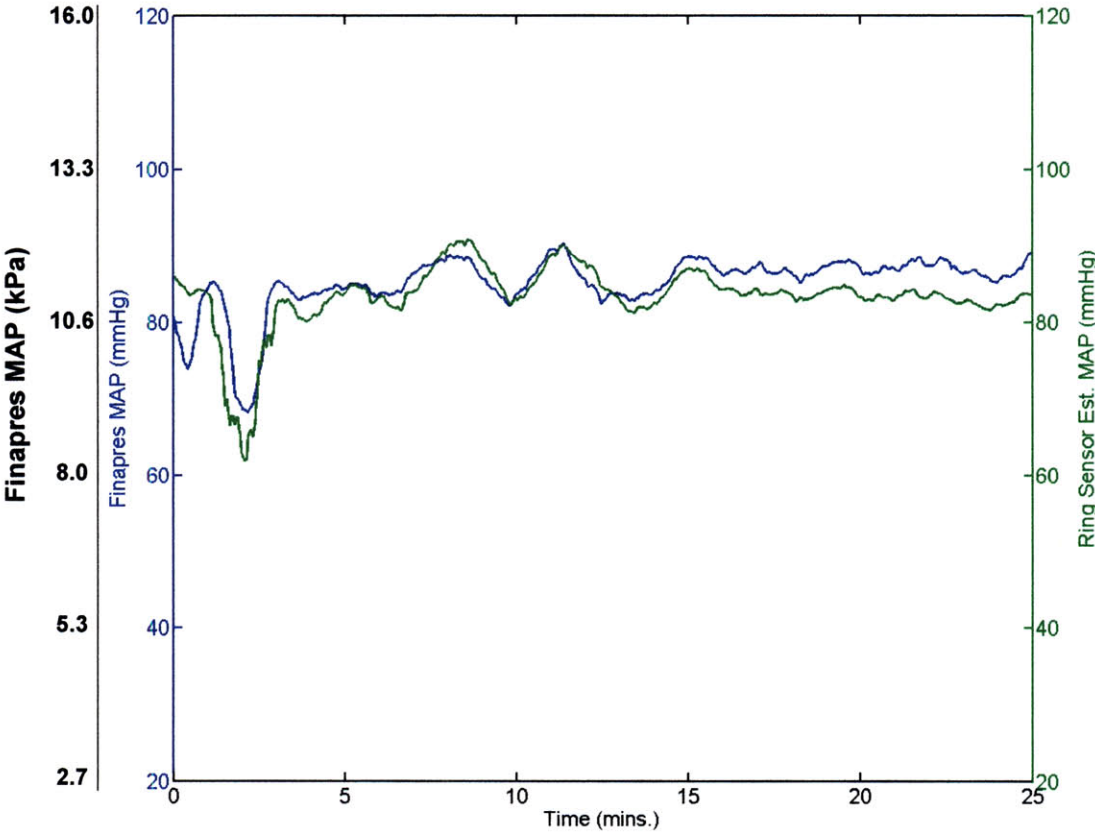


Figure 70: Comparison of continuous MAP measurements provided by a Finapres device and the Ring Sensor.

Additionally, during the 30 minute monitoring period we found that the finger monitored with existing method for continuous blood pressure (i.e. the Finapres) had become a deep shade of purple in color and was claimed to be numb, suggesting that significant venous pooling had occurred due to the large circumferential pressures. A finger simultaneously monitored with the ring sensor was a healthy flesh tone and no noticeable discomfort was described ().

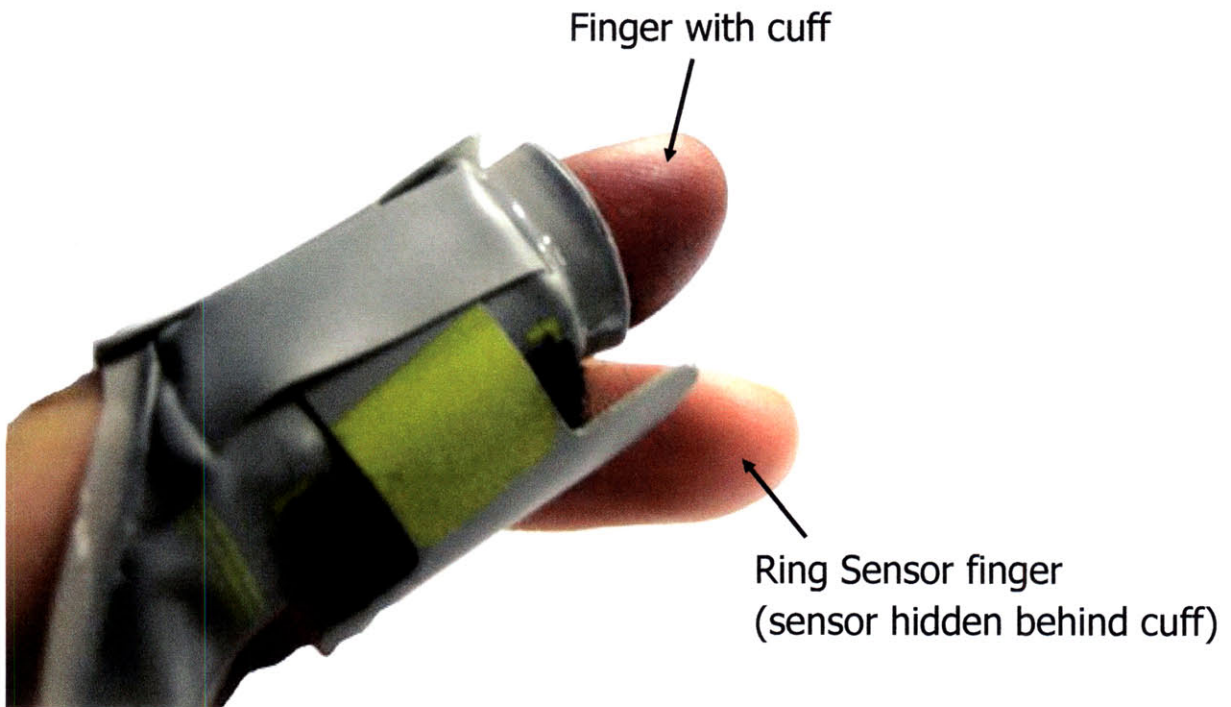


Figure 71: Comparison of two fingers immediately after long-term monitoring experiment. The Finapres finger is a deep shade of purple while the ring sensor finger is a healthy flesh tone.

Chapter 9 Conclusions

9.1 Summary of Contributions

This thesis presents a new method and device capable of non-invasively monitoring a patient's blood pressure. The main results of this thesis are as follows:


- A novel hydrostatic-based method for cuffless blood pressure measurement has been detailed. The method varies a subject's local transmural pressure without the need for a circumferentially occlusive pressure cuff. Instead, the protocol utilizes the natural hydrostatic pressure changes associated with raising and lowering an arm to measure a patient's blood pressure. The proposed method has far-reaching applications beyond the work presented in this thesis. The hydrostatic method has already been found to be useful in pulse wave velocity applications and could be incorporated into existing oscillometric devices.
- A nonlinear finite element model of a finger base was developed. The finite element model was tuned with published material parameters and validated with a combination of magnetic resonance images and experimentally measured tissue stiffness values. Numerical simulations of the model have been used to gain insight into the mechanisms of pressure propagation within the finger. The model provides a useful tool for guiding future developments of the sensor system.
- A miniaturizable monitoring unit containing all of the sensors necessary for monitoring blood pressure in a package the size of a quarter was created. The unit is designed to

apply a local, non-circumferential pressure directly to wall of the digital artery. The design makes it possible for the sensor to be worn for extended periods of time without significantly impeding blood flow throughout the finger. Data acquisition and sensor calibration software accompany the sensor system.

- A tetherless height system consisting of two accelerometers was constructed to eliminate the need for fluid-filled columns when providing continuous arm height measurement. The sensor has been shown to be compact, unobtrusive, and requires less than 5V of power for operation.
- The measurement method and sensor system have been validated on 9 healthy volunteers. Mean arterial blood pressure measurements were found to be within 3% of Finapres measurements. The method was additionally shown to be capable of providing systolic and diastolic blood pressure information.
- A method for continuous blood pressure monitoring has been proposed and has been demonstrated to be effective for monitoring a patient's blood pressure for as long as 10 minutes without the need for additional recalibrations or sensors.

Our results, when compared with a commercially available Finapres NIBP unit, demonstrate the ability of a nearly imperceptible finger sensor to reliably measure mean arterial pressure for extended periods of time.

Appendix A. Approved Study Protocol

	Massachusetts Institute of Technology Committee on the Use of Humans as Experimental Subjects	Application # (assigned by COUHES)	
		Date	

APPLICATION FOR APPROVAL TO USE HUMANS AS EXPERIMENTAL SUBJECTS (STANDARD FORM)

Please answer every question. Positive answers should be amplified with details. You may mark N/A where the question does not pertain to your application. Any incomplete application will be rejected and returned for completion. A completed **CHECKLIST FOR STANDARD APPLICATION FORM** must accompany this application.

Basic Information

1. Title of Study	
Multi-Sensor Fusion for Remote Circulatory Monitoring	
2. Principal Investigator	
Name: H. Harry Asada	Building and Room #:
Title:	Email:
Department:	Phone:
3. Associated Investigator(s)	
Name:	Email:
Title:	Phone:
Affiliation:	
4. Collaborating Institutions. <i>If you are collaborating with another institution(s) then you must obtain approval from that institution's institutional review board, and forward copies of the approval to COUHES)</i>	
5. Location of Research. <i>If at MIT please indicate where on campus. If you plan to use the facilities of the Clinical Research Center you will need to obtain the approval of the CRC Advisory Committee. You may use this form for simultaneous submission to the CRC Advisory Committee.</i>	
6. Funding. <i>If the research is funded by an outside sponsor, please enclose one copy of the research proposal with your application. A draft of the research proposal is acceptable.</i>	
Source:	Contract or Grant Title:
Contract or Grant #:	OSP #:

7. Human Subjects Training. All study personnel **MUST** take and pass a training course on human subjects research. MIT has a web-based course that can be accessed from the main menu of the COUHES web site. COUHES may accept proof of training from some other institutions. List the names of all study personnel and indicate if they have taken a human subjects training course.

Anticipated Dates of Research

Start Date:	Completion Date:
-------------	------------------

STUDY INFORMATION

1. Purpose of Study. Please provide a concise statement of the background, nature and reasons for the proposed study. Use non-technical language that can be understood by non-scientist members of COUHES.

The remote monitoring of beat-to-beat hemodynamics for continuous periods of weeks, months, or years, could prove revolutionary as a tool for the study, diagnosis and management of cardiovascular (CV) disease. Remote CV monitoring would likely be valuable for individuals in hazardous duty (such as firefighters or soldiers), and in monitoring individuals in the community predisposed to circulatory dysfunction (chronic heart failure patients, the elderly), as well as traditional hospital patients. Data from longterm remote monitoring could improve the diagnosis and treatment of chronic CV conditions such as hypertension, heart failure, and peripheral vascular disease. Such tasks necessitate wearable sensors on the body which can be worn for days at a time, yielding real time data. Existing sensor modalities that are able to make useful hemodynamic and vascular measurements are not actually wearable, whereas existing wearable sensor modalities record biosignals that are problematic for medical applications. There are four key shortcomings to these wearable biosensor (WBS) modalities: a) each measured signal is altered by the location in which the measurement is made; b) each signal is determined by an uncertain combination of central hemodynamic and local effects; c) each signal lacks information necessary to characterize the central state; and d) each signal may be corrupted by local sources of noise such as physical movement and muscular bioelectrical signals. Furthermore, wearable biosensors must be compact, low power consumption, and tether-free so that the sensors can be worn for a long time. There is no single WBS modality that meets all the requirements. To overcome these problems, we are working on a new multi-modality sensor system and a novel sensor fusion method to enable long-term remote circulatory monitoring.

2. Study Protocol. For *biomedical, engineering and related research*, please provide an outline of the actual experiments to be performed. Where applicable, provide a detailed description of the experimental devices or procedures to be used, detailed information on the exact dosages of drugs or chemicals to be used, total quantity of blood samples to be used, and descriptions of special diets.

For applications in the **social sciences, management and other non-biomedical disciplines** please provide a detailed description of your proposed study. Where applicable, include copies of any questionnaires or standardized tests you plan to incorporate into your study. If your study involves interviews please submit an outline indicating the types of questions you will include.

You should provide sufficient information for effective review by non-scientist members of COUHES. Define all abbreviations and use simple words. Unless justification is provided this part of the application must not exceed 5 pages.

Attaching sections of a grant application is not an acceptable substitute.

The purpose of this protocol is to collect rudimentary data for developing a new system

that can estimate arterial blood pressure and cardiac output (the volumetric rate of blood pumped by the heart) using strictly wearable sensors. This study is designed to expose subjects to zero risk, as explained later.

Wearable sensors refer to very small, light, unobtrusive sensors that can be placed noninvasively on a subject with minimal or no restriction on that subject's activities. Ideally, the sensor should be no more obtrusive than a wristwatch or bandaid. Presently, there are noninvasive methods for measuring arterial blood pressure (ABP) and cardiac output (CO). These include FDA-approved devices such as Medwave's Vasotrac blood pressure monitoring device, which involves a bulky wrist sensor and a subject remaining quite motionless, and Cardiodynamics bioimpedance cardiac output monitor, which involves electrodes placed on the subject while the subject remains very still and doesn't breath deeply. Needless to say, while these technologies permit the noninvasive monitoring of important physiologic phenomena, they are far from wearable.

It is our research plan to employ sensor modalities that are truly wearable, including electrodes and small photosensors, to estimate ABP and CO. The electrodes permit measurement of the heart's electrical activity, the electrocardiogram (ECG) as well as pulsatile changes in tissue electrical impedance related to pulsatile changes in blood volume (EBI). The photosensors permit measurement of changes in light absorption related to pulsatile changes in skin blood volume, known as photoplethysmography (PPG) as well as the percentage of the oxygen binding sites occupied by oxygen in the arterial hemoglobin, known as pulse oximetry. The challenge, therefore, is to use the signals obtained from wearable modalities, the EBI, ECG, and PPG biosensors, to estimate ABP and CO. For experimental purposes, we will use well-established noninvasive techniques to measure the ABP and CO as gold-standards, while we also measure signals using the sensor modalities that are wearable.

For the "gold-standard" measurements, we will use off-the-shelf monitoring equipment intended to measure ABP and CO. For ABP, this may include a tonometer solution such as Medwave's, or another tonometer solution such as Colin's or Biopac's, or the Finapres non-invasive blood pressure technique that involves PPG plus a finger pressure cuff. These technologies are all well established and are provided by vendors with the intention of human use. The only possible risk would be discomfort, and patients will be asked repeatedly if they are comfortable; if not the experiment will terminate. The equipment will be kept clean using hospital-grade cleansers. The equipment will be visually inspected before each experiment and perceptible damage or degradation of the equipment due to repeated use (i.e. break in cable insulation, damage to any protective coverings, etc) will lead to rescheduling of that experiment and replacement of the equipment.

For CO, off-the-shelf solutions include Cardiodynamics and Biopacs bioimpedance techniques for measuring CO (another option includes using the ABP signal to estimate CO using established techniques). These technologies are all well established and are provided by vendors with the intention of human use. The only possible risk would be discomfort, and patients will be asked repeatedly if they are comfortable; if not the

experiment will terminate. The equipment will be kept clean using hospital-grade cleansers. The equipment will be visually inspected before each experiment and perceptible damage or degradation of the equipment due to repeated use (i.e. break in cable insulation, damage to any protective coverings, etc) will lead to rescheduling of that experiment and replacement of the equipment. Subjects may need to hold their breath for the CO measurement; this period will be kept <15 seconds, and any preexisting cardiovascular or pulmonary disease will exclude the subject from the investigation.

Finally, the subject will be measured using PPG and EBI sensors. These sensors will be approved prototype sensors built in our lab, in addition to commercially available medical sensors. These prototype sensors were designed to expose subjects to zero foreseeable risk. Of note, we have previously used our prototype sensors in investigations at Massachusetts General Hospital (MGH). Our sensors were tested and fully approved for safety first by MGH Bioengineering (Patricia Volpe - PVOLPE@PARTNERS.ORG) for an independent assessment that our medical instrumentation meets all federal guidelines for patient safety. We also received IRB approval from the Partners Healthcare/MGH IRB (IRB No.: 2001-001462). Finally, we conducted our experiment in 16 subjects. There were no adverse events. During said testing each subject was surveyed as to the level of discomfort, if any, experienced while wearing the PPG-based sensor. The results of the survey indicated that the device was no worse than wearing a hat.

Please see the attached documentation, which provides technical specs on this instrumentation, and a detailed assessment of all foreseeable risks (heat injury, electrical injury, mechanical injury, infection transmission, etc) and why we anticipate zero risk from these foreseeable risks.

An accompanying set of non-invasive physiological and environmental measurements will be gathered during the course of the experiment. The measurements, which will include patient acceleration, room temperature, peripheral skin temperature, sensor height, and the pressure applied by the PPG sensor band will be made using standard, commercially available non-invasive and unobtrusive sensors. For example, acceleration measurements will be made utilizing low power MEMS-type accelerometer units developed by companies such as MEMS-IC.

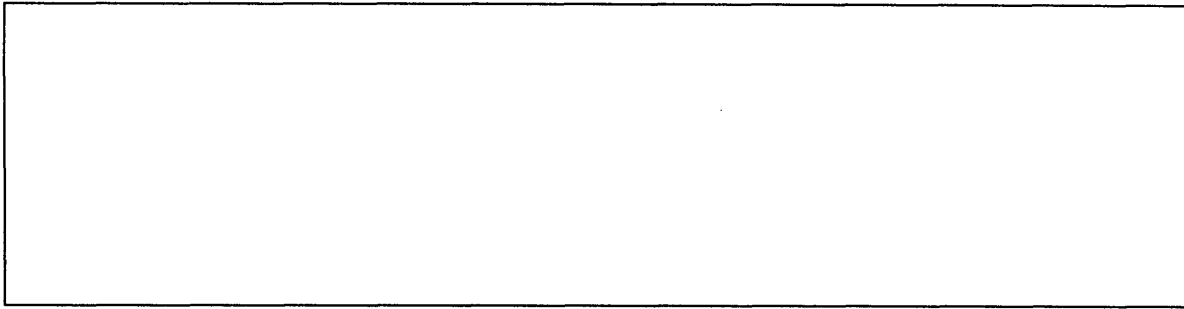
As stated in the previously approved protocol, ALL equipment will be kept clean using hospital-grade cleansers. The equipment will be visually inspected before each experiment and perceptible damage or degradation of the equipment due to repeated use will lead to rescheduling of that experiment and replacement of the equipment.

The experimental protocol consists of a series of measurements using the CO and ABP gold-standards, with simultaneous PPG and EBI measurements. Baseline measurements will be made while the subject is sitting or lying still. After these "at-rest" measurements have been acquired the subject will next be asked to perform a

mild to moderate level exercise task (the equivalent of riding a stationary bicycle). Before beginning the exercise task each subject will be instructed to indicate to the researchers if any discomfort occurs during the task. Additionally, the subject will be asked about their condition periodically throughout the experiment. Any discomfort, although not expected to occur, will result in the immediate conclusion of the experiment.

A second component of the experimental protocol involves a brief period of localized ambient heating and cooling. Each subject will be asked to rest his/her hand inside of a climate-controlled insulated box. Ambient temperatures (continuously monitored using a standard temperature probe) within the box will not exceed 105 F and will not fall below 40 F. The heating elements used for the experiment are purely resistive (no ultraviolet radiation exposure) and the cooling elements consist of a battery powered computer fan and reusable cooler ice packs, all of which will be inaccessible to the subject. The expected duration of each thermal experiment is expected to be no more than 20 minutes. Additionally, as with the exercise protocol, each subject will be reminded of their right to end the experiment at any time prior to the beginning of the experiment. Any patient discomfort will result in the immediate conclusion of the experiment.

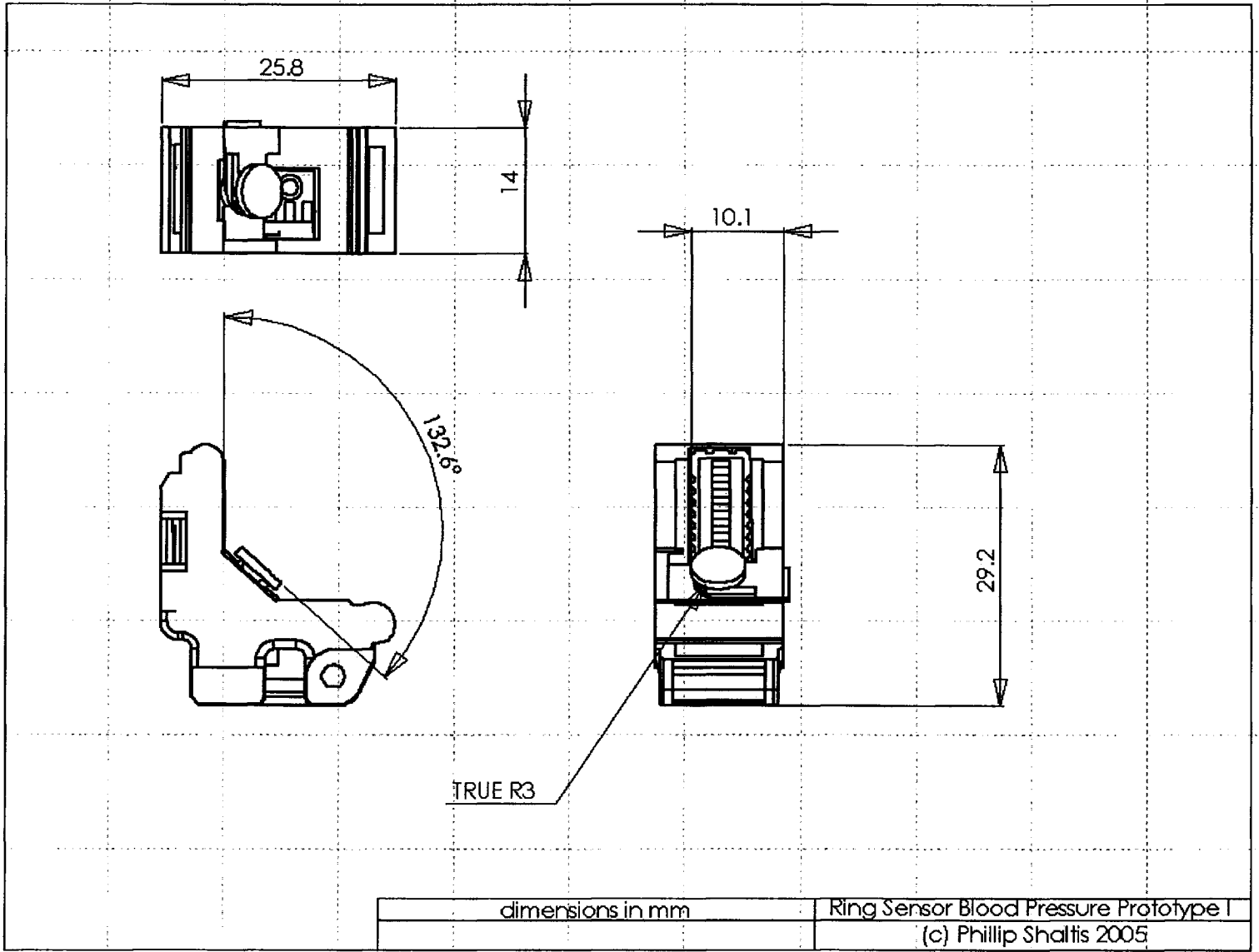
We might repeat the measurements with the PPG and EBI measurements made at different anatomic locations of the extremities and trunk. No locations that are sensitive (i.e. breasts, groin) will be selected. Subjects will be informed of the location of the sensors in advance, and informed that, if they are not 100% comfortable with the location, they should not participate for their own protection. Therefore, no subject will suffer embarrassment when electrodes are placed on their abdomen for the cardiac output measurement.

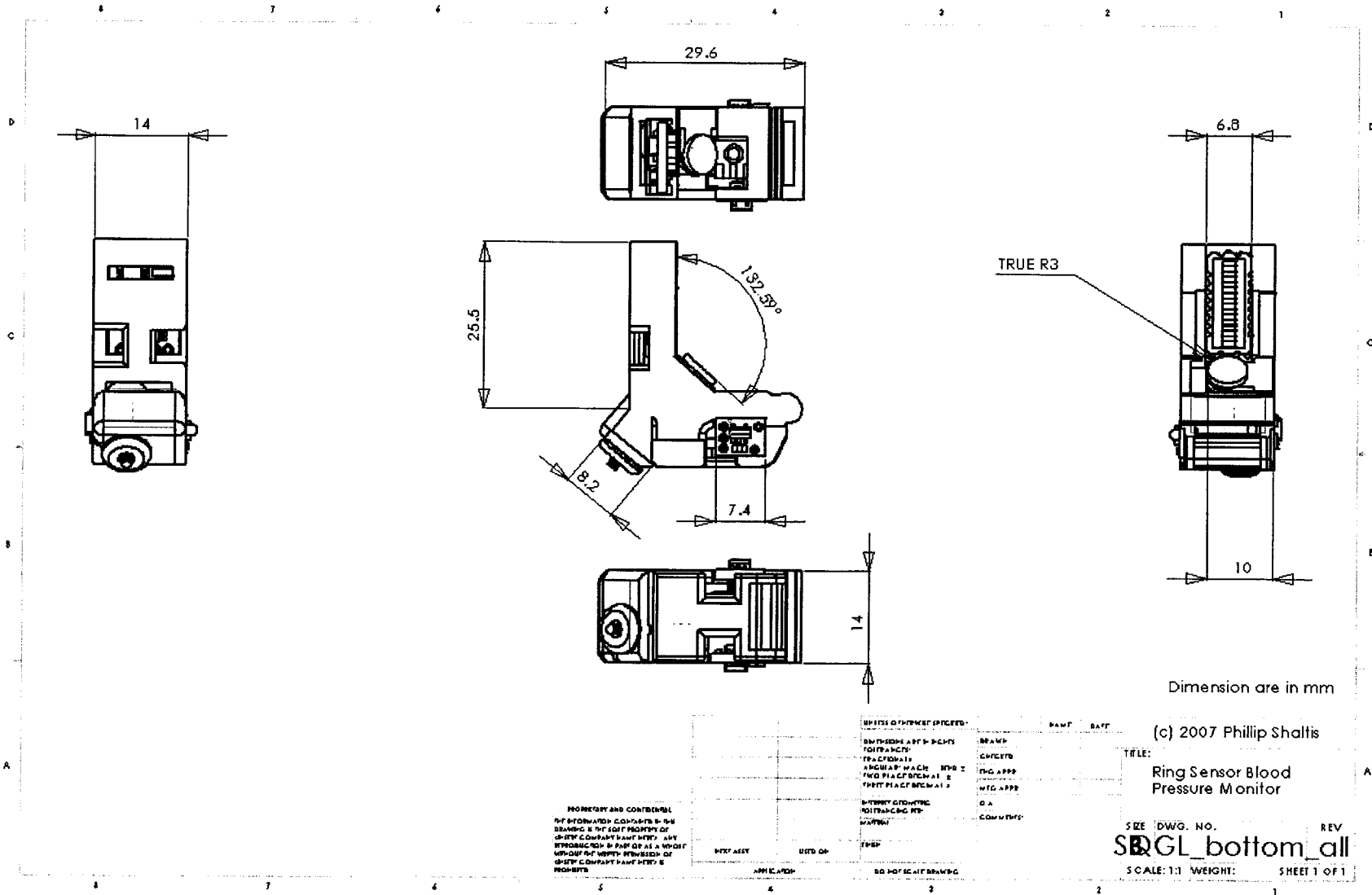


Please return a signed hard copy of this application to the COUHES office at E25-143b

Please also return additional copies, either by email or regular mail, in accord with the instructions on the COUHES web-site.

Appendix B. Ring Sensor Drawings





<p>PROPRIETARY AND CONFIDENTIAL</p> <p>THIS INFORMATION CONTAINS TRADE SECRETS AND IS THE SOLE PROPERTY OF QIWI COMPANY. ANY REPRODUCTION OR DISSEMINATION OF THIS INFORMATION WITHOUT THE WRITTEN PERMISSION OF QIWI COMPANY IS STRICTLY PROHIBITED.</p>	<p>DATE ASST</p> <p>DATE DR</p> <p>APP. LOCATION</p>	<p>DATE</p> <p>NO. OF SCALE DRAWING</p>	<p>REVISED OR CHANGED (SPECIES)</p> <p>DESIGNED BY: PCHM</p> <p>DATE: 05/05/07</p> <p>APPROVED BY: MWS</p> <p>DATE: 05/05/07</p> <p>DESIGNED BY: MWS</p> <p>DATE: 05/05/07</p> <p>DESIGNED BY: MWS</p> <p>DATE: 05/05/07</p>	<p>DRAWN</p> <p>CHECKED</p> <p>ENG APPR</p> <p>MFG APPR</p> <p>QA</p> <p>COMPLETED</p>	<p>PAW</p> <p>BAIT</p>
---	--	---	--	--	------------------------

References

- [1] Pickering TG, Shimbo D, Haas D. Ambulatory blood-pressure monitoring. *N Engl J Med.*, vol. 354(22), pp. 2368-2374, Jun 1 2006.
- [2] Bhatt DL, Steg PG, Ohman EM, et. al.; REACH Registry Investigators. International prevalence, recognition, and treatment of cardiovascular risk factors in outpatients with atherothrombosis. *JAMA.*, vol. 295(2), pp. 180-189, Jan 11 2006.
- [3] McGrath, B.P., Ambulatory blood pressure monitoring. *Med J Aust*, vol. 176(12), pp. 588-592, 2002.
- [4] Payne RA, Symeonides CN, Webb DJ, Maxwell SR. Pulse transit time measured from the ECG: an unreliable marker of beat-to-beat blood pressure. *J Appl Physiol.* , vol. 100(1), pp. 136-141, 2006.
- [5] Lu, W., et al., Research on the main elements influencing blood pressure measurement by pulse wave velocity. *Front Med Biol Eng*, vol. 4(3), pp. 189-199, 1992.
- [6] Davies, J.I. and A.D. Struthers, Pulse wave analysis and pulse wave velocity: a critical review of their strengths and weaknesses. *J Hypertens*, vol. 21(3), pp. 463-472, 2003.
- [7] Asada. H., Shaltis, P., Reisner, A., Rhee, S., and Hutchinson, R., "Mobile monitoring with wearable photoplethysmographic biosensors," *IEEE Engineering in Medicine and Biology Magazine*, vol. 22(3), pp 28-40, 2003.
- [8] Awad AA, et al. How does the plethysmogram derived from the pulse oximeter relate to arterial blood pressure in coronary artery bypass graft patients? *Anesth Analg*, vol. 93(6), pp. 1466-1471, 2001.
- [9] Challoner AVJ, Photoelectric plethysmograph. In: *Non-Invasive Physiological Measurements*, P. Rolfe, Ed. Academic Press: London, 1979, pp. 125-151.
- [10] Whitney, R.J., The measurement of volume changes in human limbs. *J Physiol*, 1953. 121(1): pp. 1-27.
- [11] Fitchett, D.H., Forearm arterial compliance: a new measure of arterial compliance? *Cardiovasc Res*, 1984. 18(11): pp. 651-6.
- [12] Fung, Y.C., B.W. Zweifach, and M. Intaglietta, Elastic environment of the capillary bed. *Circ Res*, 1966. 19(2): p. 441-61.

-
- [13] Meyer, J.U., et al., Vasomotion patterns in skeletal muscle arterioles during changes in arterial pressure. *Microvasc Res*, 1988. 35(2): p. 193-203.
- [14] Challoner, A.V.J., Photoelectric plethysmograph, in *Non-Invasive Physiological Measurements*, P. Rolfe, Editor. 1979, Academic Press: London. p. 125-151.
- [15] Nijboer, J.A., J.C. Dorlas, and H.F. Mahieu, Photoelectric plethysmography--some fundamental aspects of the reflection and transmission method. *Clin Phys Physiol Meas*, 1981. 2(3): p. 205-15.
- [16] Weinman, J., A. Hayat, and G. Raviv, Reflection photoplethysmography of arterial-blood volume pulses. *Med Biol Eng Comput*, 1977. 15: p. 22-31.
- [17] Sara, C.A. and C.A. Shanks, The peripheral pulse monitor--a review of electrical plethysmography. *Anaesth Intensive Care*, 1978. 6(3): p. 226-33.
- [18] Greenwald, S.E., H.T. Denyer, and M.S. Sobeh. Non invasive measurement of vascular compliance by a photoplethysmographic technique. in *SPIE*. 1997.
- [19] Wilson, B.C. and G. Adam, A Monte Carlo model for the absorption and flux distributions of light in tissue. *Med Phys*, 1983. 10(6): p. 824-30.
- [20] Keijzer, M., W.M. Star, and P.R.M. Storchi, Optical diffusion in layered media. *Appl Optics*, 1988. 27: p. 1820-1824.
- [21] Nilsson, L., A. Johansson, and S. Kalman, Macrocirculation is not the sole determinant of respiratory induced variations in the reflection mode photoplethysmographic signal. *Physiol Meas*, 2003. 24(4): p. 925-37.
- [22] Visser, K.R., et al., Observations on blood flow related electrical impedance changes in rigid tubes. *Pflugers Arch*, 1976. 366(2-3): p. 289-91.
- [23] D'Agrosa, L.S. and A.B. Hertzman, Opacity pulse of individual minute arteries. *J Appl Physiol*, 1967. 23(5): p. 613-20.
- [24] Almond, N.E., D.P. Jones, and E.D. Cooke, Noninvasive measurement of the human peripheral circulation: relationship between laser Doppler flowmeter and photoplethysmograph signals from the finger. *Angiology*, 1988. 39(9): p. 819-29.
- [25] Loukogeorgakis, S., et al., Validation of a device to measure arterial pulse wave velocity by a photoplethysmographic method. *Physiol Meas*, 2002. 23(3): p. 581-96.
- [26] Ugnell, H. and P.A. Öberg, The time-variable photoplethysmographic signal; dependence of the heart synchronous signal on wavelength and sample volume. *Med Eng Phys*, 1995. 17(8): p. 571-8.

-
- [27] Kamal, A.A., et al., Skin photoplethysmography--a review. *Comput Methods Programs Biomed*, 1989. 28(4): p. 257-69.
- [28] Zweifler, A.J., G. Cushing, and J. Conway, The relationship between pulse volume and blood flow in the finger. *Angiology*, 1967. 18(10): p. 591-8.
- [29] Kumar, G. and J.M. Schmitt, Optimal probe geometry for near-infrared spectroscopy of biological tissue. *Applied Optics*, 1997. 36(10): p. 2286-93.
- [30] Feng, S., F. Zeng, and B. Chance, Photon migration in the presence of a single defect: a perturbation analysis. *Applied Optics*, 1995. 34(19): p. 3826-37.
- [31] Shelley, K.H., W.B. Murray, and D. Chang, Arterial-pulse oximetry loops: a new method of monitoring vascular tone. *J Clin Monit*, 1997. 13(4): p. 223-8.
- [32] Avolio, A., The finger volume pulse and assessment of arterial properties. *J Hypertens*, 2002. 20(12): p. 2341-3.
- [33] Ando, J., et al., Pressure-volume relationships of finger arteries in healthy subjects and patients with coronary atherosclerosis measured non-invasively by photoelectric plethysmography. *Jpn Circ J*, 1991. 55(6): p. 567-75.
- [34] Yamakoshi, K., Non-invasive and simultaneous cardiovascular measurements using plethysmography techniques. *Front Med Biol Eng*, 1990. 2(4): p. 249-76.
- [35] Chirife, R., V.M. Pigott, and D.H. Spodick, Measurement of the left ventricular ejection time by digital plethysmography. *Am Heart J*, 1971. 82(2): p. 222-7.
- [36] Haffty, B.G., et al., Noninvasive tracking of peripheral resistance by ear densitography. *Chest*, 1983. 83(5): p. 771-5.
- [37] Xu, H., et al., Prediction of pulmonary arterial wedge pressure from arterial pressure or pulse oximetry plethysmographic waveform. *Chin Med J (Engl)*, 2002. 115(9): p. 1372-5.
- [38] Shamir, M. and C. Weissman, Plethysmographic waveform variation as an indicator to hypovolemia. *Anesth Analg*, 2003. 97(2): p. 602; author reply 602-3.
- [39] Shamir, M., et al., Pulse oximetry plethysmographic waveform during changes in blood volume. *Br J Anaesth*, 1999. 82(2): p. 178-81.
- [40] Golparvar, M., H. Naddafnia, and M. Saghaei, Evaluating the relationship between arterial blood pressure changes and indices of pulse oximetric plethysmography. *Anesth Analg*, 2002. 95(6): p. 1686-90, table of contents.

-
- [41] Johansson, A. and P.A. Oberg, Estimation of respiratory volumes from the photoplethysmographic signal. Part 2: A model study. *Med Biol Eng Comput*, 1999. 37(1): p. 48-53.
- [42] Ezri, T., et al., Skin vasomotor reflex as a measure of depth of anesthesia. *Anesthesiology*, 1998. 89(5): p. 1281-2.
- [43] Lu, W., et al., Research on the main elements influencing blood pressure measurement by pulse wave velocity. *Front Med Biol Eng*, 1992. 4(3): p. 189-99.
- [44] Davies, J.I. and A.D. Struthers, Pulse wave analysis and pulse wave velocity: a critical review of their strengths and weaknesses. *J Hypertens*, 2003. 21(3): p. 463-72.
- [45] Rhee, S. Yang B-H and Asada, H., "Modeling of finger plethysmography for wearable sensors," in *Proc. of 21st Annual International Conference of the IEEE Engineering in Medicine and Biology Society*, 1999, vol. 2, pp. 816.
- [46] Rhee, S., "Design and analysis of artifact-resistive finger photoplethysmographic sensors for vital sign monitoring," Ph.D. Thesis, MIT, 2000.
- [47] Srinivasan, M.A. and Dandekar, K., "An Investigation of the Mechanics of Tactile Sense Using Two-Dimensional Models of the Primate Fingertip," *J. of Biomechanical Engineering*, vol. 118, pp. 48-55, 1996.
- [48] Martini, F., Fundamentals of Anatomy and Physiology. 3rd ed., pp. 150, 1995.
- [49] Song, HK., Wehrli, FW., And Ma, J., "In Vivo MR Microscopy of the Human Skin," *MRM*, vol. 37, pp. 185-191, 1997.
- [50] Sandzen, S., Atlas of Acute Hand Injuries. pp. 24, 1980.
- [51] <http://www.anatomyatlases.org/HumanAnatomy/4Section/40.shtml>
- [52] Fung, YC., Biomechanics: Circulation. 2nd ed., pp. 111, 1997.
- [53] <http://www.handuniversity.com/>, 2007
- [54] Cysyk, J. and Srinivasan, M.A., "Skin Dynamics in the Tactile Sensing of Shape," *Touch Lab Report*, RLE Technical Report – 638, MIT, 1999.
- [55] Lockhart, R. D., Hamilton, G. F., and Fyfe, F. W., Anatomy of the Human Body, JP Lippincott Co., Philadelphia, 1965.
- [56] Lanir, Y., Dikstein, S., Hartzshtark, A., and Manny, V., "In Vivo Indentation of Human Skin," *J. of Biomechanics*, vol. 112, pp.63-69, 1990.

-
- [57] Dai, G., Gertler, J. P. and Kamm, R. D., "The Effect of External Compression on Venous Blood Flow and Tissue Deformation in the Lower Leg," *Journal of Biomedical Engineering*, vol. 121, 557-564, 1999.
- [58] Sato, M., Hayashi, K., et. al., "Axial Mechanical Properties of Arterial Walls and their Anisotropy," *Med. Biol. Eng. Comp.*, vol. 17, pp. 170-176, 1979.
- [59] Bathe, M., "A Fluid-Structure Interaction Finite Element Analysis of Pulsatile Blood Flow through a Compliant Stenotic Artery," B.S. Thesis, MIT, 1998.
- [60] Tang, D., Yang, J., et. al., "A Nonlinear Axisymmetric Model with Fluid-Wall Interactions for Steady Viscous Flow in Stenotic Elastic Tubes," *J. of Biomechanical Engineering*, vol. 121, pp. 494-501, 1999.
- [61] Dandekar, K. and Srinivasan, M. A., "Role of Mechanics in Tactile Sensing of Shape," Touch Lab Report 2, RLE Technical Report - 604, MIT, 1996.
- [62] Dandekar, K., B.I. Raju and M.A. Srinivasan., "3-D Finite-Element Models of Human and Monkey Fingertips to Investigate the Mechanics of Tactile Sense." *J. of Biomechanical Engineering*, vol. 125, pp. 682-691, 2003.
- [63] Maeno, T., Kawai, T. and Kobayashi, K., "Analysis and Design of a Tactile Sensor Detecting Strain Distribution Inside an Elastic Finger," *Proceedings of the 1998 International Conference on Intelligent Robotics and Systems, Victoria, B.C., Canada*, pp.1658-1663, 1998.
- [64] Shimazu, H., Kawarada, A., Ito, H. and Yamakoshi, K., "Electric Impedance cuff for the indirect measurement of blood pressure and volume elastic modulus in human limb and finger arteries," *Medical & Biological Engineering & Computing*, vol. 27, pp. 477-483, 1989.
- [65] Keller, TS., "Predicting the Compressive Mechanical Behavior of Bone," *J. of Biomechanics*, vol. 27(9), pp. 1159-1168, 1994.
- [66] Hoffmeister, BK., Handley, SM., et. al., "Estimation of the Elastic Stiffness Coefficient c_{13} of Fixed Tendon and Fixed Myocardium," *J. of the Acoustic Society of America*, vol. 97 (5 Pt 1), pp. 3171-3176, 1995.
- [67] Voss., K. J. and Srinivasan, M. A., "Investigation of the Internal Geometry and Mechanics of the Human Fingertip, in vivo, using Magnetic Resonance Imaging," Touch Lab Report 10, RLE Technical Report - 622, MIT, January, 1998.
- [68] Musculoskeletal MRI, Phoebe Kaplan, et al., 1st ed., W.B. Saunders Company: Philadelphia, PA, p. 261, 2001.

-
- [69] Rhee, S., Yang, B-H and Asada, H., "Artifact-resistant, power-efficient design of finger-ring plethysmographic sensors," IEEE Transactions on Biomedical Engineering, vol. 48(7), pp. 795-805, 2001.
- [70] http://www.robotmaker.co.uk/Parts/Motors/Nano_motors/motors_nano_rmn1.htm , 2006.
- [71] <http://www.didel.com/slow/pricelist/images/10R4.jpg> , 2006.
- [72] <http://www.newscaletechnologies.com/>, 2007.
- [73] Parati, G., Ongaro, G., Bil, G., et. al. "Non-invasive beat-to-beat blood pressure monitoring: new developments," Blood Pressure Monitoring, vol. 8, pp. 31-36, 2003.
- [74] Levenberg, K., "A method for the solution of certain non-linear problems in least squares." Quarterly of Applied Mathematics, vol. 2(2), pp. 164-168, July 1944.
- [75] Marquardt, D.W., "An algorithm for the least-squares estimation of nonlinear parameters." SIAM Journal of Applied Mathematics, vol. 11(2), pp. 431-441, June 1963.
- [76] Wang, J.J., Lin, C.T., Liu, S.H., Wen, Z.C., "Model-based synthetic fuzzy logic controller for indirect blood pressure measurement., IEEE Transactions on Systems, Man, and Cybernetics, Part B: Cybernetics, vol. 32(3), pp. 306-15, June 2002.
- [77] Shaltis, P., Reisner, A., Asada, H., "Calibration of the photoplethysmogram to arterial blood pressure: capabilities and limitations for continuous pressure monitoring," Proc. of the 27th Annual International Conference of the IEEE/EMBS, 2005, pp. 3970-3973.
- [78] Geddes, L. and Roeder, R., "Oscillometric noninvasive blood pressure monitor," U.S. Patent 7014611, Mar. 21, 2006.